PEOPLE'S DEMOCRATIC REPUBLIC OF ALGERIA

MINISTRY OF HIGHER EDUCATION

AND SCIENTIFIC RESEARCH

University of Echahid Hamma Lakhdar - El Oued

FACULITY OF TECHNOLOGY

DEPARTMENT OF PROCESS ENGINEERING AND PETROCHEMICALS

Thesis Submitted in Partial Fulfilment of the Requirement for the Degree of

LMD Doctorate

in Process Engineering

Specialty: Process Engineering

Optimizing the Biosynthesis Temperature of Iron Oxide Nanoparticles Using Moringa Oleifera Extract and Study of their Biological Activities

Presented by

TEDJANI Mohammed Laid

Before the jury composed of

FERHAT Mohammed Fouad	MCA	University of El-Oued	President
KHELEF Abdelhamid	Professor	University of El-Oued	Supervisor
ZIDANE Mohamed	MCA	University of El-Oued	Examiner
SEKIRIFA Mohamed Lamine	Professor	University of Ouargla	Examiner
SELLAMI Mohamed Hassen	Professor	University of Ouargla	Examiner
LAOUINI Salah Eddine	Professor	University of El-Oued	Invited

2021-2022

Dedication

To my beloved parents,

To my dear fiancée

To my sister and my brothers,

To all the members of my big family,

To the memory of all my grandparents,

To all my teachers and instructors,

To all my friends and classmates,

To the pursuit of knowledge, the thrill of discovery and the hope of their use for the betterment of humankind.

Acknowledgments

First and foremost, I have to thank greatly God for giving me the power to complete this work.

I have a deep sense of gratitude to my supervisor Prof. ***KHELEF Abdelhamid*** *for all of his constant support, motivation and friendship throughout the completion of this thesis. His wide knowledge, logical thinking, continuous encouragement and wise guidance made it an absolute privilege to work under his supervision.*

I am sincerely grateful to the jury members ***Dr. FERHAT Mohammed Fouad, Dr. ZIDANE Mohamed, Pr. SEKIRIFA Mohamed Lamine, Pr. SELLAMI Mohamed Hassen, and Pr. LAOUINI Salah Eddine****, who honored me by accepting to be members in this jury and for devoting their time and efforts in reading and evaluating this thesis.*

I am very thankful to all my teachers in the process engineering and petrochemicals department of Echahid Hamma Lakhdar University for their valuable edification.

I wish to extend my special thanks to Mr. ***Ali TLIBA, and Mrs. LAOUINI*** *for their help and assistance in laboratory.*

I am extremely thankful to all my beloved teachers especially, ***Mr. HAMDAOUI Boudjemaa and Mr. CHERFI Mohamed Nabil****, who believed in me and taught me the most important lessons of my life "****THANK YOU VERY MUCH!****".*

Finally, I would like to express my highest respect and gratitude to my parents for their unconditional love and support which promoted the essence of my life and made my successes possible.

Abstract

ملخص

Résumé

Abstract

The past two decades have seen a growing interest in optimizing the synthesis of metal oxide nanoparticles due to their unique properties that have made revolutionary improvements in many fields. This work aims to optimize the biosynthesis temperature of iron oxide nanoparticles and to study their biological activity. *Moringa Oleifera* leaves extract was used as a bio-reducing and stabilization agent for the biosynthesis process, and the optimization was performed using response surface methodology (RSM) based on central composite design (CCD). The biosynthesis temperatures (reaction and annealing temperatures) besides precursor concentration were set as independent variables, and the crystallite size was set as a response to obtain the optimal conditions that minimize IONPs crystallite size. Different characterization techniques such as UV-Vis, FTIR, XRD, SEM, and EDX were employed to study the nanoparticles properties. The characterizations results have confirmed the biosynthesis of Hematite (α-Fe_2O_3) nanoparticles of rhombohedral structure. The generated model has exhibited predicted values very close to the actual proving its validity to analyze and optimize this study. The model indicated that all the investigated parameters and their interactions significantly affected the crystallite size. Within the studied range, an optimal crystallite size of 29.35 nm was achieved when biosynthesis temperatures i.e., reaction and annealing temperatures are 55 and 500 °C respectively, and precursor concentration of 0.03 M. Furthermore, the antibacterial activity of IONPs was tested using the disk diffusion method, which has shown significant antibacterial activity against both Gram-positive and Gram-negative bacteria.

Keywords:

Nanoparticles; Iron oxide; Optimization; Biosynthesis temperature; *Moringa Oleifera*; Crystallite size; RSM; Antibacterial activity.

ملخص

شهد العقدان الماضيان إهتمامًا متزايدًا بتحسين صناعة جزيئات أكسيد المعادن النّانويّة نظرًا لخصائصها الفريدة اللتي أدت تحسينات جوهرية في العديد من المجالات. يهدف هذا العمل إلى تحسين درجة حرارة التصنيع الحيوي لجسيمات أكسيد الحديد النّانويّة ودراسة نشاطها البيولوجي. تم إستخدام مستخلص أوراق *موريـنجا أوليفيرا* كعامل إرجاع حيوي لعملية التصنيع الحيوي، وتم إجراء عملية التحسين بإستخدام منهجية سطح الإستجابة (RSM) بناءً على التصميم المركب المركزي (CCD). تم إختيار درجات حرارة التصنيع الحيوي (درجات حرارة التفاعل والتكلس) إلى جانب تركيز الملح المعدني كمتغيرات مستقلة ، و أُختير الحجم البلوري كمتغير تابع (إستجابة) من أجل الحصول على الظروف المثلى التّي تقلّل من حجم البلورات النّانوية لأكسيد الحديد. تم إستخدام تقنيات توصيف مختلفة مثل الأشعَّة فوق البنفسجية UV-Vis، الأشعَّة تحت الحمراء FTIR، إنعراج الأشعَّة إكس XRD، مسح المجهر الإلكتروني SEM و الأشعَّة السِّينية المُشَتَّتَةِ للطاقة EDX لدراسة خصائص الجسيمات النّانويّة. نتائج التوصيفات أكدت نجاح صناعة الجسيمات النّانويّة لأكسيد الحديد من نوع الهيماتيت (α-Fe_2O_3) ذو هيكل كريستالي مُعَيَّنِيُّ السُّطوح. أظهر النموذج الرّياضي الذي تم إنشاؤه قِيَمًا توقعيَّة قريبة جدًا من القيم التَّجريبيَّة مما يثبت قدرة هذا النَّموذج على التنبُّؤِ الصَّحيح بنتائج هذه الدراسة وتحسينها. أشار النموذج إلى أن جميع المتغيرات التي تم فحصها وتداخلاتها أثرت بشكل كبير على حجم البلورات. ضمن النطاق المدروس ، تم التحصل على حجم بلوري مثالي قدره 29.35 نانومتر عندما تكون درجات حرارة التفاعل والتكلس 55 و 500 درجة مئوية على التوالي ، والتركيز المولاري للملح المعدني 0.03 مولاري. علاوة على ذلك ، تم إختبار النشاط المضاد للبكتيريا لجزيئات أكسيد الحديد النّانويّة بإستخدام طريقة القرص المنتشر، وأظهر فعالية معتبرة ضد كل من البكتيريا مُوجَبَةُ و سَالِبَةُ الجرام.

الكلمات المفتاحية:

الجسيمات النانوية؛ أكسيد الحديد؛ التحسين؛ درجة حرارة التصنيع الحيوي؛ *موريـنجا أوليفيرا* ؛ حجم بلوري؛ RSM؛ الفعالية المضادة للبكتيريا.

Résumé

Au cours des deux dernières décennies, un intérêt croissant pour l'optimisation de la synthèse des nanoparticules d'oxyde métallique en raison de leurs propriétés uniques a permis des développements révolutionnaires dans de nombreux domaines. Ce travail vise à optimiser la température de biosynthèse des nanoparticules d'oxyde de fer et à étudier leur activité biologique. L'extrait de feuilles de *Moringa Oleifera* a été utilisé comme agent de bio-réduction et stabilisation pour le processus de biosynthèse et l'optimisation a été réalisée à l'aide de la méthodologie de surface de réponse (RSM) basée sur la conception composite centrale (CCD). Les températures de biosynthèse (températures de réaction et de recuit) en plus de la concentration de précurseur ont été choisies comme variables indépendantes et la taille des cristallites a été définie comme une réponse pour obtenir les conditions optimales qui minimisent la taille des cristallites des IONP. Différentes techniques de caractérisation telles qu'UV-Vis, FTIR, XRD, SEM et EDX ont été utilisées pour étudier les propriétés des nanoparticules. Les résultats des caractérisations ont confirmé la biosynthèse de nanoparticules d'Hématite (α-Fe_2O_3) de structure rhomboédrique. Le modèle mathématique généré a présenté des valeurs prédites très proches de l'expérimental ce qui prouve sa validité pour analyser et optimiser cette étude. Le modèle a indiqué que tous les paramètres étudiés et leurs interactions ont significativement affecté la taille des cristallites. Dans l'échelle étudiée, une taille de cristallite optimale de 29,35 nm a été atteinte lorsque les températures de (les températures de réaction et de recuit) sont respectivement de 55 et 500 °C et la concentration en précurseur de 0,03 M. De plus, l'activité antibactérienne des nanoparticules d'oxyde de fer a été testée à l'aide de la méthode de diffusion sur disque, et les nanoparticules ont montré une activité antibactérienne significative contre les bactéries Gram-positifs et les Gram-négatives.

Mots clés :

Nanoparticules; Oxyde de fer; Optimisation ; Température de biosynthèse; *Moringa oleifera*; Taille des cristallites; RSM; Activité antibactérienne.

List of abbreviations

IONPs	Iron Oxide Nanoparticles
NPs	Nanoparticles
CCD	Central Composite Design
RSM	Response Surface Methodology
DOE	Design Of Experiments
ANOVA	Analysis of Variance
UV-Vis	Ultraviolet–visible spectroscopy
FTIR	Transform Infrared spectroscopy
XRD	X-Ray Diffraction
SEM	Scanning Electron Microscopy
EDX	Energy Dispersive X-ray analysis
R^2	Coefficient of determination
P-value	Probability value
F-value	Fisher test value
DF	Degree of Freedom
MHA	Mueller-Hinton agar
NA	Nutrient Agar
pH	potential of Hydrogen
M	Molar
kDa	kiloDalton
DM	Dry Matter

List of figures

Chapter I

CHAPTER II

CHAPTER III

CHAPTER IV

APPENDIXES

List of tables

CHAPTER I

CHAPTER II

Chapter III

Chapter IV

Table of contents

CHAPTER II

CHAPTER III

CHAPTER IV

GENERAL INTRODUCTION

General introduction

In the past two decades, nanoscale materials of single or multidimensions and a size below 100 nm have attracted increasing interest due to their new and unique features over their bulk counterparts [1]. The new features of these materials have made revolutionary improvements in many fields, making nanoscience one of the most promising and innovative fields of research in materials sciences.

Various inorganic materials have been modified, and their size was reduced to nanoscale as nanoparticles in order to achieve superior properties with greater functional versatility. Among the inorganic nanoparticles, Iron oxide nanoparticles (IONPs) in particular magnetite (Fe_3O_4), maghemite (γ-Fe_2O_3), and hematite (α-Fe_2O_3) are of great technological and industrial interest due to their unique properties appropriate for many fields, including the electronics industry for the fabrications of the new generation technological devices [2], medicine field especially for diagnostics; drug delivery and antimicrobial agents [3,4], the agriculture sector as a fertilizers [5], and environmental remediation removal of pollution or contaminants from water [6].

Diverse chemical and physical processes have been extensively employed for the fabrication of metal nanoparticles. However, these production methods are generally costly, toxic, and potentially dangerous to the environment and living organisms. Which have arisen many concerns about the production of nanomaterials; these concerns are faded by implementing a sustainable green biological method in nanomaterials production, which uses biodegradable and biocompatible natural sources such as bacteria fungi, and plant extracts. This synthesis method allowed the production of low-cost, non-toxic, and eco-friendly nanomaterials [7].

The unique features of iron oxide nanoparticles are significantly influenced by their shape and size [2,8–11]. Generally, significant enhancements on nanoparticles properties are reached by reducing their size. Therefore, extensive studies and efforts were made to better understanding the relationship between the size and properties, aiming to reach a size-controlled synthesis of nanoparticles with optimized properties and best performance [12].

Former studies in the literature have found that it is possible to control nanoparticles' size and properties by adjusting the synthesis conditions including reaction temperature, pH,

duration, and reactant concentration that significantly influences the growth of nanoparticles' crystallite size [13–18].

Most of the previous works optimizing the synthesis parameters and studying their effect on nanoparticles size have restricted their investigation to study separate synthesis parameters in what is known with One Factor At Time (OFAT) optimization. This technique is surrounded by many disadvantages, such as not being able to explain the interactive effect of multiple synthesis parameters; also, it requires a considerable number of experiments that could be expensive and a waste of time, resources, and efforts [19].

These disadvantages can be efficiently reduced using multivariate statistical techniques such as Response Surface Methodology (RSM), which is a set of mathematical and statistical techniques based on the adjustment of a polynomial equation to the experimental data that effectively model and study processes by investigating the effect of multiple factors (independent variables) and their combined effect on the response (dependent variables). The most advantageous feature of RSM is its ability to assist determining the optimal conditions for a combination of factors that optimizes the response maintaining a reduced number of experiments, which saves efforts, recourses and time[20].

This work aims to optimize the biosynthesis temperature of IONPs and to study their biological activity. *Moringa Oleifera* leaves extract was used for the biosynthesis process, and the optimization was performed using response surface methodology RSM based on central composite design.

This work consists of four chapters:

- The first chapter represents a botanical study of *Moringa Oleifera* and its phylogenic classification.
- The second chapter is a literature review on nanoparticles, their synthesis, classifications, properties, and applications.
- The third chapter briefly describes the materials, analysis, and optimization methods used for this study.
- The fourth chapter displays the different results of the optimization, characterizations, and antibacterial activity for the performed experiments in tables and graphs, followed by discussions and interpretations.

Finally, a general conclusion summarizes the main results obtained during this thesis and suggestions for further study.

GENERALITIES ON MORINGA OLEIFERA

Chapter I: Moringa Oleifera

There was always a close relationship between human beings and plants. Since the early ages, plants have symbolized life and sustainability for humankind due to their benefits and diverse applications in different fields, such as food, medicine, and construction. Up to this day, plants are being widely used in high-tech sectors and advanced medicine.

I.1 Moringa Oleifera

Moringa Oleifera is considered one of the world's most useful and easily accessible trees. It is widely cultivated because of its capability to quickly grow and resistance to poor soil [1]. Besides using it as food, *Moringa Oleifera* is also famous with its important healing abilities which make it earn the name of "the miracle tree" or "the tree of life"[2].

I.2 Nomenclature

Moringa Oleifera has different names depending on the region[3]:

Table I. 1 Some common names of *Moringa oleifera*

English	Arabic	Hindi	French
Drumstick tree	Ruwag	Horseradish	Ben ailé
Ben oil tree	Shajarat Al Ban	Shajnah	benzolive
Horseradish tree	Habbah Ghaliah	Dumstick	Pois Quénique

I.3 Taxonomic classification:

Moringa is the only genus from the *Moringaceae* family. [4], [5]

Table I. 2 Taxonomy classification of *Moringa Oleifera* [4], [5].

Kingdom	Plantae
Subkingdom	Tracheobionta
Superdivision	Spermatophyta
Division	Magnoliophyta
Class	Eudicots
Subclass	Rosids
Order	Brassicales
Family	Moringaceae
Genus	*Moringa*

I.4 History

Moringa has been used by many societies including Roman, Greek, Egyptian, and Indian for thousands of years with writings dating as far back as 150 AD. The history of Moringa dates back to 150 B.C. Historical proofs reveal that ancient kings and queens used Moringa leaves and fruit in their diet to maintain mental alertness and healthy skin [6].

I.5 Geographical distribution

Moringa Oleifera is a tree native to the Himalayas, India northeast, Bangladesh, Afghanistan, and Pakistan. It has been introduced to all the tropics and subtropics and has become naturalized in many African countries. This tree has an extensive geographic distribution throughout Central and South America, Africa, and South Asia [7].

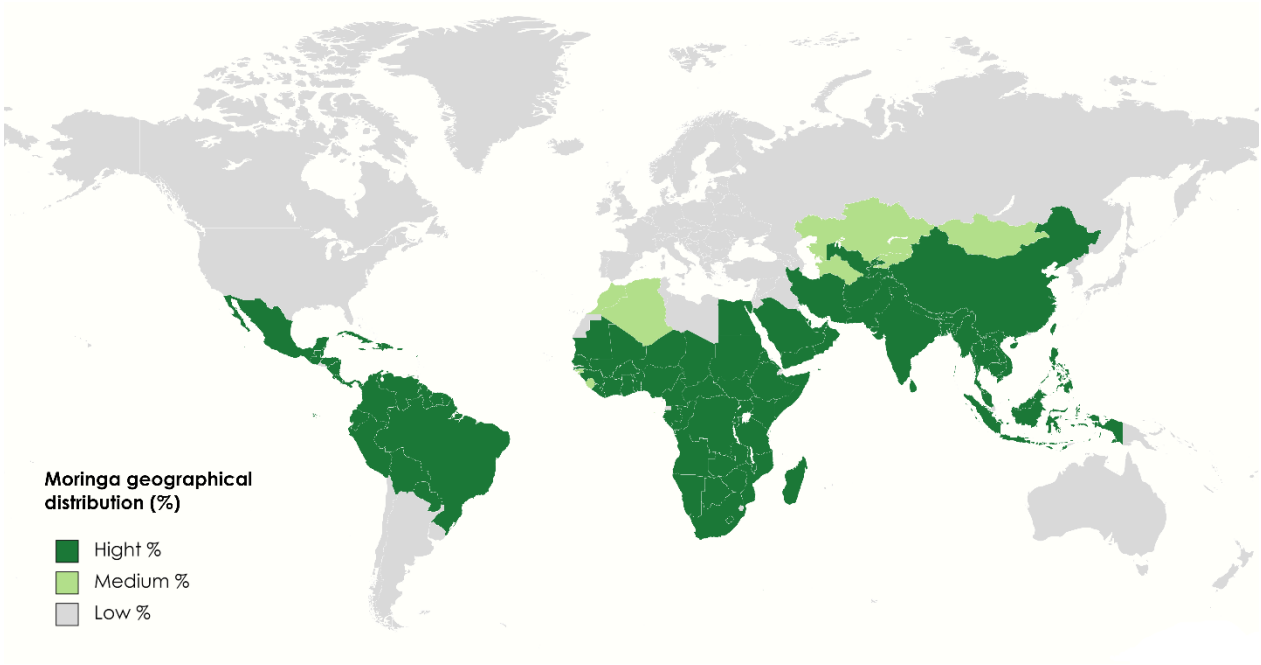

Figure I.1 Geographical distribution of *Moringa Oleifera* in the world [8].

I.6 Botanical description for the different parts of *Moringa Oleifera* plant

Moringa Oleifera tree is a fast-growing plant. It can grow to reach 10 to 15 m in height and up to 3 meters in diameter, with an umbrella-shaped open crown and a straight trunk of 20 to 40 cm in diameter. In general, it reaches 1.5 to 3 meters high before dividing into branches. *Moringa Oleifera* wood is soft, very tender, and often attacked by termites [2], [9].

Figure I. 2 *Moringa Oleifera* tree.

I.6.1 **Seeds**

The seeds are round with a brownish semi-permeable seed hull, with 3 papery wings. Seed hulls are generally brown to black but can be white if kernels are of low viability. Viable seeds germinate within 2 weeks. The hull itself has three white wings that run from top to bottom at 120° intervals. Each tree can produce between 15,000 and 25,000 seeds/year. The average weight per seed is 0.3 g and the kernel to hull ratio is 75:25[10].

Figure I. 3 *Moringa Oleifera* seeds.

I.6.2 **Flowers**

The flowers are 2.5 cm wide and appear as axillary, drooping panicles of 10 to 25 cm. They are generally abundant and with a pleasant odor. Moringa flowers are consist of five creamy-white petals with yellow dots at the base five perfect stamens alternating with five subulate staminodes, and five sepals that are symmetrical and lanceolate [3], [11].

Figure I. 4 *Moringa Oleifera* flowers.

I.6.3 **Fruits**

The fruits are pendulous, linear, three-sided pods with nine longitudinal ridges, usually 20 to 50 cm in length, but infrequently up to 1 m or longer, and 2.0 to 2.5 cm thick. Each pod usually contains up to 26 seeds [12].

Figure I. 5 *Moringa Oleifera* fruits.

I.6.4 **Branches**

Moringa Oleifera branches grow in a disorganized manner, and the canopy takes an umbrella shape [13].

Figure I. 6 *Moringa Oleifera* branches.

I.6.5 **Roots**

Moringa Oleifera seeds develop a white, swollen, tuberous root with a characteristic pungent odor and sparse side roots. Trees grown from seeds develop a deep, stout taproot with a wide-spreading system of thick, tuberous lateral roots [12], [14].

Figure I. 7 *Moringa Oleifera* roots.

I.6.6 Leaves

The leaves are usually bipinnate or tripinnate and can reach up to 45 cm long. They are alternate and spirally arranged on the twigs. Pinna and pinnules are opposite; leaflets are 1.2 to 2 cm long and 0.6 to 1 cm wide, the lateral leaflets elliptic, the terminal ones obovate; petioles of lateral leaflets are 1.5 to 2.5 mm long, those of terminal ones 3 to 6 mm long [15], [16].

Figure I. 8 *Moringa Oleifera* leaves.

I.7 Main ecological requirements of Moringa Oleifera

I.7.1 Altitude

Moringa Oleifera favors an altitude beneath 600 m from sea level. Although, it can grow up to 1200 m in some tropical areas and has also been observed growing at 2000 m [17], [18].

I.7.2 Temperature

Generally, *Moringa Oleifera* grows best under warm, dry conditions in tropical and semi-arid regions. The ideal temperature range for this plant is 25 to 35 ºC, but it can tolerate temperatures up to 48 ºC for short periods [18], [19].

I.7.3 Soil

Moringa tolerates a wide range of soil types. However, it prefers well-drained (light) sandy soils that do not retain water which Helps the root branches cuttings their way directly into the ground. It would also grow well in heavy soils (clay) that doesn't remain waterlogged for prolonged periods [18].

I.7.4 pH

Moringa Oleifera tolerates a wide pH range from 4.5 to 9. This plant can also grow well in an alkaline medium up to a pH of 9 [18].

I.7.5 Wind

Moringa Oleifera can be very susceptible to a windy climate. The strong winds can cause considerable damage to the tree branches and trunk [18].

I.8 Nutritional values of *Moringa Oleifera*

Moringa Oleifera is well-known for its high nutrient value. Previous studies have proven that fresh leaves of this plant contain [20], [21]:

- 4 times more vitamin A than carrots.
- 7 times more vitamin C than oranges.
- 4 times more calcium than milk.
- 3 times more potassium than bananas.
- 5 times the iron contained in spinach.
- 2 times more protein than eggs.
- 8 times more fiber than wheat.
- 30 times more vitamin B2 than almonds.

- Figure I. 9 Vitamin and mineral content of *Moringa Oleifera* leaves[8].

I.9 Chemical compositions

Regarding the beneficial health effects of *Moringa Oleifera*, it is a unique herb owing to its rich nutrients and low antinutrient content. The leaves of *M. oleifera* are the most nutritious part, being a significant source of proteins, minerals, vitamins, and other secondary metabolites. The Table I. 2 and Table I. 3 below shows the chemical and amino acid compositions presented in 100 g of *Moringa Oleifera* fresh leaves, dry leaves and powdered leaves [21], [22].

Table I. 3 Chemical compositions of *Moringa Oleifera* leaves [21], [22].

Nutrient component	Fresh leaves	Dry leaves	Powdered leaves
Calories (cal)	92	329	205
Protein (g)	6.7–17.1	29.4–40.0	25.4–27.1
Fat (g)	1.7–2.11	5.2–6.5	2.3
Carbohydrates (g)	6.3–12.5	38.0–41.2	34.3–38.2
Fiber (g)	0.9–7.09	12.5–21.09	19.2
Vitamin A	0.9–11.05	16.3–18.90	-
Vitamin B1 (mg)	0.06	2.02–2.60	2.64
Vitamin B2 (mg)	0.05	19.82–21.3	20.5
Vitamin B3 (mg)	0.8	7.6–8.3	8.2
Vitamin C (mg)	220	15.8–17.3	17.3
Vitamin E (mg)	448	10.8–77.0	113
Calcium (mg)	440	2185–3050	2003
Magnesium (mg)	42–82	86–448	368
Phosphorus (mg)	30.15–70	204–252	204
Potassium (mg)	259	1236–1384	1324
Copper (mg)	0.07	0.08–0.49	0.57
Iron (mg)	0.85–10.7	25.6–490	28.2
Sulfur (mg)	-	363–630	870
Zinc (mg)	6.7	3.25–13.03	-
Manganese (mg)	81.6	86.8–91.2	-

Table I. 4 Amino Acid Content of *Moringa Oleifera* Leaves. [21], [22].

Amino acid	Fresh leaves (mg / g DM)	Extracted leaves (mg / g DM)
Lysine	13.25–26.77	14.06–18.09
Leucine	20.52–42.89	17.5–21.84
Isoleucine	11.91–22.53	8.08–11.30
Methionine	3.5–8.96	1.13–4.97
Cystine	3.8–5.18	1.0–3.39
Phenylalanine	16.31–27.14	8.9–15.51
Tyrosine	18.88	9.71
Valine	10.62–27.58	7.25–14.26
Histidine	5.17–13.57	7.16–7.50
Threonine	13.5–21.97	7.90–11.70
Serine	10.87–20.79	9.40–10.34
Glutamic acid	28.42–50.85	17.10–25.65
Aspartic acid	20.52–46.11	14.3–22.16
Proline	14.3–25.75	12.41–13.63
Wisteria	15.33–26.62	10.3–13.73
Alanine	28.67–30.33	12.51–18.37
Arginine	18.9–30.28	13.25–15.64
Tryptophan	4.25–9.26	5.27–7.16

I.10 *Moringa Oleifera* applications

Moringa Oleifera leaves are widely distributed all over the world, they have a wide range of applications due to their nutritional and medicinal benefits. Almost every part of this tree has been found to possess many nutrients. Among the different applications of this plant we distinguish:

I.10.1 Human consumption

The leaves, fruits, young stems, roots, and flowers are edible and are eaten all over the world. The leaves can be eaten fresh or powdered and even combined with spices such as chili, they can also be prepared in soup or salad. The young green pods can be eaten boiled like beans.

The dry seeds can be powdered and used to season sauces, and the flowers can also be eaten as raw vegetables (salad). *Moringa Oleifera* oil is used as edible vegetable oil and also as a cooking oil [23], [24].

I.10.2 Animal consumption

Moringa Oleifera is rich in nutrients and bioactive compounds that offer great potential for its use as a livestock feeding resource. The leaves, seeds, and tree bark are easily consumed by farm animals such as cattle, sheep, and goats as ingredients in nutrition [25].

I.10.3 Pharmaceutical

Moringa Oleifera can be used to cure over 300 diseases. It has been used in herbal medicine for a long by Indians and Africans, the presence of phytochemicals makes it an important medicinal agent. The different parts of this tree, including the roots, bark, leaves, flowers, fruits, and seeds have been traditionally used in various therapeutic applications including abdominal tumors, hysteria (psychological disorder), scurvy, bladder palsy, and prostate [26], [27].

Figure I. 10 Pharmaceutical applications of *Moringa Oleifera*

I.10.4 Water treatment

The aqueous seed extract has traditionally been used to purify water in Africa and South Asian countries as a natural coagulant, since it exhibits high levels of active cationic proteins with molecular weights between 6 and 16 kDa and highly alkaline isoelectric points. In addition, it's well-known that the seeds can reduce 99.9% of bacteria suspended in the water after a treatment of 1 to 2 hours [28].

I.10.5 Industrial applications

Due to its properties, *Moringa Oleifera* oil is used as a lubricant in fine machinery, such as watchmaking (for its low tendency to deteriorate and become rancid and sticky). It is also of interest in the cosmetics and perfumes industry. The wood of this tree is "also an excellent pulp [29].

I.10.6 Biodiesel

After extracting high-value nutrients, *Moringa Oleifera* oil can be converted to biodiesel. The most remarkable property of this biodiesel is its high cetane number. The studied physicochemical properties of the biodiesel in *Moringa Oleifera* oil suggest that it can be used as a fuel in engines [30], [31].

I.10.7 Other applications

Moringa Oleifera has other abilities; its seeds are used to purify milk and honey. Due to its content of phytohormone compounds such as Cytokinins. This plant can be used as a fertilizer to boost tree growth and plant yields. *Moringa Oleifera* was also used as a phase barrier and windbreak [32].

I.11 Agroecological importance

Moringa Oleifera is one of the most useful tropical trees. It spreads relatively easily both vegetatively and sexually, and it does not require much water and minerals. Thus, its production and maintenance are easy. Introducing this plant to a farm in an environment rich in biodiversity can benefit both the farmer and the surrounding ecosystem. Almost all parts of the plant have nutritional interests, which highlight the plant socioeconomic importance in the agroecological region [33].

References

[1] A. A. Mariod, M. E. Saeed Mirghani, and I. Hussein, "Chapter 35 - Moringa oleifera Seed Oil," A. A. Mariod, M. E. Saeed Mirghani, and I. B. T.-U. O. and O. S. Hussein, Eds. Academic Press, 2017, pp. 233–241.

[2] H. S. U. Rebecca, M. Sharon, A. Arbainsyah, and D. Lucienne, "Moringa oleifera: medicinal and socio-economic uses," *Int. Course Econ. Bot. Natl. Herb. Leiden, Netherlands*, vol. Miracle, pp. 2–6, 2006.

[3] T. K. Lim, "Moringa oleifera," in *Edible Medicinal And Non Medicinal Plants*, Springer, 2012, pp. 453–485.

[4] M. Korsor, C. Ntahonshikira, H. M. Bello, and H. M. Kwaambwa, "Com-parative Study of M. oleifera and M. ovalifolia Survival Rates in Central Namib-ia," *J Plant Sci Curr Res*, vol. 1, no. 001, 2017.

[5] D. S. Arora, J. G. Onsare, and H. Kaur, "Bioprospecting of Moringa (Moringaceae): microbiological perspective," *J. Pharmacogn. Phytochem.*, vol. 1, no. 6, 2013.

[6] K. T. Mahmood, T. Mugal, and I. U. Haq, "Moringa oleifera: a natural gift-A review," *J. Pharm. Sci. Res.*, vol. 2, no. 11, p. 775, 2010.

[7] R. I. Castillo-López, J. León-Félix, M. Á. Angulo-Escalante, R. Gutiérrez-Dorado, M. D. Muy-Rangel, and J. B. Heredia, "Nutritional and phenolic characterization of moringa Oleifera leaves grown in Sinaloa, México," *Pakistan J. Bot.*, vol. 49, no. 1, pp. 161–168, 2017.

[8] R. K. Saini, I. Sivanesan, and Y. S. Keum, "Phytochemicals of Moringa oleifera: a review of their nutritional, therapeutic and industrial significance," *3 Biotech*, vol. 6, no. 2, pp. 1–14, 2016, doi: 10.1007/s13205-016-0526-3.

[9] Bichi M., "A review of the applications of Moringa oleifera seeds extract in water treatment," *Civ. Environ. Res.*, vol. 3, no. 8, pp. 1–11, 2013.

[10] H. P. S. Makkar and K. Becker, "Nutrients and antiquality factors in different morphological parts of the Moringa oleifera tree," *J. Agric. Sci.*, vol. 128, no. 3, pp. 311–322, 1997, doi: 10.1017/S0021859697004292.

[11] A. Sandeep, G Anitha, T Vijayalatha, KR Sadasakthi, “Moringa for nutritional security (Moringa oleifera Lam .),” *Int. J. Bot. Stud.*, vol. 4, no. 1, pp. 21–24, 2019.

[12] E. Chukwuebuka, “Moringa oleifera‘The Mother’s Best Friend,’” *Int. J. Nutr. Food Sci.*, vol. 4, no. 6, p. 624, 2015, doi: 10.11648/j.ijnfs.20150406.14.

[13] T. Tshabalala, E. M. Abdel-Rahman, B. Ncube, A. R. Ndhlala, and O. Mutanga, “Leveraging of hyperspectral remote sensing on estimating biomass yield of Moringa oleifera Lam. medicinal plant,” *South African J. Bot.*, vol. 140, pp. 37–49, 2021, doi: https://doi.org/10.1016/j.sajb.2021.03.035.

[14] C. Cui *et al.*, “Characterization of Moringa oleifera roots polysaccharide MRP-1 with anti-inflammatory effect,” *Int. J. Biol. Macromol.*, vol. 132, pp. 844–851, 2019, doi: 10.1016/j.ijbiomac.2019.03.210.

[15] A. Roloff, H. Weisgerber, U. Lang, and B. Stimm, “Moringa oleifera LAM., 1785,” *Sea*, vol. 10, no. 10, 2009.

[16] A. M. A. Hassanein and A. A. Al-Soqeer, “Morphological and genetic diversity of Moringa oleifera and Moringa peregrina genotypes,” *Hortic. Environ. Biotechnol.*, vol. 59, no. 2, pp. 251–261, 2018, doi: 10.1007/s13580-018-0024-0.

[17] J. A. Parotta, “Moringa oleifera Moringa oleifera,” *Agrofor. Database*, vol. 0, no. November 2017, pp. 4–9, 2009.

[18] T. Radovich, “Farm and forestry production and marketing profile for Moringa (Moringa oleifera),” *Specialty crops for Pacific island agroforestry*. Permanent Agriculture Resources (PAR): Holualoa, HI, USA, 2011.

[19] A. G. Adebayo, H. A. Akintoye, A. O. Shokalu, and M. T. Olatunji, “Soil chemical properties and growth response of Moringa oleifera to different sources and rates of organic and NPK fertilizers,” *Int. J. Recycl. Org. Waste Agric.*, vol. 6, no. 4, pp. 281–287, 2017, doi: 10.1007/s40093-017-0175-5.

[20] S. Gupta, R. Jain, S. Kachhwaha, and S. L. Kothari, “Nutritional and medicinal applications of Moringa oleifera Lam.—Review of current status and future possibilities,” *J. Herb. Med.*, vol. 11, pp. 1–11, 2018, doi: 10.1016/j.hermed.2017.07.003.

[21] S. Mahfuz and X. S. Piao, “Application of moringa(Moringa oleifera) as natural

feed supplement in poultry diets," *Animals*, vol. 9, no. 7, p. 431, 2019, doi: 10.3390/ani9070431.

[22] C. W. Yameogo, M. D. Bengaly, A. Savadogo, P. A. Nikiema, and S. A. Traore, "Determination of chemical composition and nutritional values of Moringa oleifera leaves," *Pakistan J. Nutr.*, vol. 10, no. 3, pp. 264–268, 2011, doi: 10.3923/pjn.2011.264.268.

[23] G. C. Stevens, K. P. Baiyeri, and O. Akinnnagbe, "Ethno-medicinal and culinary uses of Moringa oleifera Lam. in Nigeria," *J. Med. Plants Res.*, vol. 7, no. 13, pp. 799–804, 2013, doi: 10.5897/JMPR12.1221.

[24] Fozia Farooq, "Medicinal properties of Moringa oleifera: An overview of promising healer," *J. Med. Plants Res.*, vol. 6, no. 27, pp. 4368–4374, 2012, doi: 10.5897/jmpr012.279.

[25] A. B. Falowo, F. E. Mukumbo, E. M. Idamokoro, J. M. Lorenzo, A. J. Afolayan, and V. Muchenje, "Multi-functional application of Moringa oleifera Lam. in nutrition and animal food products: A review," *Food Res. Int.*, vol. 106, pp. 317–334, 2018, doi: 10.1016/j.foodres.2017.12.079.

[26] Q. Shamim, P. Jitendra, A. Reddy, S. Safiullah, and P. Mohapatra, "Phytochemicals and Pharmacological Activities of Moringa oleifera Lam.," *Res. J. Pharmacol. Pharmacodyn.*, vol. 2, no. 2, pp. 183-186–186, 2010.

[27] S. Gupta, S. Kachhwaha, S. L. Kothari, M. K. Bohra, and R. Jain, "Surface Morphology and Physicochemical Characterization of Thermostable Moringa Gum: A Potential Pharmaceutical Excipient," *ACS Omega*, vol. 5, no. 45, pp. 29189–29198, 2020, doi: 10.1021/acsomega.0c03966.

[28] F. P. Camacho, V. S. Sousa, R. Bergamasco, and M. Ribau Teixeira, "The use of Moringa oleifera as a natural coagulant in surface water treatment," *Chem. Eng. J.*, vol. 313, pp. 226–237, 2017, doi: 10.1016/j.cej.2016.12.031.

[29] F. U. Ozioko, "Synthesis and Study of Properties of Biolubricant based on Moringa oleifera Oil for Industrial Application," *Au J.T.*, vol. 17, no. 3, pp. 137–142, 2014.

[30] V. Karthickeyan, "Effect of cetane enhancer on Moringa oleifera biodiesel in a thermal coated direct injection diesel engine," *Fuel*, vol. 235, pp. 538–550, 2019,

doi: 10.1016/j.fuel.2018.08.030.

[31] S. Manigandan *et al.*, “Performance, noise and emission characteristics of DI engine using canola and Moringa oleifera biodiesel blends using soluble multiwalled carbon nanotubes,” *Fuel*, vol. 289, p. 119829, 2021, doi: 10.1016/j.fuel.2020.119829.

[32] T. Okuda, A. U. Baes, W. Nishijima, and M. Okada, “Coagulation mechanism of salt solution-extracted active component in Moringa oleifera seeds,” *Water Res.*, vol. 35, no. 3, pp. 830–834, 2001, doi: 10.1016/S0043-1354(00)00296-7.

[33] A. S. T. 2 S Patel 1* and A. C. 2 and A. M. 3, “Moringa Oleifera: A Review of There Medicinal and Economical Importance to ...: EBSCOhost,” *Drug Invent. Today*, vol. 2, no. 7, pp. 339–342, 2010.

OVERVIEW ON NANONPARTICLES

Chapter II: Overview on nanoparticles

Nanoscale science and technology, frequently uttered as “nanoscience” or “nanotechnology,” are simply the science and engineering carried out on the nano-metric scale, that is, 10^{-9} meters.

Nanoscience and nanotechnology today represent one of the most promising fields of research in the material sciences. This field is expected to play a vital role in different disciplines and is becoming the most innovative scientific field.

In recent years, nanoscale materials have attracted the curiosity of researchers due to their unusual and exceptional features over their bulk counterparts. These new features have given this field continuous evolutions by developing new synthesis methods for these nanomaterials of controlled size and shape.

II.1 Historical aspect

Although material manipulation at the atomic and molecular scale to obtain new functions and features appears to be a very recent concept. But there is much evidence that ancient artisans also controlled matter at the tiniest scales, and they have mainly been used for decorative coloring of glass. However, the concept of nanoparticles was unexplained at that time [1].

Investigations using various techniques showed that Celtic red enamels dated from 100 to 400 BC contain copper and cuprous oxide nanocrystals. The metallic particles have been widely used during the Roman period for coloring glass. They have used glass containing a dispersion of copper nanocrystals to synthesize the majority of the red tesserae used in Roman mosaics [2].

Extraordinary work with glass made by the Romans in the fifth century AD demonstrates one of the greatest examples of nanotechnology in the ancient civilizations. The Lycurgus cup, which shows the Greek King Lycurgus being pulled to the underworld. The cup looks green When is illuminated externally (Fig a), when light is shone through it internally turns to a glowing translucent red internally and the King Lycurgus looks purple (Fig (b) [2,3].

The analysis of this cup revealed that it contains a combination of two metal crystals of nanoscale size (~70 nm) i.e., Silver and Gold in a molar ratio of 14:1. The presence of these nanocrystals has given the Lycurgus cup its unique color display [3].

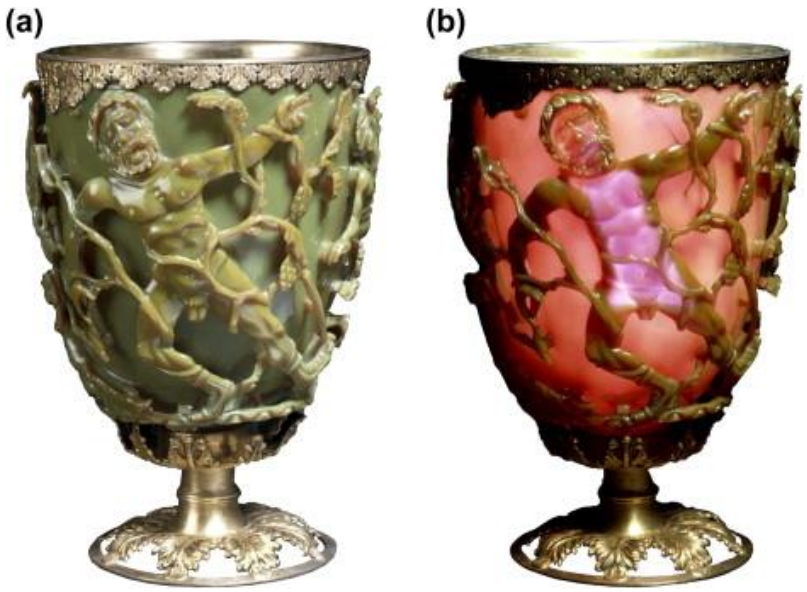

Figure II. 1 Photograph of the famous Lycurgus cup which displays a different color depending on whether it is illuminated externally (a) or internally (b).

The ancient Indian and Chinese have used nano and colloidal gold particles as a medicine named "Suvarna Bhasma" to treat different diseases such as diabetes, rheumatoid arthritis, and nervous system-related diseases [4].

Despite the prementioned applications, nanoparticles in their modern concept were unexplained at the time.

In 1857, the American physicist and Nobel Prize Faraday made an exceptional work on colloidal gold, which introduced the concept of metallic nanoparticles igniting a revolution in the nanotechnology world [5].

At a lecture in 1959, Richard Feynman famously said, “the principles of physics, as far as I can see, do not speak against the possibility of maneuvering things atom by atom”. With this declaration, Feynman proposed to the scientific community to explore the universe at the tiniest scale. Fifteen years later, the term “nanotechnology” was originally introduced by the Japanese scientist Norio Taniguchi in 1974 [6].

Table II. 1 summarizes an outline of the historical background in connection with nanoparticles (nanotechnology) [3].

Table II. 1Chronological table of nanotechnology [3].

Year	Remarks	Country/people
1200–1300 BC	Discovery of soluble gold	Egypt and China
290–325 AD	Lycurgus cup	Alexandria or Rome
1618	First book on colloidal gold	F. Antonii
1676	Book published on drinkable gold that contains metallic gold in neutral media	J. von Löwenstern-Kunckel (Germany)
1718	Publication of a complete treatise on colloidal gold	Hans Heinrich Helcher
1857	Synthesis of colloidal gold	M. Faraday (The Royal Institution of Great Britain)
1902	Surface plasmon resonance (SPR)	R. W. Wood (Johns Hopkins University, USA)
1908	Scattering and absorption of electromagnetic fields by a nanosphere	G. Mie (University of Göttingen, Germany)
1931	Transmission electron microscope (TEM)	M. Knoll and E. Ruska (Technical University of Berlin, Germany)
1937	Scanning electron microscope (SEM)	M. von Ardenne (Forschungslaboratorium für Elektronen-physik, Germany)
1959	Feynman's Lecture on "There's Plenty of Room at the Bottom"	R. P. Feynman (California Institute of Technology, Pasadena, CA, USA)
1960	Microelectromechanical systems (MEMS)	I. Igarashi (Toyota Central R&D Labs, Japan)
1960	Successful oscillation of a laser	T. H. Maiman (Hughes Research Laboratories, USA)
1962	The Kubo effect	R. Kubo (University of Tokyo, Japan)
1965	Moore's Law	G. Moore (Fairchild Semiconductor Inc., USA)
1969	The Honda–Fujishima effect	A. Fujishima and K. Honda (University of Tokyo, Japan)
1972	Amorphous heterostructure photodiode created with bottom-up process	E. Maruyama (Hitachi Co. Ltd., Japan)

1974	Concept of nanotechnology proposed	N. Taniguchi (Tokyo University of Science, Japan)
1976	Carbon nanofiber	M. Endo (Shinshu University, Japan)
1976	Amorphous silicon solar cells	D. E. Carlson and C. R. Wronski (RCA, USA)
1980	Quantum hall effect (Nobel Prize)	K. von Klitzing (University of Würzburg, Germany)
1982	Scanning tunneling microscope (STM) (Nobel Prize)	G. Binnig and H. Rohrer (IBM Zurich Research Lab., Switzerland)
1986	Atomic force microscope (AFM)	G. Binnig (IBM Zurich Research Lab., Switzerland)
1986	Three-dimensional space manipulation of atoms demonstrated (Nobel Prize)	S. Chu (Bell Lab., USA)
1987	Gold nanoparticle catalysis	M. Haruta (Industrial Research Institute of Osaka, Japan)
1990	Atoms controlled with scanning tunneling microscope (STM)	D. M. Eigler (IBM, USA)
1991	Carbon nanotubes discovered	S. Iijima (NEC Co., Japan)
1992	**Japan's National Project on Ultimate Manipulation of Atoms and Molecules begins**	
1995	Nano-imprinting	S. Y. Chou (University of Minnesota, USA)
1996	Nano sheets	T. Sasaki (National Institute for Research in Inorganic Materials, Japan)
2000	National Nanotechnology Initiative (NNI), USA	
2003	21st Century Nanotechnology Research and Development Act, USA	
2005	Nanoscience and Nanotechnologies: An action plan, Europe	

II.2 Definitions

The prefix "nano" is a Greek word that means dwarf or miniature. The International System (SI) of units considers nano as a prefix to indicate 10^{-9} part of a unit. Nanoscience is the science that is specifically interested in exploring and studying the properties of matter at the nanoscale (100 nm or less). It concentrates on the unusual and unique, size-dependent properties of solid-state materials [7].

II.2.1 Nanotechnology

Nanotechnology, or nanotech, is the manipulation of matter at the nanoscale from 1 to 100 nanometers, in order to take advantage of their exceptional features and employing them for industrial purposes [8].

II.2.2 Nanomaterials

Nanomaterials are defined as materials which at least have one dimension in the nanoscale range. They can be produced from the destruction of a macroscopic material, or by the development of a group of atoms or molecules. These nanomaterials can have different shapes such as (nanospheres, nanotubes, nanowires, cells, and single crystals...). [9] Nanostructured materials then have specific mechanical, electrical, magnetic, optical, and catalytic properties that may differ from their bulk counterpart [10].

II.2.3 Nanoparticles

A nanoparticle is an assembly of a few hundred to a few thousand atoms, forming an object with at least one dimension between 1 and 100 nm. Therefore, Nanoparticles are located in between the macroscopic and molecular scales. Comparing to natural organic structures, nanoparticles size is mainly in the range corresponding to proteins [11]. Most materials at the micrometer scale have the same physical properties as solid material. Meanwhile, at the nanometric scale, they can have distinctly different physical properties from their larger counterparts. Nanoparticles are of great interest due to their extremely small size and high surface area to volume ratio, producing differences in chemical and physical properties. These differences give special characteristics to nanoparticles. Making nanoparticles the building blocks of the next generation in many fields, such as chemistry, physics, electronics, mechanics, and biotechnology [12,13].

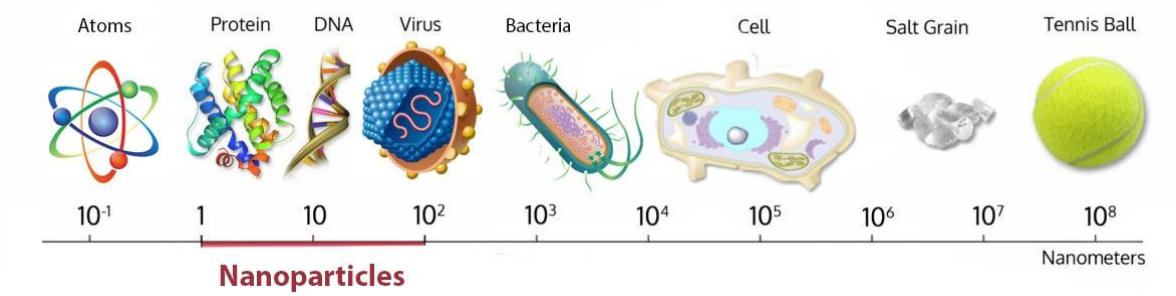

Figure II. 2 The range of nanoparticle sizes compared to major chemical and biological structures [14].

II.2.3.1 Classifications of nanoparticles

Nanomaterials can be classified into different groups based on various criteria. Generally, Nanoparticles are categorized according to three major aspects: their dimensions, origin (natural or anthropogenic), and chemical compositions [15].

II.2.3.1.1 Classifications of nanoparticles according to their dimensions

II.2.3.1.1.1. Zero-dimensional nanoparticles

Nanoparticles of 0 dimensions (0D) are the most popular type of nanomaterials. These nanoparticles are point-like particles in a range less than 100 nm in size. The most popular particles in this dimension are quantum dots, hollow spheres, and nano lenses [16,17].

II.2.3.1.1.2. One-dimensional nanoparticles

Nanoparticles of 1 dimension (1D) are the particles that have at least one dimension larger than nanoscale and the other dimensions within nano range. The most popular examples in this dimension are nanofibers, nanotubes, and nanorods [16,17].

II.2.3.1.1.3. Two-dimensional nanoparticles

Nanomaterials of 2 dimensions (2D) are the materials that have two dimensions larger than nanoscale with plate-like structures. The most popular examples in this dimension are nanofilms, nanolayers, and nanocoating [16,17].

II.2.3.1.1.4. Three-dimensional nanoparticles

Nanoparticles of 3 dimensions (3D) have all three dimensions larger than nanoscale. However, they're formed based on nanoscale particles that are combined to build three-dimensional nanomaterials. The most popular in this dimension are nanocomposites, bundles of nanofibers, multi nanolayer-type structures [16,17].

II.2.3.1.2 Classifications of nanoparticles according to their origin

II.2.3.1.2.1. Natural nanoparticles

A considerable percentage of nanoparticles present in the environment are of natural origin. Although, their presence in nature is lower compared to the emissions of manufactured nanoparticles. Natural origin nanoparticles are the ultrafine particles that appeared from natural phenomena such as forest fires, volcanic eruptions, and thunderbolts. They have been an essential part of the environment since the origin of the planet [15].

II.2.3.1.2.2. Anthropogenic nanoparticles

Anthropogenic nanoparticles fall into two broad categories: accidental nanoparticles and engineered nanoparticles. Accidental nanoparticles are of heterogeneous size and shape, commonly generated by the combustion of fossil fuels (gasoline, diesel, coal, and propane) or large-scale mining. Engineered nanoparticles are specifically designed particles with precisely controlled sizes, shapes, and compositions. They can even contain multiple layers, for example, a gold nanoparticle coated with porous silica nanoparticles loaded with drugs and coated [15].

II.2.3.1.3 Classifications of nanoparticles according to their chemical compositions

Nanoparticles are chemically categorized into three main categories organic, inorganic, and carbon-based nanoparticles.

II.2.3.1.3.1 Organic nanoparticles

Organic nanoparticles are biodegradable, non-toxic materials of two or more dimensions, with a size in the range of 1–100 nm. The main groups of organic nanoparticles or polymers are dendrimers, micelles, liposomes, and ferritin. These nanoparticles are sensitive to electromagnetic and thermal radiation making them an excellent alternative for drug delivery. Due to these unique properties, organic nanoparticles are commonly used in the biomedical field for targeted drug delivery [18].

II.2.3.1.3.2 Inorganic nanoparticles

Inorganic nanoparticles are particles that are not made of carbon. They can be classified into metals, metal oxides and quantum dots [18].

II.2.3.1.3.3 Metals nanoparticles

Almost all the metals nanoparticles can be synthesized employing destructive or constructive approaches. Metal nanoparticles like gold, copper, silicon, iron, and silver are widely used in many fields as catalysis, electronics, sensors, photonics, environmental remedies, and medicine due to their unique characteristics [18].

II.2.3.1.3.4 Metal oxides nanoparticles

Metal oxides nanoparticles are synthesized to modify the properties of their corresponding metal-based nanoparticles. Different metal oxides have appeared in various forms: nanotubes, nano-rods, nano-flakes, etc. In addition, some structures demonstrate interesting properties for virtual applications in fields such as sensors, optoelectronics, transducers, medicine [18].

II.2.3.1.3.5 Quantum dots

Quantum dots have been an important area of research for the past twenty years, they have been developed used in semiconductors, insulators, metals, magnetic materials, or metal oxides. The number of atoms in a quantum dot, ranging from 1000 to 100000 does not make it an extended solid structure or a single molecular entity. [19] The flexibility of quantum dots and their associated optical properties makes it favorable for many applications in fields such as multi-color optical coding, in the study of gene expression, in high resolution and high-speed displays, and in medical imaging [20].

II.2.3.1.3.6 Carbon-based nanoparticles

The nanoparticles made entirely of carbon are known as carbon-based.

a) **Fullerenes**

Fullerenes (C_{60}) is the most studied form in carbon-based nanoparticles, first synthesized in 1985 by Kroto et al, [21] is a molecule containing 60 carbon atoms, spherical in shape similar to a soccer ball with 12 pentagon shapes and 20 hexagonal shapes. Although it is considered as structures containing 28 to 1500 carbon atoms and up to 8.2 nm in diameter [22].

b) Graphene

Graphene is a hexagonal network of honeycomb lattices made up of carbon atoms on a two-dimensional flat surface. In general, the thickness of the graphene sheet is about 1 nm. [18]

c) Carbon nanotubes (CNTs)

Carbon nanotubes (CNTs) are a new crystalline form of carbon. Twisted in a hexagonal network of carbon atoms forming a graphene nanosheet, these hollow cylinders can have diameters as small as 0.7 nm and reach several millimeters in length. Each end can be opened or closed by half a fullerene molecule [18].

d) Carbon Nanofiber

The same graphene nanosheets are used to produce carbon nanofibers like carbon nanotubes but coiled into a cone or cup shape instead of regular cylindrical tubes [18].

e) Carbon black

Carbon black consists of partially amorphous graphitic material in which a substantial fraction of the elementary particles is nanometric in size, usually 20 to 70 nm. The interaction between the particles is so strong that they bind together in aggregates and form agglomerates of around 500 nm [18].

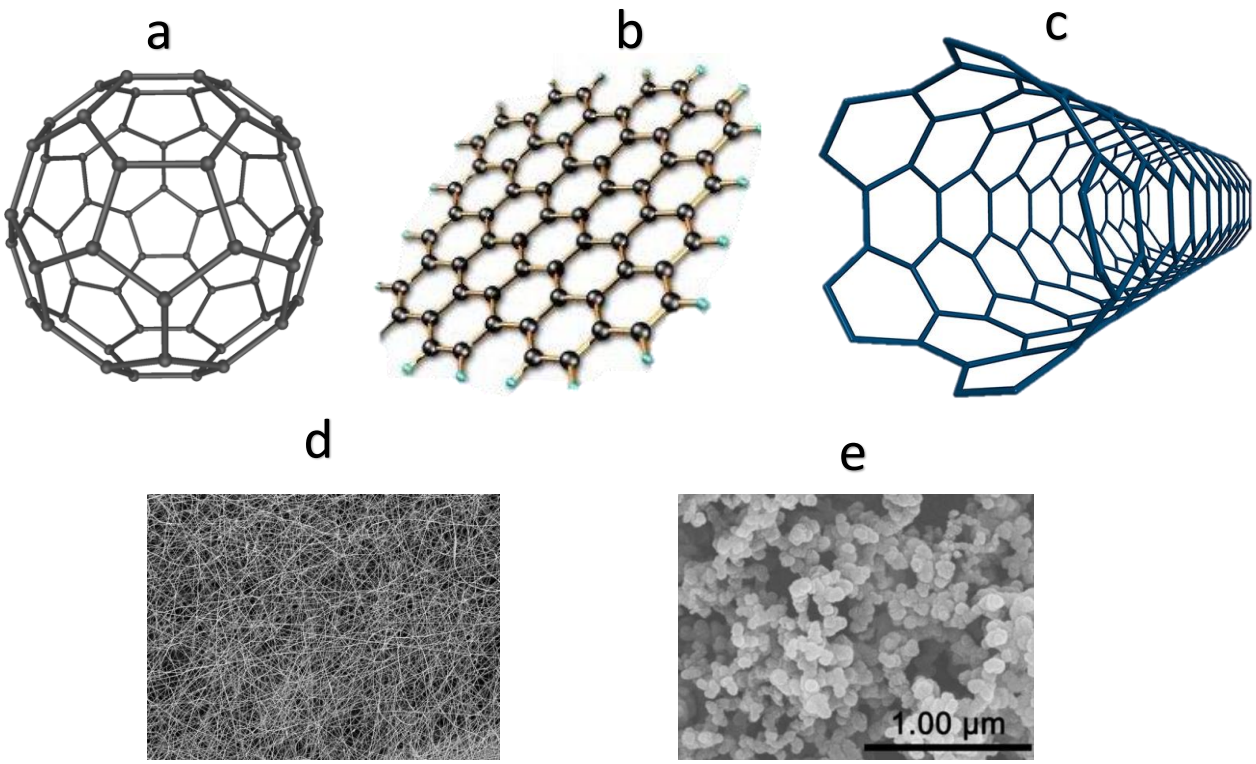

Figure II. 3 Carbon-based nanoparticles: a – fullerenes, b – graphene, c – carbon nanotubes, d – nanofiber, and e– carbon [18].

II.2.3.2 The properties of nanoparticles

II.2.3.2.1 Optical properties

Nanoparticle's optical properties such as transmission, absorption, reflection, and light emission are dynamic and completely different from their same counterpart bulk material. The electrons in nanoparticles react differently with light compared to their bulk material. The minute size of a nanoparticle limits the free motion of electrons, unlike in the case of bulk material, causing quantum confinement of electrons [23,24].

Numerous optical properties suitable for different fields are produced by simply modifying the particle's shape, size, and surface functionality. These modifications affect the color that nanoparticles appear. For example, gold spherical nanoparticles of 100 nm diameter have an orange color. Meanwhile, the same nanometric metal in the range of 25 nm looks green. Similarly, the spherical gold particles of 100 nm have an orange color while spherical silver nanoparticles of the same size 100 nm have a yellow color [23].

Nanoparticles have specific properties which are attributed in particular to the large proportion of atoms present at the surface compared to the number of core atoms. Assuming that the nanoparticles have a spherical shape, the ratio of their surface area to volume increases as the particle size decreases. (Table II.1).

II.2.3.2.2 Surface properties

Since the particle's reactive area is on its surface, the surface effect is no longer negligible compared to the volume. In the macroscopic dimension, the surface atoms of particles are negligible compared to the set of atoms composing the particles. In this case, the surface atoms do not influence the properties of the particles. In contrast, when the size of the particles decreases to a nanometric scale, the proportion of atoms on the surface is significant and plays a vital role in changing the properties of the nanoparticles [24,25].

Table II. 2 Some example calculations for volume and surface area of nanoparticles.

Nanoparticle	**Volume**	**Surface Area**	**SA:Vol Ratio**
Diameter (nm)	(nm^3)	(nm^2)	(nm^2/nm^3)
1	0.524	3.14	6
10	524	314	0.6
100	523598	31416	0.06
1000	5.24E+08	3.14E+06	0.006
10000	5.24E+11	3.14E+08	0.0006
100000	5.24E+14	3.14E+10	0.00006
1000000	5.24E+17	3.14E+12	0.000006

II.2.3.2.3 Electronic properties

The electrical resistance increases when the size of the particles decreases. This is explained by the large proportion of atoms at the surface of the particle. Therefore, the electronic properties of nanoparticles are classified between the atoms that exhibit discrete states and bulk materials that exhibit an electronic structure in energy bands [26].

II.2.3.2.4 Mechanical properties

In the nanometric scale of materials, various enhancements are expected in their mechanical properties such as bending strength, Young's modulus (or Elastic Modulus), tensile strength, fracture properties, and impact resistance. Nanoparticle's mechanical properties depend on the material base. Carbon-based materials occupy extremely high mechanical strength [27].

II.2.3.3 Approaches for the synthesis of nanoparticles

Over the past ten years, many methods have been developed to manufacture nanomaterials. Choosing the suitable method for nanoparticles synthesis is based on several criteria, such as the conditions and synthesis methods.

From an industrial point of view, cost, duration, and reproducibility represent the most important criteria. Generally, there are two main approaches for nanoparticles synthesis bottom-up and top-down. Although both approaches play a vital role in the fabrication of nanoparticles, each has advantages and disadvantages [28].

II.2.3.3.1 The bottom-up approach

The bottom-up approach means building material from the "bottom". It consists of building nano-objects and nanomaterials atom by atom, molecule by molecule, or aggregate by aggregate. The assembly or positioning of atoms, molecules, or aggregates is carried out in a precise and controlled manner, in order to obtain perfectly controlled nanomaterials, with the desirable properties.

The most frequently used bottom-up methods for nanoparticle synthesis are pyrolysis, sol-gel, spinning, chemical vapor deposition, and biosynthesis [29].

II.2.3.3.2 The top-down approach

This method is also known as the destructive method that reduces the bulk material size to nanometric scale particles of the desired shape and size. It uses mainly mechanical processes. This method is slow, expensive, and not agreeable for the large-scale production of nanoparticles.

The most frequently used bottom-up methods for nanoparticle synthesis are nanolithography, laser ablation, mechanical milling, sputtering and thermal decomposition [29,30].

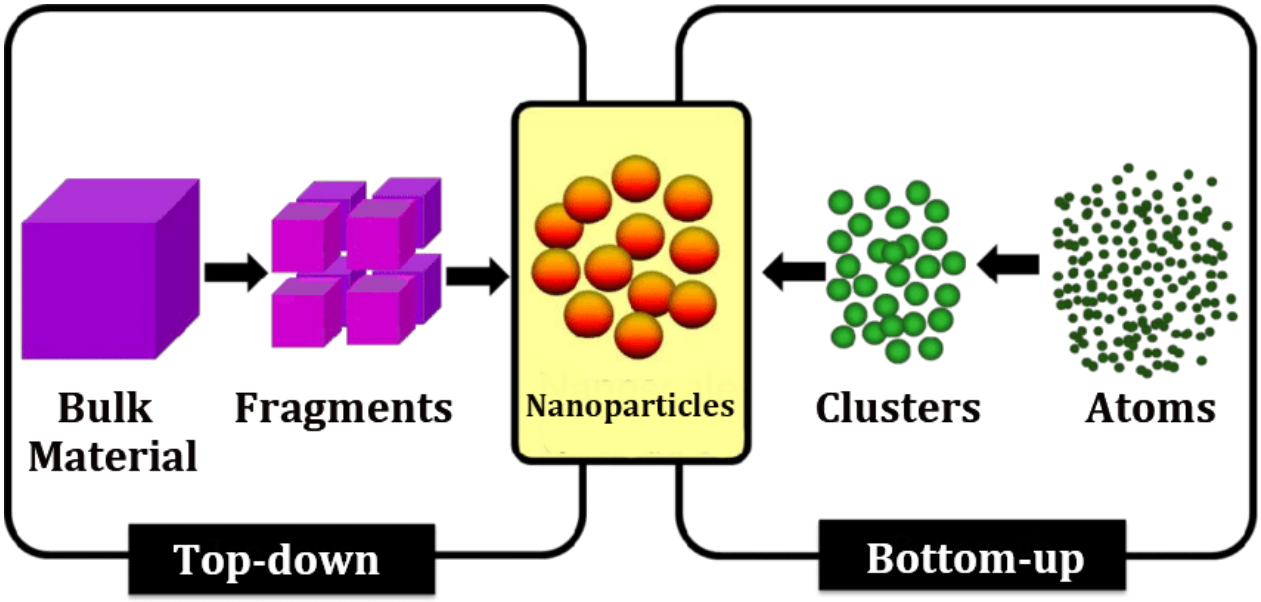

Figure II. 4 Top-down and Bottom-up approaches for nanoparticles synthesis.

II.2.3.3.3 Thermal decomposition

The thermal decomposition method consists of using heat to break the chemical bonds in the compound. Each element has a specific temperature which is called decomposition temperature. It's the temperature when the compound decomposes chemically. Due to this decomposition, nanoparticles are produced [31].

II.2.3.3.4 Laser ablation

Laser ablation involves concentrating a high-energy laser beam at a target to vaporize a part of that target and then condense the particles obtained on a substrate. The produced nanocrystals grow by condensing the species emitted by the target. The growth also occurs in a gas phase in a well-defined pressure range. The size of these nanoparticles depends on the nature of the carrier gas, its pressure, and the intensity of the laser beam [32].

II.2.3.3.5 Sol-gel

Sol-gel is a widely used method for the synthesis of high-quality metal oxides nanoparticles. It's known for its great ability to control the texture and surface of the produced nanomaterials. the essential steps for this method consist of dispersing the precursor with a host solvent by stirring or sonication or shaking to form a colloidal solution composed of liquid and solid phases. these two phases are separated by different methods such as sedimentation, filtration, and centrifugation [33].

II.2.3.3.6 Chemical Vapor Deposition

Chemical Vapor Deposition (CVD) is a method that produces uniform, hard, and highly pure nanoparticles. This method consists of deposing reactants thin layer above a substrate. The deposing process is executed in a reaction chamber at ambient temperature by merging gas molecules. When the heated substrate contacts with the combined gas, a chemical reaction take place to produce a thin film of product on the substrate surface. The product is then collected and applied for the desired application [34]. Worth noting that this method requires special equipment and the produces gases are highly toxic, which is considered a disadvantage for this method [35].

II.2.3.3.7 Sputtering

The sputtering method consists of deposing nanoparticles on a surface. This deposing is executed by ejecting these particles from the surface by colliding with ions. [36] This method is usually based on two steps, deposition of the nanoparticles' thin layer, followed by thermal treatment or annealing. Nanoparticles' properties, size, and shape are highly influenced by the annealing temperature, annealing duration, and substrate type [37].

II.2.3.3.8 pyrolysis

The pyrolysis method is widely used in industries due to its efficiency for the largescale production of nanoparticles. It is a continuous process that produces a very high yield at a low cost.[38] This method involves burning a liquid or vapor precursor with flame by inserting it in a furnace at high pressure through a small gap. The combustion of the gas state by-products is then air classified to recover the nanoparticles. In order to facilitate

evaporation, some furnaces use other techniques such as laser and plasma instead of flame [39].

II.2.3.3.9 Biosynthesis

Biosynthesis or green synthesis method is an approach that uses plant extracts, bacteria, fungi added to the precursors to synthesize nanoparticles. This method is extremely cheap and does not require chemicals or toxic materials; therefore, it is considered a cost-effective and eco-friendly approach that produces non-toxic, biodegradable nanoparticles. The nanoparticles synthesized from this method are widely applicated in biomedical applications due to their safety [40].

II.2.3.4 The applications of nanoparticles

Nanomaterials generally and nanoparticles specifically are applied in different fields due to their exceptional properties. Below are some of the main applications of nanoparticles.

II.2.3.4.1 Catalysis

One of the most critical applications of nanoparticles is employing them as a catalyst. Nanoparticles possess a huge surface-to-volume ratio, which is widely exploited in the production of chemicals. The automotive catalytic converters are one of the most important examples of using nanoparticles as catalysts. They use platinum nanoparticles instead of the bulk platin, reducing the amount of platin used, improving the performance, and significantly reducing the cost [41].

II.2.3.4.2 Electronics

The increasing demand for mobile devices nowadays, such as smartphones and laptop computers, has caused a big challenge for manufacturing compact, lightweight electronic compounds and higher-capacity batteries. Nanoparticles have been widely used in electronics to synchronize this need for smaller and more efficient electronic compounds. They have been used as separator plates in modern batteries that significantly decreased their size and weight and increased their ability to store more energy than traditional batteries[42].

II.2.3.4.3 Medicine

Nanoparticles have made revolutionary improvements in the medical field due to their new features. They are widely employed for drug delivery, facilitating diagnostics, and early detection of disease. Nanoparticles made it possible to deliver a drug to a specific cell

with the required dosage, which reduced the total drug consumption and the side effects significantly [43,44].

II.2.3.4.4 Food

Nanotechnology is widely applied in food in many aspects; it has significantly improved food production, protection, processing, and packing. Nanocomposites prevent food from microorganisms by coating it with a film nanolayer in the food packing process. Nanoparticles are also used as convertive additives and pigments in the food industry [45].

II.2.3.4.5 Environmental

Nanotechnology has played a vital role in preventing various serious hazards and provided very efficient and reliable solutions for diverse environmental challenges. Nanoparticles are to prevent water, soil and air pollution. They have proven their efficiency in water treatment such as disinfection, purification, desalination, and removing contaminants like heavy metals, pathogens, and organic pollutants without using chemicals [46]. The nanoparticles are also utilized to clean up and absorb oil spills due to their high surface-to-volume ratio, which worldwide environmental concern. Soil contamination is also treated by injecting nanoparticles into the precise location that contains toxic industrial waste or heavy metals. Nanofiltration membranes are used to limit toxic contaminant emissions from the industrial stacks that reduce air pollution [18].

II.2.3.5 Iron oxide nanoparticles (IONPs)

There are many forms of iron oxides in nature; however, magnetite (Fe_3O_4), maghemite (γ-Fe_2O_3), and hematite (α-Fe_2O_3) are the most common forms. These three forms of iron oxide are of great technological and industrial interest due to their unique properties. Table II. 3 summarizes some of their physical and magnetic properties [47].

Hematite is the frequently used name for iron oxide with the formula (α-Fe_2O_3); it is also known as ferric oxide, red ochre, martite, specularite, specular iron ore, or kidney ore. Hematite is considered the first discovered form of iron oxide on the earth's surface. It is usually obtained in soils and sedimentary rocks. Hematite color is blood-red if finely divided; on the other hand, its color will be black or grey if coarsely crystalline. It is the most stable iron oxide since it is the final product of other iron oxides transformations [48].

Table II. 3 Physical and magnetic properties of iron oxide [48].

Property	**Iron Oxide**		
	Hematite	Magnetite	Maghemite
Molecular formula	α-Fe_2O_3	Fe_3O_4	γ-Fe_2O_3
Density (g/cm³)	5.26	5.18	4.87
Melting point (°C)	1350	1583-1597	-
Hardness	6.5	5.5	5
Type of magnetism	Weakly ferromagnetic or antiferromagnetic	Ferromagnetic	Ferrimagnetic
Crystallographic system	Rhombohedral, hexagonal	Cubic	Cubic or tetrahedral
Structural type	Corundum	Inverse spinel	Defect spinel
Space group	R3c (hexagonal)	Fd3m	P4332 (cubic); P41212 (tetragonal)
Lattice parameter (nm)	a = 0.5034 nm, c = 1.375 nm (hexagonal) a Rh = 0.5427, a = 55.3° (rhombohedral)	a = 0.8396 nm	a = 0.83474 (cubic); a = 0.8347, c = 2.501 nm (tetragonal)

Meanwhile, magnetite of the formula Fe_3O_4 exhibits the most vital magnetism properties of the three iron oxides. Magnetite is also called ferrous ferrite, black iron oxide, loadstone, magnetic iron ore. The third type of iron oxide, maghemite (γ-Fe_2O_3), is a weathering product of magnetite, which rises from the contact of magnetite with water or atmospheric gases [48].

All the three prementioned iron oxides have a close-packed plane crystal structures, constituting oxygen anions and iron cations located at octahedral or tetrahedral interstitial sites. In hematite, iron Fe (III) ions conquer octahedral sites; meanwhile, oxygen ions are arranged in a hexagonal close-packed manner Figure II. 5.

The other two iron oxides, magnetite, and maghemite have a similar oxygen ions arrangement, a cubic, close-packed arrangement. However, they differ in iron ions distribution since magnetite is distinguished from most iron oxides by its possession of divalent and trivalent iron [48,49].

In the case of magnetite, Fe^{+2} ions are located at the center of the octahedral sites. Meanwhile, Fe^{+3} ions occupy the rest of the octahedral sites added to the tetrahedral sites. Differently, maghemite contains only Fe^{+3} ions, which fill both the octahedral and tetragonal sites [49].

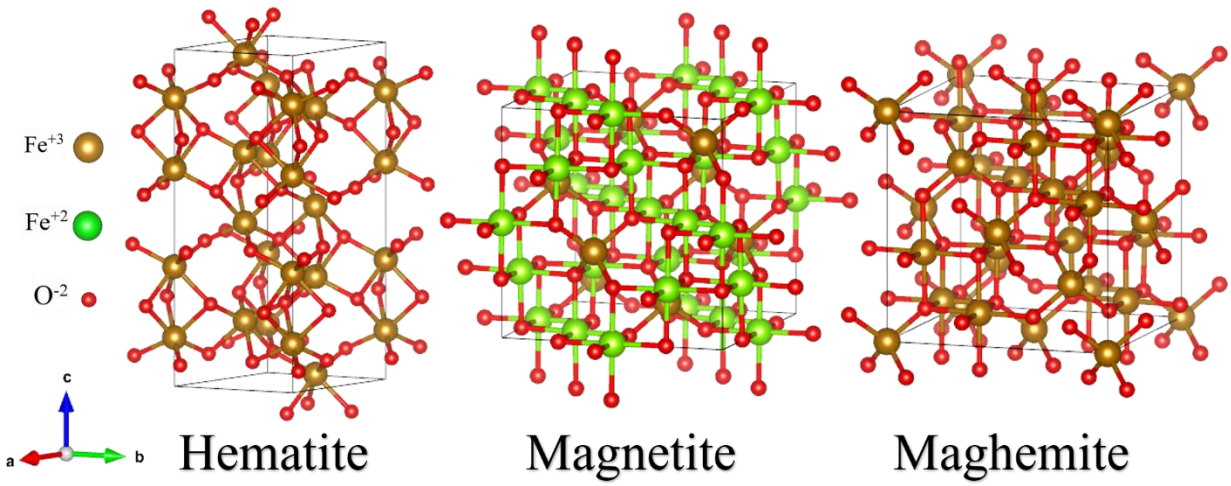

Figure II. 5 Crystal structures of hematite, magnetite, and maghemite

II.2.3.5.1 The applications of iron oxides nanoparticles

Data storage applications require particles of switchable magnetic properties that resist high temperatures and possess high stability. In order to optimize the recording performance, the particles size should be significantly minimized and not affected by corrosion or friction. Iron oxides in general, maghemite in specific, are of great interest for data storage applications due to their chemical and physical stability, making them the perfect material for data storage requirements. IONPs are also used in many modern electronics such as semiconductor materials, transistors, batteries, and gas sensors [48].

Numerous industrial sectors have employed magnetite and hematite as catalysts to facilitate chemical reactions. Ammonia gas production uses IONPs catalysts, also used for oil refining processes such as dehydrogenation of ethylbenzene and large-scale butadiene production [50]. Iron oxides nanoparticles' properties, such as low toxicity and biodegradability, have been widely exploited in biomedical applications. The magnetic properties of IONPs enable controlling them externally by a magnetic field, which is widely used in advanced bio-assays [48,51].

Thanks to iron oxides nanoparticles, major improvements have been applied to magnetic resonance imaging (MRI) to be one of the most efficient imaging tools used in clinical radiology. These significant improvements involve enhancements in contrast and signal amplification [51].

Iron oxides nanoparticles have made revolutionary improvements in medical applications, especially drug delivery. They have intensively been used as drug delivery vehicles that are loaded with therapeutics and then controlled externally by a magnetic field to deliver the loaded therapeutics to a specific cell with the required dosage, which reduced the total drug consumption and the non-desired side effects significantly. They have proven their antioxidant and antibacterial activity, besides their contribution to healing cancer by using them for labeling, detecting, and tracking cancer cells [51,52].

References

[1] A.K. Singh, Introduction to Nanoparticles and Nanotoxicology, in: A.K.B.T.-E.N. Singh (Ed.), Eng. Nanoparticles, Academic Press, Boston, 2016: pp. 1–18. https://doi.org/10.1016/b978-0-12-801406-6.00001-7.

[2] A.A. Hashim, ed., The Delivery of Nanoparticles, InTechOpen, 2012. https://doi.org/10.5772/2647.

[3] S. Horikoshi, N. Serpone, Introduction to Nanoparticles, Microwaves Nanoparticle Synth. Fundam. Appl. (2013) 3–4. https://doi.org/10.1002/9783527648122.ch1.

[4] S. Biswas, M. Chawda, K. Thakur, R. Gudi, J. Bellare, Physicochemical Variation in Nanogold-Based Ayurved Medicine Suvarna Bhasma Produced by Various Manufacturers Lead to Different In Vivo Bioaccumulation Profiles, J. Evidence-Based Integr. Med. 26 (2021) 2515690X211011064. https://doi.org/10.1177/2515690X211011064.

[5] M. Faraday, X. The Bakerian Lecture. —Experimental relations of gold (and other metals) to light, Philos. Trans. R. Soc. London. 147 (1857) 145–181. https://doi.org/10.1098/rstl.1857.0011.

[6] S. Bayda, M. Adeel, T. Tuccinardi, M. Cordani, F. Rizzolio, The History of Nanoscience and Nanotechnology: From Chemical-Physical Applications to Nanomedicine, Molecules. 25 (2019) 112. https://doi.org/10.3390/molecules25010112.

[7] M. Boholm, The use and meaning of nano in American English: Towards a systematic description, Ampersand. 3 (2016) 163–173. https://doi.org/https://doi.org/10.1016/j.amper.2016.10.001.

[8] P. Mulvaney, Nanoscience vs nanotechnology-defining the field, ACS Nano. 9 (2015) 2215–2217. https://doi.org/10.1021/acsnano.5b01418.

[9] N. Baig, I. Kammakakam, W. Falath, I. Kammakakam, Nanomaterials: A review of synthesis methods, properties, recent progress, and challenges, Mater. Adv. 2 (2021) 1821–1871. https://doi.org/10.1039/d0ma00807a.

[10] T.M. Laid, K. Abdelhamid, L.S. Eddine, B. Abderrhmane, Optimizing the

biosynthesis parameters of iron oxide nanoparticles using central composite design, J. Mol. Struct. (2020) 129497. https://doi.org/10.1016/j.molstruc.2020.129497.

[11] D.H. Samak, Y.S. El-Sayed, H.M. Shaheen, A.H. El-Far, M.E. Abd El-Hack, A.E. Noreldin, K. El-Naggar, S.A. Abdelnour, E.M. Saied, H.R. El-Seedi, L. Aleya, M.M. Abdel-Daim, Developmental toxicity of carbon nanoparticles during embryogenesis in chicken, Environ. Sci. Pollut. Res. 27 (2020) 19058–19072. https://doi.org/10.1007/s11356-018-3675-6.

[12] S. Iravani, Green synthesis of metal nanoparticles using plants, Green Chem. 13 (2011) 2638–2650. https://doi.org/10.1039/c1gc15386b.

[13] M. Gartner, M. Crisan, A. Jitianu, R. Scurtu, R. Gavrila, I. Oprea, M. Zaharescu, Spectroellipsometric Characterization of Multilayer Sol-Gel Fe 2 O 3 Films, J. Sol-Gel Sci. Technol. 26 (2003) 745–748. https://doi.org/10.1023/A:1020706423230.

[14] S.K. Brar, M. Verma, R.D. Tyagi, R.Y. Surampalli, Engineered nanoparticles in wastewater and wastewater sludge - Evidence and impacts, Waste Manag. 30 (2010) 504–520. https://doi.org/10.1016/j.wasman.2009.10.012.

[15] T.A. Saleh, Nanomaterials: Classification, properties, and environmental toxicities, Environ. Technol. Innov. 20 (2020) 101067. https://doi.org/10.1016/j.eti.2020.101067.

[16] S. Bhatia, Nanoparticles Types, Classification, Characterization, Fabrication Methods and Drug Delivery Applications, in: Nat. Polym. Drug Deliv. Syst., Springer, 2016: pp. 33–93. https://doi.org/10.1007/978-3-319-41129-3_2.

[17] J. Jeevanandam, A. Barhoum, Y.S. Chan, A. Dufresne, M.K. Danquah, Review on nanoparticles and nanostructured materials: history, sources, toxicity and regulations, Beilstein J. Nanotechnol. 9 (2018) 1050–1074.

[18] A.M. Ealias, M.P. Saravanakumar, A review on the classification, characterisation, synthesis of nanoparticles and their application, IOP Conf. Ser. Mater. Sci. Eng. 263 (2017) 032019. https://doi.org/10.1088/1757-899X/263/3/032019.

[19] R.J. Aitken, M.Q. Chaudhry, A.B.A. Boxall, M. Hull, Manufacture and use of nanomaterials: Current status in the UK and global trends, Occup. Med. (Chic. Ill). 56 (2006) 300–306. https://doi.org/10.1093/occmed/kql051.

[20] X. Michalet, F.F. Pinaud, L.A. Bentolila, J.M. Tsay, S. Doose, J.J. Li, G. Sundaresan, A.M. Wu, S.S. Gambhir, S. Weiss, Quantum dots for live cells, in vivo imaging, and diagnostics, Science (80-.). 307 (2005) 538–544. https://doi.org/10.1126/science.1104274.

[21] H.W. Kroto, J.R. Heath, S.C. O'Brien, R.F. Curl, R.E. Smalley, C 60: buckminsterfullerene, Nature. 318 (1985) 162–163. https://www.nature.com/articles/318162a0.

[22] N. Sano, H. Wang, I. Alexandrou, M. Chhowalla, K.B.K. Teo, G.A.J. Amaratunga, K. Iimura, Properties of carbon onions produced by an arc discharge in water, J. Appl. Phys. 92 (2002) 2783–2788. https://doi.org/10.1063/1.1498884.

[23] S. Mohan Bhagyaraj, O.S. Oluwafemi, Nanotechnology: The Science of the Invisible, in: S. Mohan Bhagyaraj, O.S. Oluwafemi, N. Kalarikkal, S.B.T.-S. of I.N. Thomas (Eds.), Synth. Inorg. Nanomater., Woodhead Publishing, 2018: pp. 1–18. https://doi.org/10.1016/b978-0-08-101975-7.00001-4.

[24] I. Khan, K. Saeed, I. Khan, Nanoparticles: Properties, applications and toxicities, Arab. J. Chem. 12 (2019) 908–931. https://doi.org/10.1016/j.arabjc.2017.05.011.

[25] C. Bantz, O. Koshkina, T. Lang, H.J. Galla, C.J. Kirkpatrick, R.H. Stauber, M. Maskos, The surface properties of nanoparticles determine the agglomeration state and the size of the particles under physiological conditions, Beilstein J. Nanotechnol. 5 (2014) 1774–1786. https://doi.org/10.3762/bjnano.5.188.

[26] C. Huang, X. Chen, Z. Xue, T. Wang, Effect of structure: A new insight into nanoparticle assemblies from inanimate to animate, Sci. Adv. 6 (2020) eaba1321. https://doi.org/10.1126/sciadv.aba1321.

[27] A. Reghunadhan, N. Kalarikkal, S. Thomas, Chapter 7 - Mechanical Property Analysis of Nanomaterials, in: S. Mohan Bhagyaraj, O.S. Oluwafemi, N. Kalarikkal, S.B.T.-C. of N. Thomas (Eds.), Micro Nano Technol., Woodhead Publishing, 2018: pp. 191–212. https://doi.org/https://doi.org/10.1016/B978-0-08-101973-3.00007-9.

[28] P. Iqbal, J.A. Preece, P.M. Mendes, Nanotechnology: The "Top-Down" and "Bottom-Up" Approaches, Supramol. Chem. from Mol. to Nanomater. (2012).

[29] A.M. Ealias, M.P. Saravanakumar, A review on the classification, characterisation,

synthesis of nanoparticles and their application, in: IOP Conf. Ser. Mater. Sci. Eng., IOP Publishing, 2017: p. 32019. https://doi.org/10.1088/1757-899X/263/3/032019.

[30] J. Liu, S.Z. Qiao, Q.H. Hu, G.Q. Max Lu, Magnetic Nanocomposites with Mesoporous Structures: Synthesis and Applications, Small. 7 (2011) 425–443. https://doi.org/10.1002/smll.201001402.

[31] M. Salavati-Niasari, F. Davar, N. Mir, Synthesis and characterization of metallic copper nanoparticles via thermal decomposition, Polyhedron. 27 (2008) 3514–3518. https://doi.org/10.1016/j.poly.2008.08.020.

[32] V. Amendola, M. Meneghetti, Laser ablation synthesis in solution and size manipulation of noble metal nanoparticles, Phys. Chem. Chem. Phys. 11 (2009) 3805–3821. https://doi.org/10.1039/b900654k.

[33] S. Mann, S.L. Burkett, S.A. Davis, C.E. Fowler, N.H. Mendelson, S.D. Sims, D. Walsh, N.T. Whilton, Sol-Gel Synthesis of Organized Matter, Chem. Mater. 9 (1997) 2300–2310. https://doi.org/10.1021/cm970274u.

[34] M. Adachi, S. Tsukui, K. Okuyama, Nanoparticle synthesis by ionizing source gas in chemical vapor deposition, Japanese J. Appl. Physics, Part 2 Lett. 42 (2003) L77. https://doi.org/10.1143/jjap.42.l77.

[35] S. Bhaviripudi, E. Mile, S.A. Steiner, A.T. Zare, M.S. Dresselhaus, A.M. Belcher, J. Kong, CVD synthesis of single-walled carbon nanotubes from gold nanoparticle catalysts, J. Am. Chem. Soc. 129 (2007) 1516–1517. https://doi.org/10.1021/ja0673332.

[36] P. Shah, A. Gavrin, Synthesis of nanoparticles using high-pressure sputtering for magnetic domain imaging, J. Magn. Magn. Mater. 301 (2006) 118–123. https://doi.org/10.1016/j.jmmm.2005.06.023.

[37] E. Lugscheider, S. Bärwulf, C. Barimani, M. Riester, H. Hilgers, Magnetron-sputtered hard material coatings on thermoplastic polymers for clean room applications, Surf. Coatings Technol. 108–109 (1998) 398–402. https://doi.org/10.1016/S0257-8972(98)00627-6.

[38] R. D'Amato, M. Falconieri, S. Gagliardi, E. Popovici, E. Serra, G. Terranova, E. Borsella, Synthesis of ceramic nanoparticles by laser pyrolysis: From research to

applications, J. Anal. Appl. Pyrolysis. 104 (2013) 461–469. https://doi.org/10.1016/j.jaap.2013.05.026.

[39] K. Wegner, S.E. Pratsinis, Flame synthesis of nanoparticles, Chim. Oggi. 22 (2004) 27–29. https://doi.org/10.1205/cerd.82.11.1444.52025.

[40] S. Hasan, A Review on Nanoparticles : Their Synthesis and Types, Res. J. Recent Sci. Res . J . Recent . Sci . Uttar Pradesh (Lucknow Campus). 4 (2014) 1–3.

[41] R.M. Crooks, M. Zhao, L. Sun, V. Chechik, L.K. Yeung, Dendrimer-encapsulated metal nanoparticles: Synthesis, characterization, and applications to catalysis, Acc. Chem. Res. 34 (2001) 181–190. https://doi.org/10.1021/ar000110a.

[42] Y.C. Lu, Z. Xu, H.A. Gasteiger, S. Chen, K. Hamad-Schifferli, Y. Shao-Horn, Platinum-gold nanoparticles: A highly active bifunctional electrocatalyst for rechargeable lithium-air batteries, J. Am. Chem. Soc. 132 (2010) 12170–12171. https://doi.org/10.1021/ja1036572.

[43] Z. Wang, J. Ruan, D. Cui, Advances and prospect of nanotechnology in stem cells, Nanoscale Res. Lett. 4 (2009) 593–605. https://doi.org/10.1007/s11671-009-9292-z.

[44] K. Ganesh, D. Archana, Review Article on Nanoparticles : An Overview, Am. J. Adv. Drug Deliv. 3 (2015) 196–215. www.ojadd.com.

[45] M. Laad, V.K.S. Jatti, Titanium oxide nanoparticles as additives in engine oil, J. King Saud Univ. - Eng. Sci. 30 (2018) 116–122. https://doi.org/10.1016/j.jksues.2016.01.008.

[46] W.T. Liu, Nanoparticles and their biological and environmental applications, J. Biosci. Bioeng. 102 (2006) 1–7. https://doi.org/10.1263/jbb.102.1.

[47] F.A. Blyakhman, A.P. Safronov, E.B. Makarova, F.A. Fadeyev, T.F. Shklyar, P.A. Shabadrov, S.F. Armas, G. V. Kurlyandskaya, Magnetic properties of iron oxide nanoparticles do not essentially contribute to ferrogel biocompatibility, Nanomaterials. 11 (2021) 1041. https://doi.org/10.3390/nano11041041.

[48] A.S. Teja, P.Y. Koh, Synthesis, properties, and applications of magnetic iron oxide nanoparticles, Prog. Cryst. Growth Charact. Mater. 55 (2009) 22–45. https://doi.org/10.1016/j.pcrysgrow.2008.08.003.

[49] S. Tiquia-Arashiro, D. Rodrigues, Nanoparticles Synthesized by Microorganisms, in: S. Tiquia-Arashiro, D.F. Rodrigues (Eds.), Extrem. Appl. Nanotechnol., Springer International Publishing, Cham, 2016: pp. 1–51. https://doi.org/10.1007/978-3-319-45215-9_1.

[50] M.J. Jacinto, V.C. Silva, D.M.S. Valladão, R.S. Souto, Biosynthesis of magnetic iron oxide nanoparticles: a review, Biotechnol. Lett. 43 (2021) 1–12. https://doi.org/10.1007/s10529-020-03047-0.

[51] G. Liu, J. Gao, H. Ai, X. Chen, Applications and potential toxicity of magnetic iron oxide nanoparticles, Small. 9 (2013) 1533–1545. https://doi.org/10.1002/smll.201201531.

[52] M. Jeon, M. V Halbert, Z.R. Stephen, M. Zhang, Iron Oxide Nanoparticles as T1 Contrast Agents for Magnetic Resonance Imaging: Fundamentals, Challenges, Applications, and Prospectives, Adv. Mater. 33 (2021) 1906539. https://doi.org/https://doi.org/10.1002/adma.201906539.

MATERIALS AND METHODS

Chapter III: Materials and methods

In recent years, green chemistry has attracted arising attention due to its safety and sustainability. Its ability to reduce or eliminate the uses or the production of dangerous and harmful materials has made it a favorable alternative to traditional chemistry in many multidisciplinary scientific and industrial fields [1].

This chapter, represents the methods used for biosynthesis, characterization, and optimization of the biosynthesized iron oxide nanoparticles using *Moringa oleifera* leaves extract. The characterization techniques were performed to confirm the biosynthesis of nanoparticles and study their properties, meanwhile the optimization aims to obtain the optimal conditions for IONPs biosynthesis. Furthermore, this chapter describes the method used to investigate the antibacterial activity of the synthesized nanoparticles.

III.1 The green synthesis of nanoparticles via plants extracts

Rising concerns have been related to the uses and production of nanoscale materials due to the toxic methods used for their production. These concerns are faded by implementing sustainable green chemistry in nanomaterials production, which allowed the production of low-cost, non-toxic, and eco-friendly nanomaterials.

Usually, the modern green methods used for nanomaterials synthesis involve using natural sources, which are biodegradable and biocompatible materials; bacteria, fungi, and plant extracts are the three primary sources involved in the biosynthesis of metal nanoparticles. By comparing the prementioned biological sources, the plant-mediated metal nanoparticles have higher stability and greater production rate, which motivated researchers to explore the possible mechanisms involved in metal ions bio-reduction and metal nanoparticles formation by plants [2].

III.1.1 The mechanism of nanoparticles synthesis using plants extracts

The mechanism of metals bioreduction in plant extracts generally passes through three main phases; activation, growth, and termination Figure III. 1.

The first phase is the activation phase; during this phase, metal ions are reduced metal atoms, and then nucleation of metal atoms takes place. After the nucleation of metal atoms, the ultra-small neighboring nanoparticles immediately unite to form larger particles of higher

thermodynamic stability in what is known by the growth phase. Finally, the termination phase which determines the final form of the synthesized nanoparticles. [3,4]

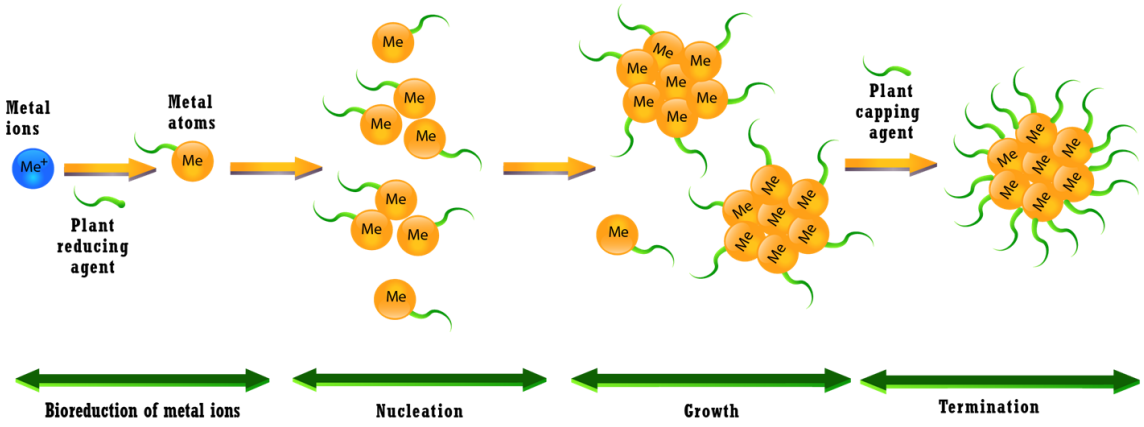

Figure III. 1 A schematic representation of metal nanoparticle synthesis in a plant extract.

III.1.2 The role of plant secondary metabolites in nanoparticles biosynthesis

Secondary plant metabolites are diverse chemical compounds produced by the plant cell through metabolic pathways derived from the primary metabolic pathways. These secondary metabolites play a vital role in the bioreduction of metal ions, which is essential for nanoparticle synthesis. Generally, polyphenols, terpenoids, alkaloids, phenolic acids, and proteins are the common plant metabolites that participate in the bioreduction of nanoparticles. Some of the main biomolecules capable of reducing metal ions are shown in Figure III. 2.

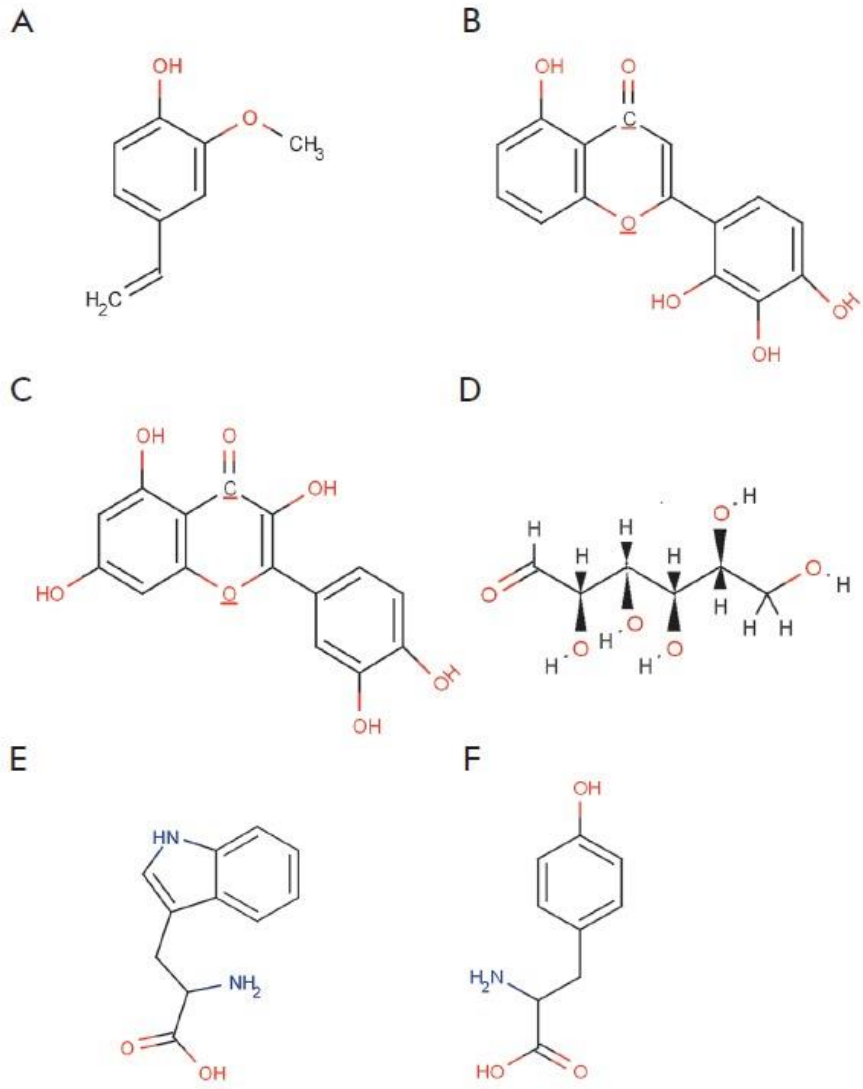

Figure III. 2 The main types of plant metabolites participated in the biosynthesis of metal nanoparticles: A – terpenoids (eugenol); B,C – flavonoids (luteolin, quertcetin); D – a reducing hexose with the open chain form; E,F – amino acids (tryptophan (E) and tyrosine[4].

III.2 Materials and Methods

The work was realized at the Laboratory of Valorisation and Technology of Sahara Resources (VTRS) at Echahid Hamma Lakhdar University, El Oued, Algeria. This study covers optimizing the biosynthesis temperature of iron oxide nanoparticles synthesized by *Moringa Oleifera* extract and their biological activity.

III.2.1 Collection and preparation of plant extract

Sample collection

Moringa Oleifera leaves were gathered from a local farm in Bagouza, Taghzout, 20 kilometers from the provincial capital, El Oued. The leaves were collected on the 12th of October 2019. Additional information about the collection of *Moringa Oleifera* are shown in Table III. 1, Figure III. 3 and Figure III. 4.

Figure III. 3 A photo of *Moringa Oleifera* tree from the collection location.

Table III. 1 Information about the collection of *Moringa Oleifera*.

Location	Site Name	Geographical coordinates	Altitude (m)	Bioclimatic zone	Collection date
El-Oued, Algeria	Bagouza	Latitude : 33°,49 N Longitude : 06°,72 E	68	Aride	12/10/2019

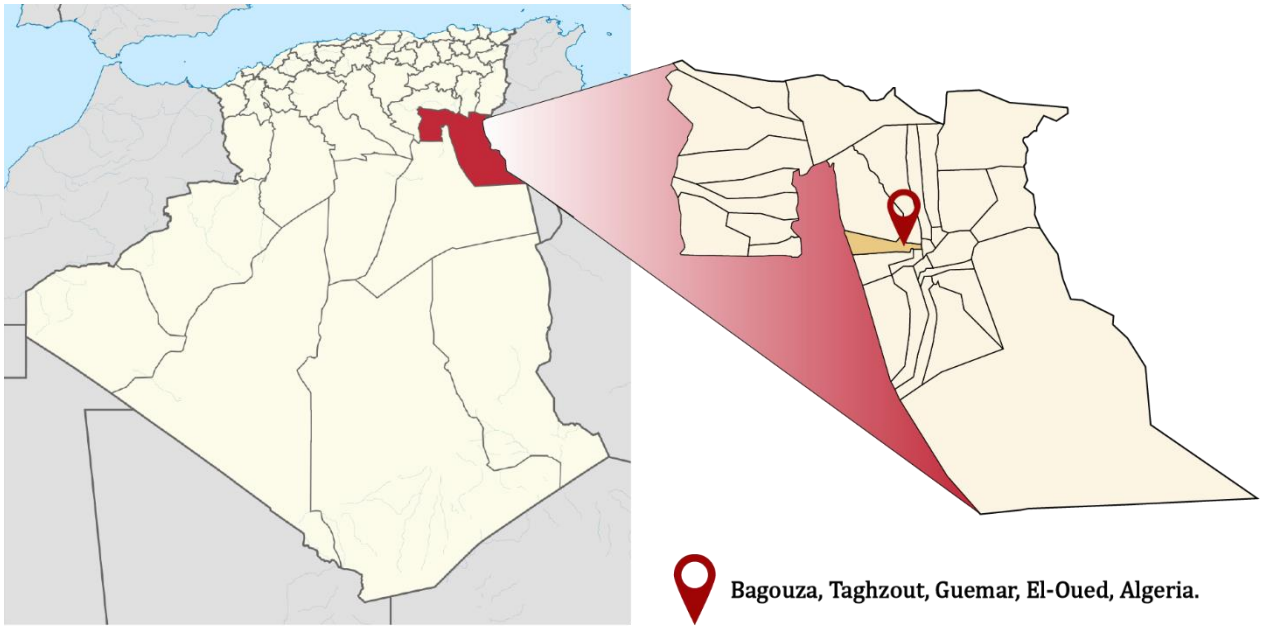

Figure III. 4 Geographic map showing the collection area.

The preparation of plant extract

First the green leaves were washed deeply with Deionized water and then left to dry away from sunlight for two weeks at room temperature. The leaves mixed continuously enabling the air to pass through the leaves. After that, electronic grinder was used to crush the air-dried leaves and then using the obtained fine powder to prepare the plant extract utilizing the maceration method [5]; 10 g of plant powder was added to 100 mL of deionized water and mixed steadily over night at room temperature. Finally, the liquid phase was separated with Whatman No.42 filter paper and stored at 4 °C for further use.

III.2.2 The biosynthesis of IONPs

IONPs biosynthesis was performed with minor modifications to a standard method used by prior studies for the biosynthesis of metal oxide NPs [6,7]. First, 10 mL of *Moringa Oleifera* leaves extract was poured into 100 mL of different concentrations of iron chloride solutions (0.02 to 0.07 M). This combination left to react under various temperatures (from 55°C to 95°C) for one hour and magnetic stirring rate of 350 rpm. A sample from each resulted solution was conserved for UV-Vis analysis. Next, the resulting mixture was centrifuged for 15 min with a rate of 3000 rpm, and the precipitated solid was washed with deionized water several times and dried in air-oven at 50°C overnight. Finally, the dried solid of the different samples was annealed for 3 hours at different temperatures (430 to 768°C) in order to purify the synthesized nanoparticles by removing the impurities and to ensure their full crystallization [7,8].

III.2.3 Characterization techniques

III.2.3.1 Structural and morphological properties

III.2.3.1.1 X Ray Diffractions (XRD)

The X ray diffractions technique was first used to determine the crystal structures of materials, determine lattice parameters, phase identification, and estimate the average crystallites size. Exposing matter to X-rays excites a variation of the electron cloud with respect to the nuclei in the atoms; these oscillations cause a re-emission of electromagnetic waves of the same frequency. This phenomenon is called Thomson coherent scattering. The wavelength of X-rays is of range between 0.01 and 10 (Å).

This technique is based on exposing a sample to be analyzed to a monochromatic beam of high-intensity x-rays. When an X-ray beam passes through a substance, the electrons of its atoms emit electromagnetic radiation in all directions of the same wavelength. These scattered waves from the electrons are arranged in the form of a crystal lattice. The interference of these waves causes diffraction by the crystal plane. Therefore, each crystalline substance scatters the X-ray as a diffraction pattern according to its atomic and molecular structure. The obtained diffraction pattern is recorded on an X-ray film or an electronic detector and then analyzed to determine the structural and morphological properties. The ray's interference is alternately either constructive or destructive.

The directions in which the interferences are constructive called diffraction peaks, which are determined by Bragg's law Equation (01) Figure III. 5.

$$n\lambda = 2d_{hkl} \sin\theta \quad (1)$$

Where λ is the x-ray wavelength, d_{hkl} is the interplanar spacing, θ is the incident angle (the angle between incident ray and the scatter plane), and n is an integer represents reflection order.

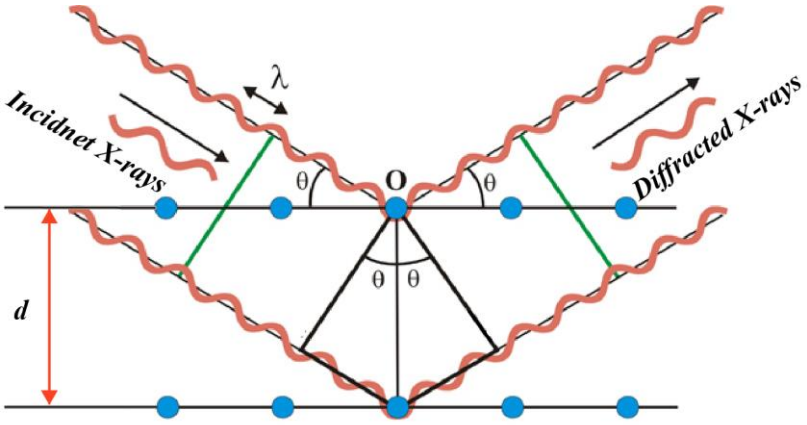

Figure III. 5 Schematic representation of Bragg's law conditions.

A variety of valuable information can be extracted from x-ray patterns, such as structural properties, the orientation of monocrystals, and crystallite size and shape.

Despite the presence of many techniques that estimates crystallite size based on the XRD patterns, the Scherrer's equation (Equation 02) is the one of the most common and efficient method for calculating the crystallite size.

$$D = \frac{k\,\lambda}{\beta\cos\theta} \quad (02)$$

Where D represents the crystallite size, k denotes the shape factor, β is FWHM (the full width at half maximum), λ is the wavelength (1.5418 Å, Cu$K\alpha$) and θ is the so-called diffraction angle [9].

III.2.3.1.2 Scanning Electron Microscopy (SEM)

Scanning Electron Microscopy (SEM) is an advanced high-resolution electron microscopy technique that allows monitoring the size, size distribution, and morphology of the micro and nanosized materials. This technique, therefore, offers a detailed morphological and dimensional analysis.

A scanning electron microscope contains a high-energy electron source called an electron gun that produces a beam of electrons.

The generated electron beam passes through a series of condenser lenses and apertures positioned below the electron gun to reduce the beam diameter to 1-10 nm. The prementioned focused beam falls directly at the sample causing electrons and X-rays emissions from the specimen. These emitted X-rays, backscattered electrons (BSE), and secondary electrons (SE) are collected by different detectors and then converted to characteristic signals that are sent to a display screen to show the final image [10].

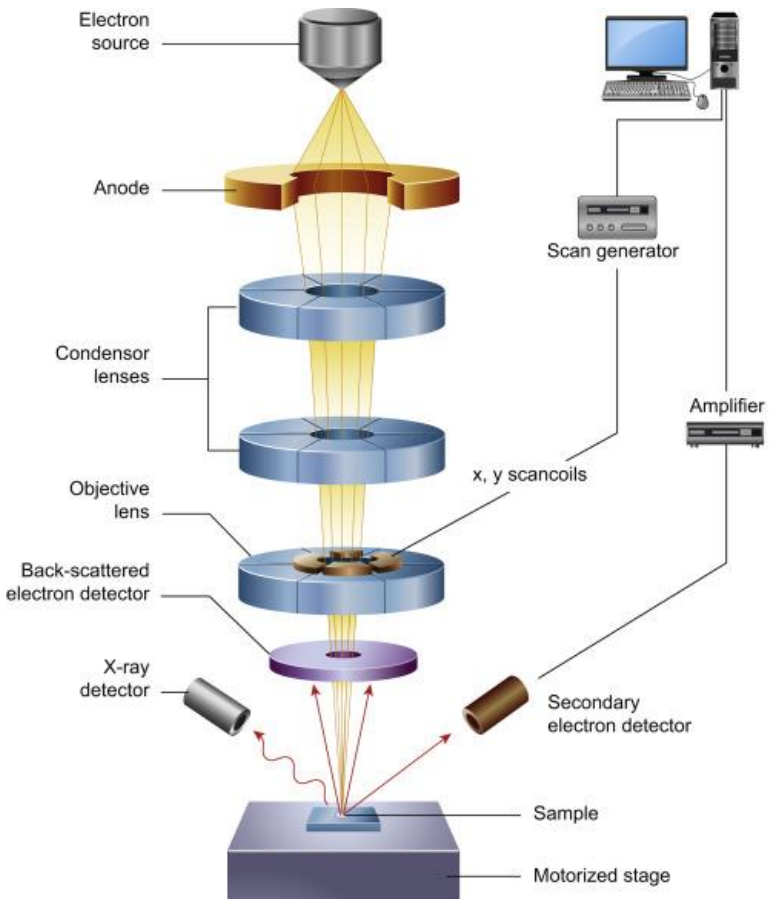

Figure III. 6 Schematic Diagram of Scanning Electron Microscope [11].

III.2.3.2 Optical properties

III.2.3.2.1 UV-visible absorption spectroscopy

UV-visible absorption spectroscopy plays a significant role in studying the optical properties of nanoparticles. This technique studies the interaction of electromagnetic waves and matter.

UV-visible analysis corresponds to the excitation of outer electrons, which pass from a ground state to an excited state after absorption of a photon in the UV-visible.

When the electrons encounter a light wave of a frequency corresponding to their vibratory frequencies, the latter absorbs the light wave's energy and acquires a vibratory movement. The vibrating electron interacts with neighboring electrons and converts the vibration into thermal energy. Absorption spectroscopy, therefore, refers to the measurement of the light absorbed by a material as a function of wavelength [12].

This spectrophotometer operates according to Beer-Lambert's principle, which indicates that the fraction of incident radiation absorbed is proportional to the number of absorbing molecules in its path (Equation 03) [13].

$$A = \log_{10}\left(\frac{I_0}{I}\right) = \epsilon c l \quad (03)$$

Where c is the molar concentration of the detected substance, A the absorbance value returned by the spectrophotometer, ϵ the wavelength-dependent molar extinction coefficient (also called molar absorptivity) in molar/cm, and l the pathlength in cm. I_0 and I represent the intensities of the incident and transmitted light respectively.

III.2.3.3 Chemical properties

III.2.3.3.1 Fourier Transform Infrared (FTIR) spectroscopy

FTIR spectroscopy is a technique that provides information about different functional groups from the peak positions in the spectrum. This analysis technique reveals the chemical groups that participated in the reduction and stabilization of nanoparticles.

FTIR analysis is performed by exposing the sample to a single or double infrared radiation beam. The absorbed radiations detect characteristic vibration frequencies of chemical bonds and the chemical functional groups present in the material.

the emitted beam is close to the molecule vibrational energy, the latter absorbs the radiation and causes a decrease in the reflected or transmitted intensity. As a result, IR radiation energy is reduced after the interaction, leading to the appearance of an absorption band at this frequency. This absorption is not systematic; it depends on the molecule's geometry and its symmetry. The position of these absorption bands will depend in particular on the difference in electronegativity between atoms and their mass [14,15].

III.2.4 Optimization method

III.2.4.1 Design of experiments (DOE)

Design of experiments (DOE) is a structured and planned method used to study the relationship between different factors (variables) affecting different outputs (responses). The combined effect of these factors is studied by testing several factors at different levels combined in a single experiment [16].

The classical investigation of One Factor At a Time (OFAT) is performed by modifying a single factor while keeping other factors constant, which explains only the effect of individual factors. This technique does not precisely describe the combined effect of different factors. Moreover, it requires a considerable number of experiments that could be expensive and a waste of time, resources, and efforts. These disadvantages can be efficiently reduced by understanding the interactive effects caused by the change of different factors. For this reason, Design of experiments (DOE) is employed to analyze complex problems with many influencing factors at the same time. Instead of testing each factor individually, in a design of experiments, several factors are modified at a time to reduce the amount of testing with the possibility of analyzing interactions between factors [17]. This is done using test tables. These arrays are full factor arrays (all combinations are tested) or fraction arrays (part of a full factorial test setup to reduce the number of tests) [18].

The main steps for creating the design used in this study is based on the experimental plan shown in Figure III. 7

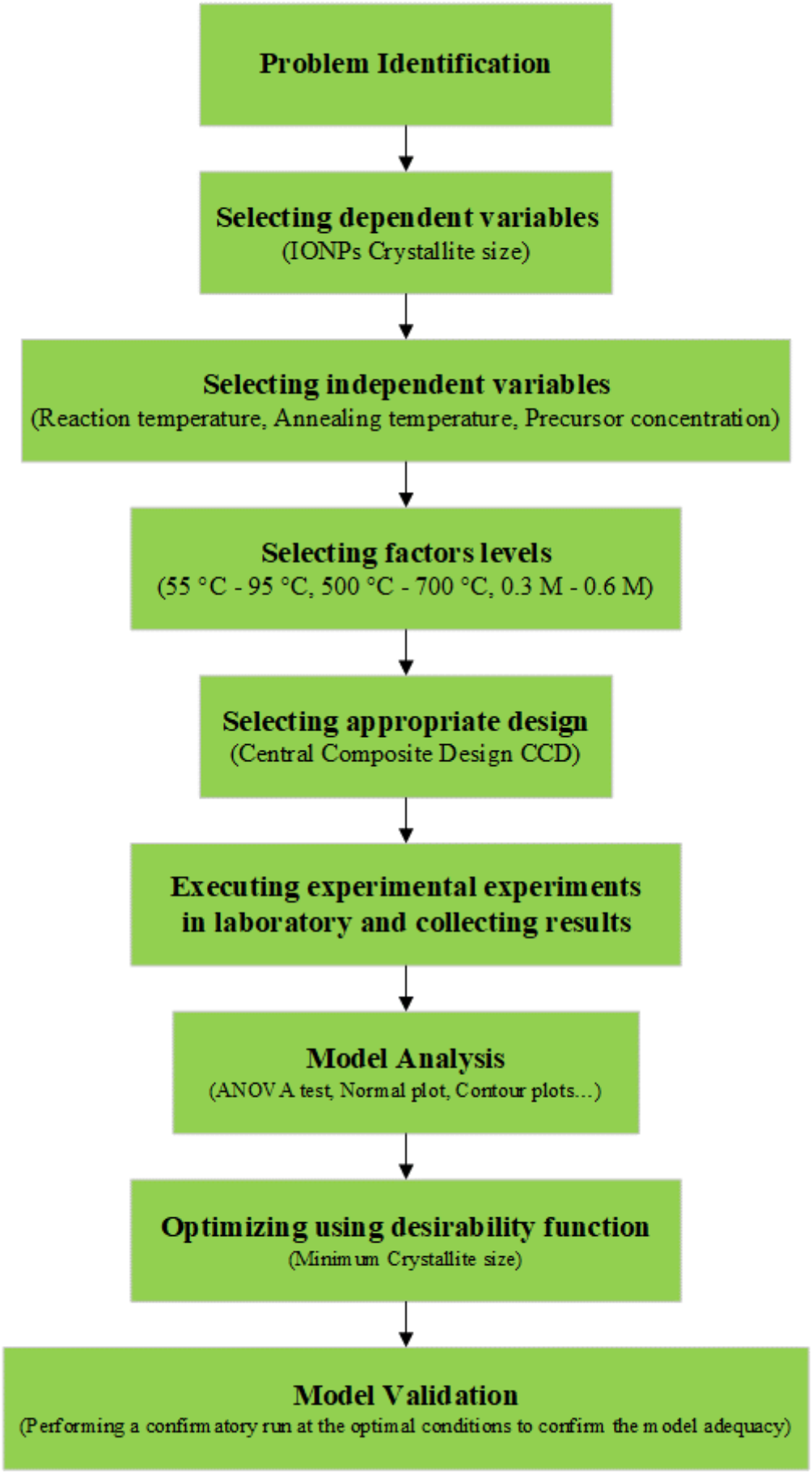

Figure III. 7 General flow chart of the experimental procedure.

III.2.4.2 Response Surface Methodology (RSM)

RSM is an effective statistical and mathematical method that proficiently model and study processes containing two factors or more by studying the effect these factors (inputs) and their interactions on one or different responses (outputs). This method aims to achieve the optimal conditions for a combination of independent variables that optimizes the response and obtains the desired result with fewer number of runs [19].

III.2.4.3 Box-Wilson Central Composite Design (CCD)

Box-Wilson Central Composite Design, frequently known as Central Composite Design CCD is a two-level factorial design, improved with center and star points that enables fitting the quadratic polynomial models [20]. In this design the independent variables (inputs) are wide-ranging over 05 levels: the high level (1), lower level (-1), center points (0), added to 02 outer (star) points symbolized (α and $-\alpha$). that signify the extreme levels for each factor (maximum and minimum). For a rotatable design having m factors, $\alpha = 2^{m/4}$. In design used for this study m = 3 so $\alpha = 2^{3/4} = 1.682$.

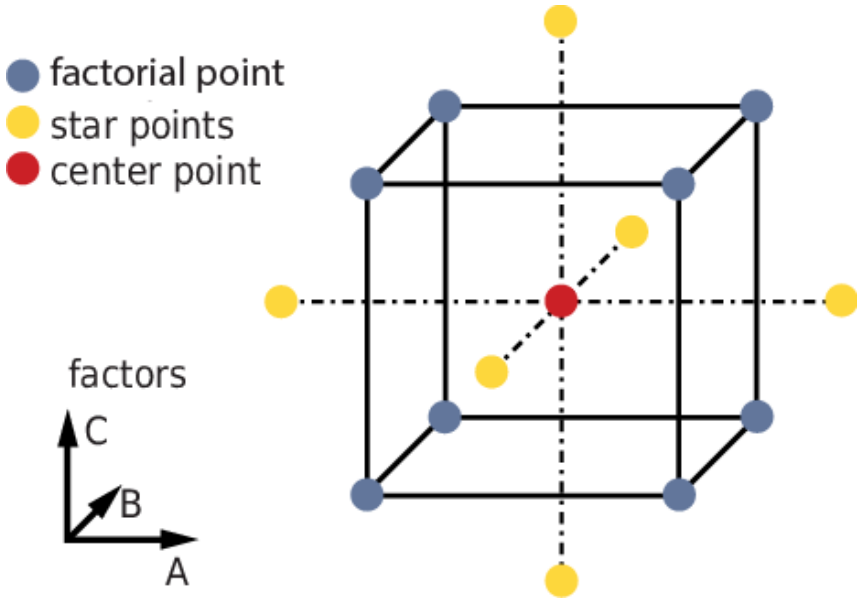

Figure III. 8 Schematic illustration of central composite design

III.2.4.4 The proposed mathematical model

The mathematical model proposed by central composite design for three factors is a quadratic equation that can be employed for predicting the optimal desired response expressed as follows (04)

$$Y = \beta_0 + \sum_{j=1}^{m} \beta_j x_j + \sum_{j=1}^{m} \beta_{jj} x^2{}_j + \sum \sum_{i<j=2}^{m} \beta_{ij} x_i x_j + \varepsilon \quad (04)$$

where β_0 is a constant coefficient, x_i and x_j are factors (i and j varies from 1 to m). The coefficients β_i, β_{ii}, and β_{ij} represent the linear, binominal and combined effects, respectively. m signify the sum of studied factors and ε represents the error [21,22].

III.2.4.5 Optimizing the biosynthesis temperature of IONPs

III.2.4.5.1 Variable's selection

In order to optimize the biosynthesis temperature and IONPs biosynthesis. The main parameters involved in IONPs biosynthesis were studied besides the biosynthesis temperature, since its strongly dependent to these parameters such as precursor concentration. IONPs size found to changes significantly by annealing temperature. Consequently, these three variables were selected for this study.

The choice of suitable ranges for the studied factors was inspired from the previous studies. It was reported that the annealing temperature of 500 °C synthesizes a clean IONPs [5–7]. Therefor 500°C was selected as the low level (-1) for this factor. Moreover, According to former studies, the recommended reaction temperature for the biosynthesis of the metallic oxide nanoparticles using plant extracts is in the range of 25–100°C [23]. Consequently, 95°C was set as the high level (1) this reaction temperature parameter. The precursor concentrations ranged from 0.03 to 0.07 in order to be suitable for the volume of the plant extract used in this biosynthesis process [8,24]. Table III. 2 shows the coded and actual levels of each independent variable.

Table III. 2 The levels of the different factors.

Independent variable	Codes	Levels				
		-α	-1	0	+1	+α
Precursor concentration (M)	A	0.0 197	0.03	0.045	0.06	0.0702
Reaction Temperature (°C)	B	41.3641	55	75	95	108.636
Annealing Temperature (°C)	C	431.821	500	600	700	768.179

The sum of the required experimental runs is calculated by the following equation (05);

$$N = 2^n + 2n + n_c \quad (05)$$

where N is the total number of experimental runs and n is the number of variables, the values 2^n, $2n$ and n_c represent factorial runs, axial and center runs respectively. For three variables, the advised number of replicates at the center point is six [25]. Therefore, a total number of twenty runs is performed according to Equation (05). They are listed with their coded values in Table III. 3. The runs were operated in a randomized arrangement to avoid systematic bias.

Table III. 3 The experimental design for each combination of factors along with their predicted and experimental response.

Run	Coded values			Crystallite size (nm)	
	A	B	C	Experimental	Predicted
1	0	0	0	62.28	61.76
2	0	0	0	61.42	61.76
3	0	0	-1.682	40.71	40.18
4	0	0	1.682	64.03	63.74
5	-1	-1	-1	29.26	29.34
6	0	0	0	61.54	61.76
7	0	0	0	61.86	61.76
8	1.682	0	0	63.31	63.23
9	-1.682	0	0	34.85	34.12
10	0	1.682	0	54.06	52.85
11	1	-1	1	60.30	60.01
12	0	0	0	60.97	61.76
13	1	1	1	64.55	65.04
14	1	1	-1	57.55	58.03
15	-1	1	-1	32.22	33.08
16	-1	1	1	48.82	49.48
17	-1	-1	1	50.26	50.35
18	1	-1	-1	48.47	48.39
19	0	0	0	62.37	61.76
20	0	-1.682	0	45.09	45.48

III.2.4.6 Data analysis

Design Expert (version 13) statistical software was employed to constructing the experimental design and analyzing the obtained data by generating the different statistical reports and plots, investigating the different effects of the chosen variables, and determining the optimal conditions within the studied range.

III.2.5 Antibacterial activity

The antibacterial activity of the biosynthesized IONPs was investigated using the disk diffusion method. Before the experiment, pure cultures of two human pathogens, E. coli and S. aureus, were isolated from patient's samples collected from El-medjed Laboratory, El-Oued, Algeria. The bacteria were then subcultured on nutrient agar (NA) and incubated at a temperature of 37 °C overnight.

Different runs of IONPs of different sizes were properly sonicated and dispersed in deionized water in concentrations of 50 mg/ml. The dispersed IONPs were loaded to 7mm disks made of No.1 Whatman filter paper.

Mueller-Hinton agar (MHA) was heated to 55°C, then 20 ml from the solution was poured in a petri dish and left to solidify for 15 min; the preprepared bacteria then was dispersed in saline solution (NaCl 0.9%) using a vortex mixer (2550 rpm) in microorganism concentration of 0.5 McFarland. After that, the bacterial uniformly dispersed at the MHA surface using cotton swap.

The different runs of IONPs of various sizes were properly sonicated and dispersed in deionized water in concentrations of 50 mg/ml. Then, the dispersed IONPs were loaded to 7 mm disks made of No.1 Whatman filter paper. Gentamycin (120 mg/mL) was used as a positive control, while deionized water was the negative control.

Finally, the prepared IONPs disks along with positive and negative controls were placed at the MHA surface at 37°C for 24 hrs. At the end of incubation, inhibition zones formed around the disc were measured with a transparent ruler in millimeters.

A comprehanisive graphical abstract that explains the main steps of this study is shown in Figure III. 9

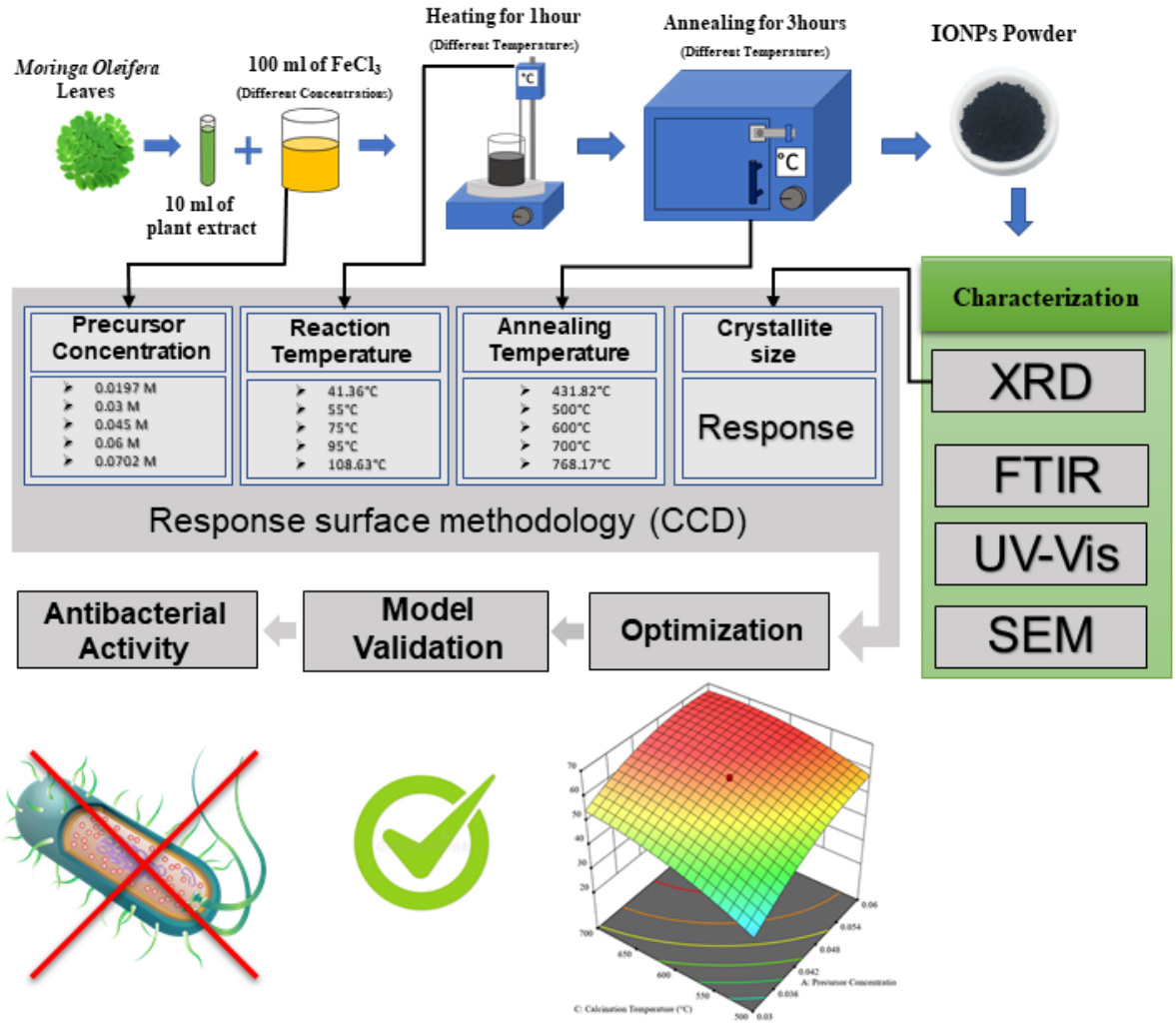

Figure III. 9 Comprehensive graphical abstract

References

[1] J.C. Warner, A.S. Cannon, K.M. Dye, Green chemistry, Environ. Impact Assess. Rev. 24 (2004) 775–799. https://doi.org/10.1016/j.eiar.2004.06.006.

[2] C.L. Keat, A. Aziz, A.M. Eid, N.A. Elmarzugi, Biosynthesis of nanoparticles and silver nanoparticles, Bioresour. Bioprocess. 2 (2015) 47. https://doi.org/10.1186/s40643-015-0076-2.

[3] V. V. Makarov, A.J. Love, O. V. Sinitsyna, S.S. Makarova, I. V. Yaminsky, M.E. Taliansky, N.O. Kalinina, "Green" nanotechnologies: Synthesis of metal nanoparticles using plants, Acta Naturae. 6 (2014) 35–44. https://doi.org/10.32607/20758251-2014-6-1-35-44.

[4] N.T.K. Thanh, N. Maclean, S. Mahiddine, Mechanisms of Nucleation and Growth of Nanoparticles in Solution, Chem. Rev. 114 (2014) 7610–7630. https://doi.org/10.1021/cr400544s.

[5] A. Bouafia, S.E. Laouini, Green synthesis of iron oxide nanoparticles by aqueous leaves extract of Mentha Pulegium L.: Effect of ferric chloride concentration on the type of product, Mater. Lett. 265 (2020) 127364–127368. https://doi.org/10.1016/j.matlet.2020.127364.

[6] F.T. Thema, P. Beukes, A. Gurib-Fakim, M. Maaza, Green synthesis of Monteponite CdO nanoparticles by Agathosma betulina natural extract, J. Alloys Compd. 646 (2015) 1043–1048. https://doi.org/10.1016/j.jallcom.2015.05.279.

[7] A.T. Khalil, M. Ovais, I. Ullah, M. Ali, Z.K. Shinwari, M. Maaza, Biosynthesis of iron oxide (Fe 2 O 3) nanoparticles via aqueous extracts of Sageretia thea (Osbeck.) and their pharmacognostic properties, Green Chem. Lett. Rev. 10 (2017) 186–201. https://doi.org/10.1080/17518253.2017.1339831.

[8] J.A.A. Abdullah, L. Salah Eddine, B. Abderrhmane, M. Alonso-González, A. Guerrero, A. Romero, Green synthesis and characterization of iron oxide nanoparticles by pheonix dactylifera leaf extract and evaluation of their antioxidant activity, Sustain. Chem. Pharm. 17 (2020) 100280–100287. https://doi.org/10.1016/j.scp.2020.100280.

[9] J.I. Langford, X-ray diffraction procedures for polycrystalline and amorphous materials by H. P. Klug and L. E. Alexander, J. Appl. Crystallogr. 8 (1975) 573–574. https://doi.org/10.1107/S0021889875011399.

[10] Q. Luo, Electron Microscopy and Spectroscopy in the Analysis of Friction and Wear Mechanisms, Lubricants. 6 (2018). https://doi.org/10.3390/lubricants6030058.

[11] B.J. Inkson, Scanning Electron Microscopy (SEM) and Transmission Electron Microscopy (TEM) for Materials Characterization, in: G. Hübschen, I. Altpeter, R. Tschuncky, H.-G.B.T.-M.C.U.N.E. (NDE) M. Herrmann (Eds.), Mater. Charact. Using Nondestruct. Eval. Methods, Woodhead Publishing, 2016: pp. 17–43. https://doi.org/10.1016/B978-0-08-100040-3.00002-X.

[12] G. George, R. Wilson, J. Joy, Ultraviolet Spectroscopy: A Facile Approach for the Characterization of Nanomaterials, in: S. Thomas, R. Thomas, A.K. Zachariah, R.K.B.T.-S.M. for N.C. Mishra (Eds.), Spectrosc. Methods Nanomater. Charact., Elsevier, 2017: pp. 55–72. https://doi.org/10.1016/B978-0-323-46140-5.00003-0.

[13] W. Mäntele, E. Deniz, UV–VIS absorption spectroscopy: Lambert-Beer reloaded, Spectrochim. Acta - Part A Mol. Biomol. Spectrosc. 173 (2017) 965–968. https://doi.org/10.1016/j.saa.2016.09.037.

[14] S. Groiss, R. Selvaraj, T. Varadavenkatesan, R. Vinayagam, Structural characterization, antibacterial and catalytic effect of iron oxide nanoparticles synthesised using the leaf extract of Cynometra ramiflora, J. Mol. Struct. 1128 (2017) 572–578. https://doi.org/10.1016/j.molstruc.2016.09.031.

[15] D. Kowalczuk, M. Pitucha, Application of FTIR method for the assessment of immobilization of active substances in the matrix of biomedical materials, Materials (Basel). 12 (2019). https://doi.org/10.3390/ma12182972.

[16] M. Khanahmadi, R. Ghaffarzadegan, F. Khalighi-Sigaroodi, H. Naghdi Badi, A. Mehrafarin, R. Hajiaghaee, Optimization of the glycyrrhizic acid extraction from licorice by response surface methodology, Iran. J. Chem. Chem. Eng. 37 (2018) 121–129.

[17] G. Milad, F. Hossein, Response surface methodology optimization of cobalt (II) and lead (II) removal from aqueous solution using MWCNT-Fe3o4 nanocomposite, Iran.

J. Chem. Chem. Eng. 36 (2017) 129–141.

[18] Y. Nuapia, E. Cukrowska, H. Tutu, L. Chimuka, Statistical comparison of two modeling methods on pressurized hot water extraction of vitamin C and phenolic compounds from Moringa oleifera leaves, South African J. Bot. 129 (2020) 9–16. https://doi.org/10.1016/j.sajb.2018.09.001.

[19] K. Hinkelmann, Design and Analysis of Experiments, 9 th, John wiley & sons, New York, 2012. https://doi.org/10.1002/9781118147634.

[20] H. Amiri, R. Nabizadeh, S. Silva Martinez, S. Jamaleddin Shahtaheri, K. Yaghmaeian, A. Badiei, S. Nazmara, K. Naddafi, Response surface methodology modeling to improve degradation of Chlorpyrifos in agriculture runoff using TiO2 solar photocatalytic in a raceway pond reactor, Ecotoxicol. Environ. Saf. 147 (2018) 919–925. https://doi.org/10.1016/j.ecoenv.2017.09.062.

[21] X. Zhang, J. Chen, M. Mao, H. Guo, Y. Dai, Extraction optimization of the polysaccharide from Adenophorae Radix by central composite design, Int. J. Biol. Macromol. 67 (2014) 318–322. https://doi.org/https://doi.org/10.1016/j.ijbiomac.2014.03.039.

[22] P. Mondal, M.K. Purkait, Green synthesized iron nanoparticles supported on pH responsive polymeric membrane for nitrobenzene reduction and fluoride rejection study: Optimization approach, J. Clean. Prod. 170 (2018) 1111–1123. https://doi.org/10.1016/j.jclepro.2017.09.222.

[23] J.K. Patra, K.-H. Baek, Green Nanobiotechnology: Factors Affecting Synthesis and Characterization Techniques, J. Nanomater. 2014 (2014) 1–12. https://doi.org/10.1155/2014/417305.

[24] H. Sharifi Dehsari, A. Halda Ribeiro, B. Ersöz, W. Tremel, G. Jakob, K. Asadi, Effect of precursor concentration on size evolution of iron oxide nanoparticles, CrystEngComm. 19 (2017) 6694–6702. https://doi.org/10.1039/c7ce01406f.

[25] G.E.P. Box, J.S. Hunter, Multi-Factor Experimental Designs for Exploring Response Surfaces, Ann. Math. Stat. 28 (1957) 195–241. https://doi.org/10.1214/aoms/1177707047.

RESULTS AND DISCUSION

Chapter IV: Results and discussion

The past two decades have witnessed an extensive research effort spent on optimizing the synthesis of metal oxide nanoparticles due to their unique properties has made revolutionary improvements in many fields [1]. This chapter, represents the different results of the optimization, characterizations, and antibacterial activity for IONPs, followed by discussions and interpretations.

IV.1 Visual observations

The formation IONPs was clearly distinguished by the immediate color change from light brown to dark black (Figure IV. 1) when the ferric chloride ($FeCl_3$) solution was mixed with *Moringa Oleifera* leaves extract which was clearly noted by naked eye observation. This result match those observed in earlier studies using diverse plants [2,3]. The color change occurred due to the presence of the active molecules in the used extract, which reduced the iron metal ions.

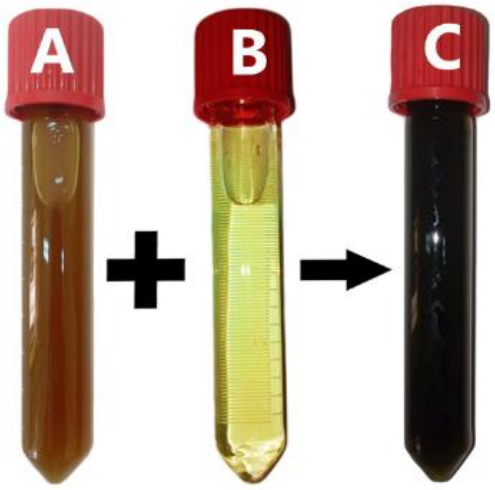

Figure IV. 1 Visual color change; (A) $FeCl_3$ solution, (B) *Moringa Oleifera* extract, and (C) IONPs solution.

Moringa oleifera is a rich source of biomolecules such as (polyphenols, flavonoids, terpenoids, alkaloids, tannins, etc.) that can reduce and stabilize metal ions to their nano form. When ferric chloride salt ($FeCl_3$) dissolves in water, it forms an ionic solution of iron and chlorine ions that moves freely moves in the solution. Once the ionic solution is mixed with *Moringa oleifera* liquid extract, the freely moving iron ions are attracted towards the plant's biomolecules due to electron deficiency. This leads to transferring electrons from

oxygen to iron ions according to the donor-acceptor mechanism causing the reduction of iron ions to zero-valent NPs. This latter is then stabilized by the other biomolecules of the plant extract. On the other side, the plant biomolecules are converted to keto compounds. The reduced iron nanoparticles are transformed into iron oxide nanoparticles during air-drying and annealing [1].

IV.2 Characterization of IONPs

IV.2.1 UV–visible Spectroscopy

The UV-visible spectrum of IONPs was recorded using a double-beam UV-Visible spectrophotometer (Shimadzu 1800) recording the range of 200-900 nm. Before the analysis, IONPs solution concentration was reduced by pouring 1 mL of IONPs solution in 10 mL of deionized water. Quartz cuvette was used in this analysis, and distilled water was used as the reference solvent.

The graphs corresponding to IONPS and *Moringa* leaves extract are shown in Figure IV. 2. Two peaks located around 250 and 320 nm appeared in the plant extract spectrum. Meanwhile, IONPs spectrum exhibited a single peak at 275 nm. This peak is attributed to the characteristic IONPs SPR Surface Plasmon Resonance absorption band of IONPs [3–5].

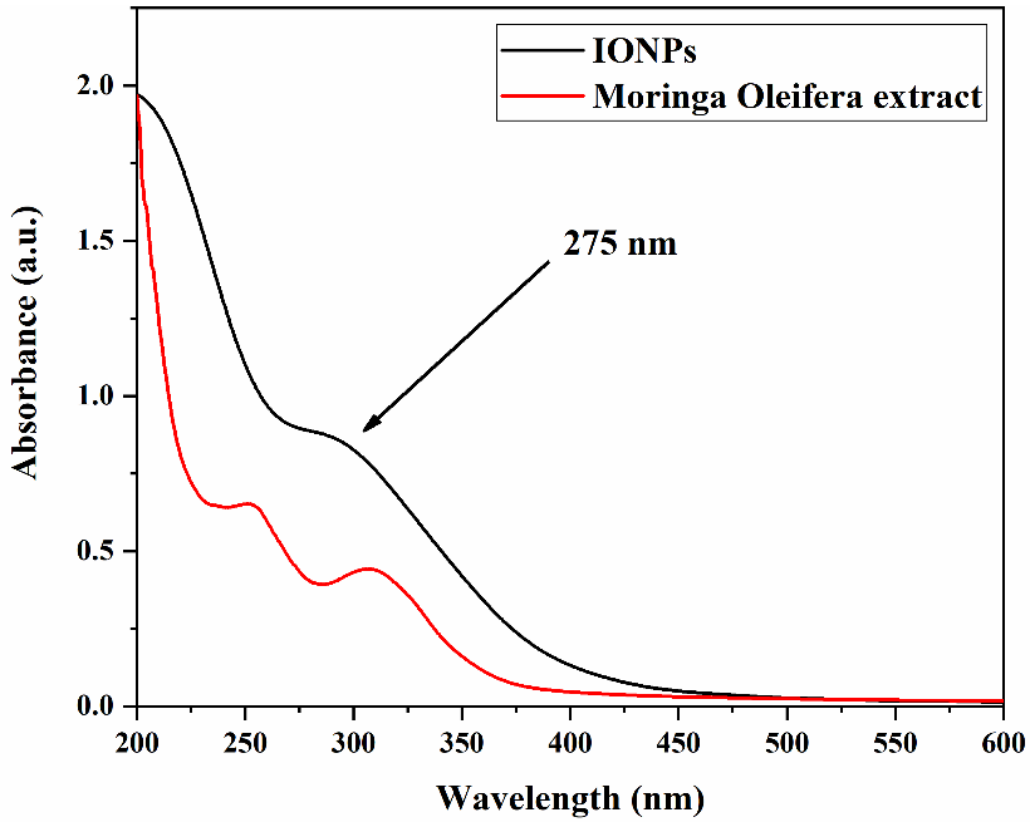

Figure IV. 2 UV-vis absorbance spectra of IONPs and the plant extract.

The gap energy E_g of the synthesized IONPs was determined from the UV-Visible spectrum. Figure IV. 3 and Figure IV. 4 shows the variation of (αhv) as a function of (hv) the gap energy (E_g) of nanoparticles is estimated using Tauc's formula (Equation (06)) [6]:

$$(\alpha hv) = K(hv - E_g)^n \quad (06)$$

- K: is a constant and hv represents the energy of the incident photon.
- α: the absorption coefficient.
- E_g: the optical band gap in electron volts (eV).
- n: is an variable exponent that depends on the nature of the electronic transition (when the transition is direct $n = 2$, and when transition is indirect $n = 1/2$) [7,8].

Prior studies evaluating hematite (α-Fe_2O_3) band gap observed inconsistent results on whether it has direct or indirect bandgap; some has reported that hematite is a direct bandgap material [3,9], while others described it as an indirect bandgap material [10,11]. Differently, other demonstrated that α-Fe_2O_3 possess the both types of band gaps direct and indirect [12,13]. Consequently, we have considered studying the both direct and indirect band gap transmissions. The estimation of bandgap using Tauc's plot exhibited values of 3.53 eV for direct transmissions and 2.83 eV for indirect transmissions. These results are in line with those of previous studies [3,7].

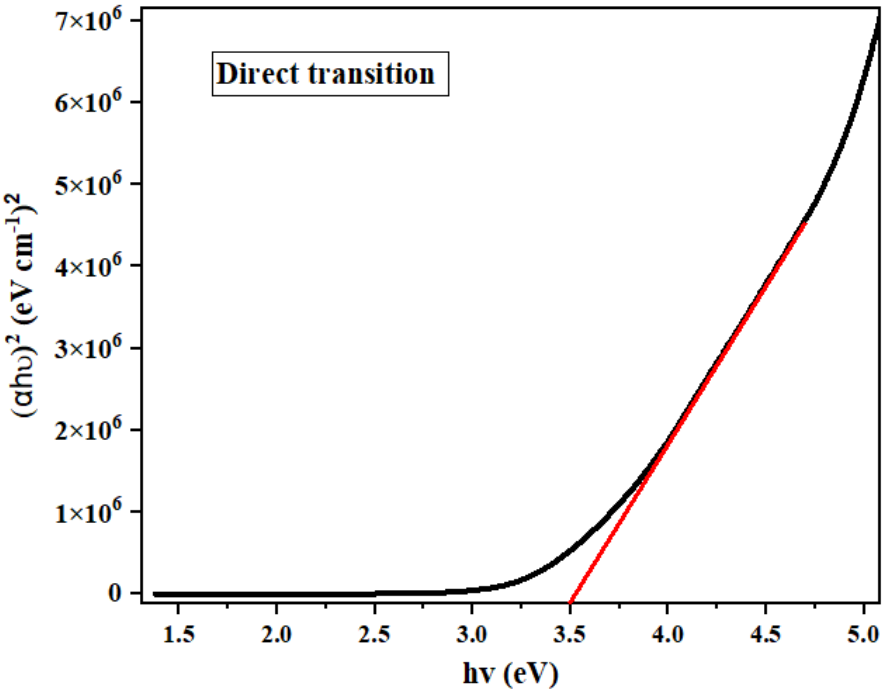

Figure IV. 3 Direct bandgap (Eg) estimation using Tauc's plot.

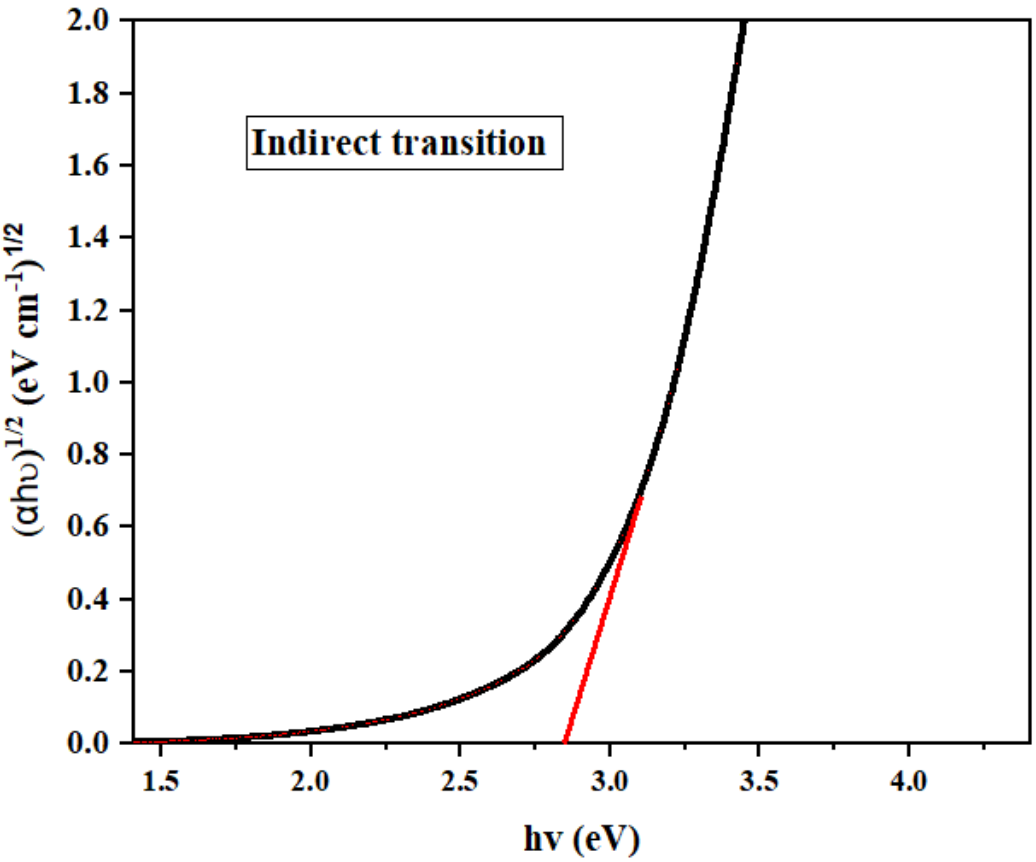

Figure IV. 4 Indirect bandgap (Eg) estimation using Tauc's plot.

IV.2.2 Fourier Transform Infrared (FTIR) spectroscopy

IONPs and *Moringa Oleifera* leaves extract FTIR spectra were recorded on Total Reflection (ATR) spectrometer (Thermo scientific-Nicolet iS5) operating in the range of 400-4000 cm^{-1}.

FTIR analysis was mainly employed to identify the biomolecules that participated in iron oxide nanoparticles reduction and stabilization by comparing the spectrum of the crude plant extract with the spectrum of the biosynthesized nanoparticles.

The resultant FTIR spectrum (Figure IV. 5.a) has revealed on multiple absorption peaks that related to the different functional groups of the biomolecules presented in the *Moringa Oleifera* extract.

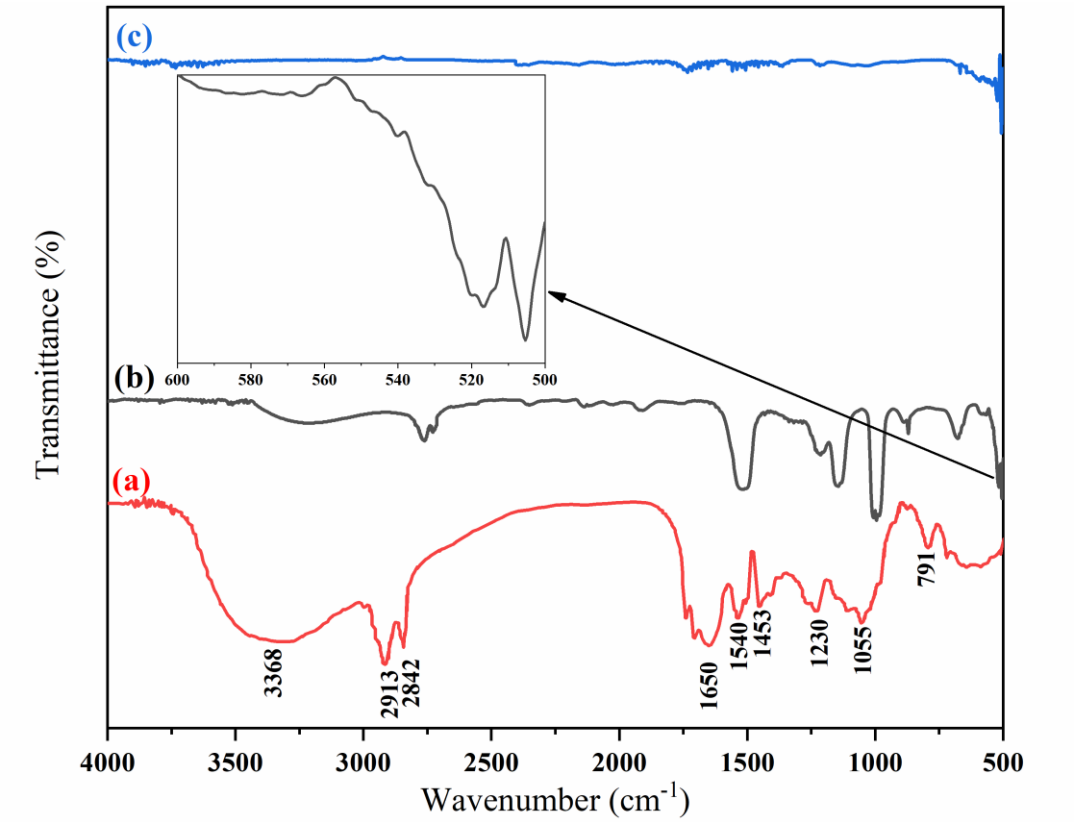

Figure IV. 5 FTIR Spectra of: (a) *Moringa Oleifera* extract, (b) IONPs before annealing, and (c) IONPs after annealing.

The O–H stretching vibrations was observed at the broad peak centered at 3368 cm^{-1}[14], the two close peaks appeared at 2913 cm^{-1} and 2842 cm^{-1} are assigned to the methyl group C–H asymmetric and symmetric stretching vibrations respectively [15], the C=O and C=C stretching vibrations are distinguished by the peaks located 1650 cm^{-1} and 1453 cm^{-1} respectively [16]. The presence of amines group was noted by the C–N stretching vibration band appears as narrow peak around 1540 cm^{-1} [16]. In addition, the peaks centered at 1230 cm^{-1} and 1055 cm^{-1} are assigned to C–O stretching C–OH bending vibrations respectively [17]. The peaks appeared in *Moringa Oleifera* extract spectrum confirms that it contains different polyphenolic compounds [15], that can effectively reduce and stabilize metals for nanoparticles biosynthesis [18].

Comparing the FTIR spectra of plant extract (Figure IV. 5.a) and IONPs (Figure IV. 5.b) show that there is a shift in the wavenumber of the absorption bands, which indicate the interaction of biomolecules with iron ions [19]. Furthermore, the comparison exposed a distinguished decrease in intensity of the band centered at 3368 cm^{-1}, which indicates the vital role of the biomolecules attributed to this functional group in the reduction and stabilization of IONPs [5]. The wavenumber range from 500 to 600 cm^{-1} has been zoomed

to display the inorganic peaks, the peaks shown at 506 cm^{-1} and 515 cm^{-1} are attributed to the Fe–O stretching vibrations [20], [21]. The same peaks were also seen in the spectrum of IONPs annealed (Figure IV. 5.c), and all the executed runs Figure IV. 6.

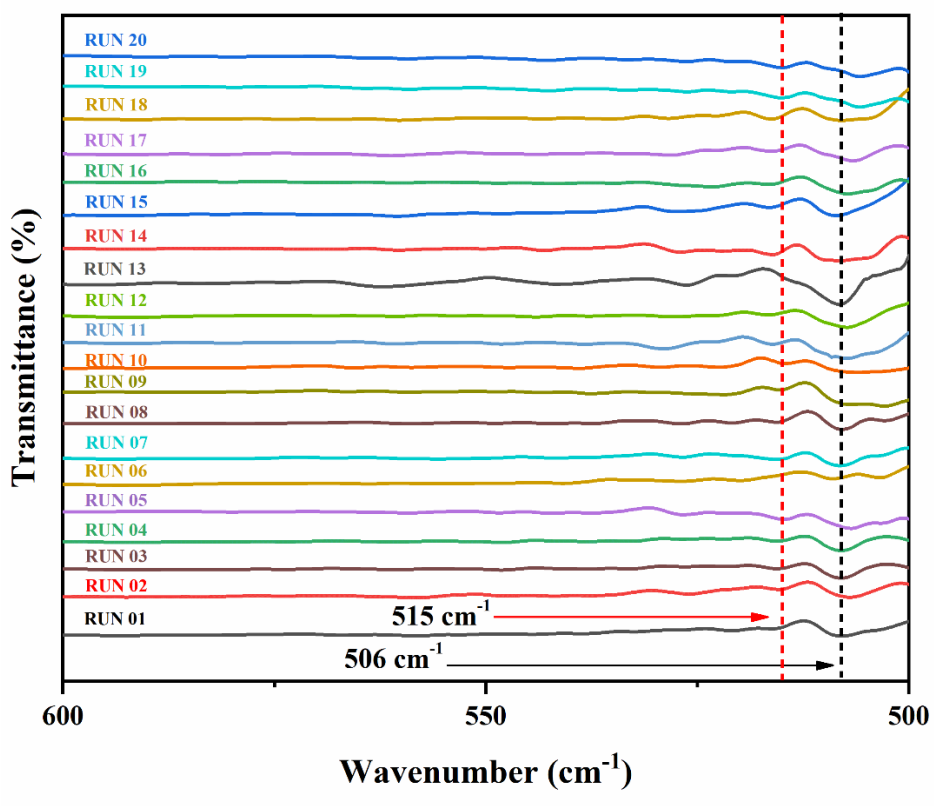

Figure IV. 6 FTIR spectra zoomed in the range from 600 to 500 cm^{-1} for all the annealed IONPs runs.

IV.2.3 X-ray diffraction (XRD)

The X Ray Diffraction was performed to study the crystalline structure, crystallite size and the phases presented IONPs samples. The XRD patterns were recorded using X ray diffractometer (Rigaku, Mini Flex 600) operating in 2θ range from 20° to 80° with $K\alpha$ radiation of copper (λ= 1.5406Å). The X ray was produced with 30 kilovolts and 20 mA.

Figure IV. 7 shows all the XRD patterns of the different runs executed according to the experimental design order Table III. 3. Common peaks were observed in all the XRD patterns of the different runs placed at 2-theta (2θ) positions of 24.15°, 33.13°, 35.64°, 40.65°, 49.48°, 54.09°, 57.43°, 62.53°, and 64.14° assigned respectively to the crystal planes of (012), (104), (110), (113), (024), (116), (122), (214) and (300) [22]. According to JCPDS card no. 01-079-0007 these peaks are allocated to iron oxide of the type Hematite α-Fe_2O_3

of having its characteristic rhombohedral geometry and lattice parameters a = b = 5.04 Å, and c = 13.75 Å (space group: R-3c) [23].

As can be seen from Figure IV. 7 the peaks of XRD patterns vary in terms of intensity and width due to the different biosynthesis conditions. According to Scherrer's formula (Equation 02), these variations in peaks intensity and width indorse that these patterns correspond to samples of different crystallite sizes since the crystallite size is estimated from FWHM and peaks positions. The IONPs of the executed runs were of diverse sizes at the nanoscale range of 29.26 - 64.55 nm.

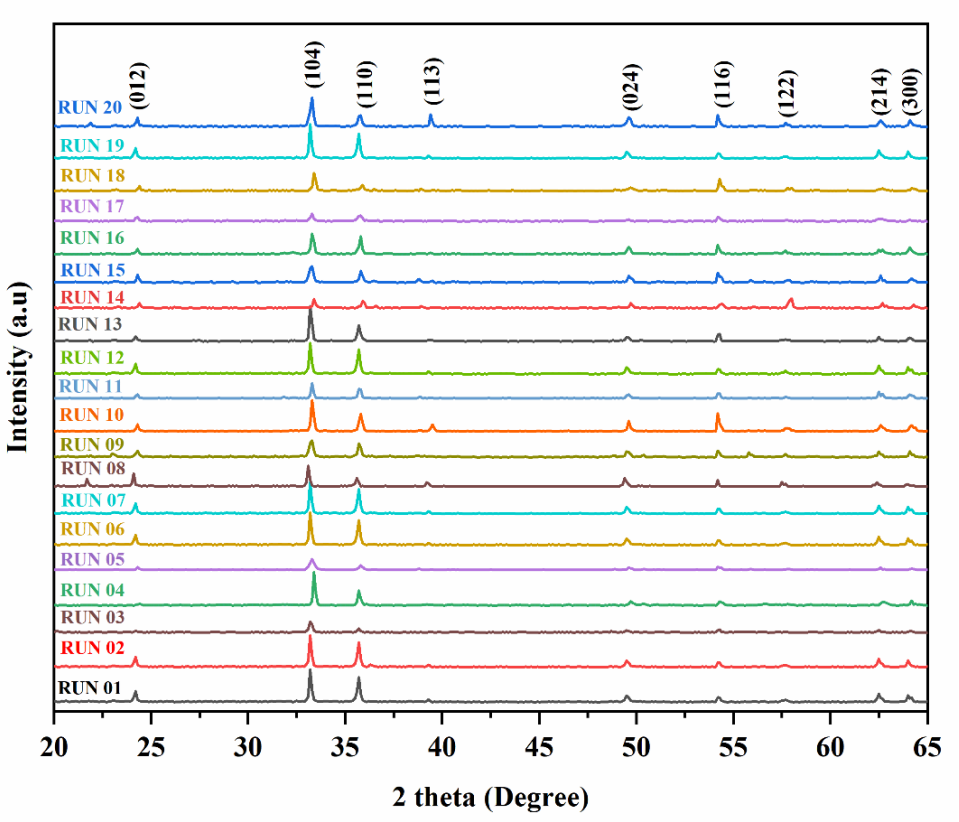

Figure IV. 7 X ray diffraction patterns of all the performed experiments.

IV.3 Optimizing the biosynthesis temperature of IONPs

IV.3.1 Fitting of model

The Data obtained from Central composite design Tables III.2 are generated into a second-order polynomial response function model, which predicts IONPs crystallite sizes, expressed by the coded variables (A, B and C) in Equation (07):

$$Y = 61.76 + 8.65\,A + 2.19\,B + 7\,C + 1.48\,AB - 2.35\,AC - 1.5\,BC - 4.63\,A^2 - 4.45\,B^2 - 3.47\,C^2 \quad (07)$$

where Y represents the predicted response the crystallite size, A, B and C are the coded values of the independent variables.

The predicted and actual values of crystallite sizes values of the different variable combinations are listed in Table III.2. Comparing the values of experimental and predicted demonstrates that they are in a very close arrangement.

The values of the coefficients in (Equation 07) express intensity, and signs represent the nature of the influence (positive or negative) of a specific variable on the response. A positive effect of a factor means that the crystallite size is increased by increasing the factor level, while a negative effect indicates that an increase in the factor level reduces IONPs crystallite size [8]. It is clear from (Eq. 3) that A, B, C, AB, has a positive effect on the response (Crystallite size), while some quadratic terms such as AC, BC, A^2, B^2, C^2, have positive effects, taking into account that A-precursor concentration factor and C-Annealing temperature with a coefficient of 8.65 and 7 respectively has more effect on the Crystallite size than the other factors.

IV.3.2 Analysis of variance (ANOVA)

The ANOVA table for response surface methodology of the quadratic model is shown in Table IV. 1. As listed in this table, the model is significant with a P-value < 0.0001 and Fisher's F-value of 481.81. P-values less than 0.05 indicate the model terms are significantly affecting the response. Meanwhile, a greater P-values indicate the non-significantly of the model terms. In our case, all the linear terms have a significant effect on the response with a P-value < 0.0001 and all square terms and their interaction also have significant on the response with a P-values (< 0.05). The effect of the terms on the model is related to their Fisher F-values which is strongly related to their p-values. The higher the F-value, the more significant the individual factors coefficients. From this perspective, the model terms can be classified in this order: A > C > B > AB > BC > AC > C^2 > B^2 > A^2. The Precursor Concentration factor was found to have the greatest influence on the model followed by the Annealing Temperature.

The non-significant shown at the bottom of the Table IV. 1 P-value of lack of fit (more than 0.05) implies that the model fits the experimental data, and the response is significantly influenced by independent variables which indicate that the used quadratic model was effective for the current study. Moreover, from Table IV. 1 it can be seen that predicted R^2 and adjusted R^2 values are in reasonable agreement of 0.9861 and 0.9956

respectively. The adjusted R^2 is in good agreement with the R^2 of 0.9977, suggesting a high correlation between the actual and the predicted values. These three values are close to unity (1) which confirms the adequacy of the model in prediction within the studied range. Adequate precision was used to measure the signal to noise ratio, a ratio more than 4 favorable. In this model the ratio of adequate precision is 66.84, another proof for the model adequacy.

Table IV. 1 Analysis of variance (ANOVA) results for the experimental design.

Source	Sum of Squares	DF	Mean Square	F-value	P-value
Model	2473.70	9	274.86	481.81	< 0.0001[a]
A-Concentration	1022.57	1	1022.57	1792.52	< 0.0001
B-Reaction Temperature	65.62	1	65.62	115.03	< 0.0001
C-Annealing Temperature	669.91	1	669.91	1174.32	< 0.0001
AB	17.43	1	17.43	30.56	0.0003
AC	44.04	1	44.04	77.20	< 0.0001
BC	10.65	1	10.65	18.67	0.0015
A^2	308.70	1	308.70	541.14	< 0.0001
B^2	285.79	1	285.79	500.99	< 0.0001
C^2	173.03	1	173.03	303.31	< 0.0001
Residual	5.70	10	0.5705		
Lack of Fit	4.27	5	0.8533	2.97	0.1289[b]
Pure Error	1.44	5	0.2876		
Cor Total	2479.40	19			

R^2 = 0.9977; **Adjusted *R^2*** = 0.9956; **Predicted *R^2*** = 0.9861. **Adequate Precision** = 66.84

DF degree of freedom.

[a]Significant

[b] Not significant

In Figure IV. 8, the relationship between the predicted and actual values of IONPs crystallite size is shown. The actual values are the calculated values of the crystallite size, which are determined experimentally [9]. On the other hand, predicted values are the values generated by the obtained mathematical model. According to Figure IV. 8, the predicted values of the crystallite size are in respectable agreement with the actual experimental data. The value of the coefficient of determination (R2 = 0.9977) indicates that there is a good

relationship between the predicted and experimental responses. It can be concluded that the model had a great prediction of the studied process within the studied range.

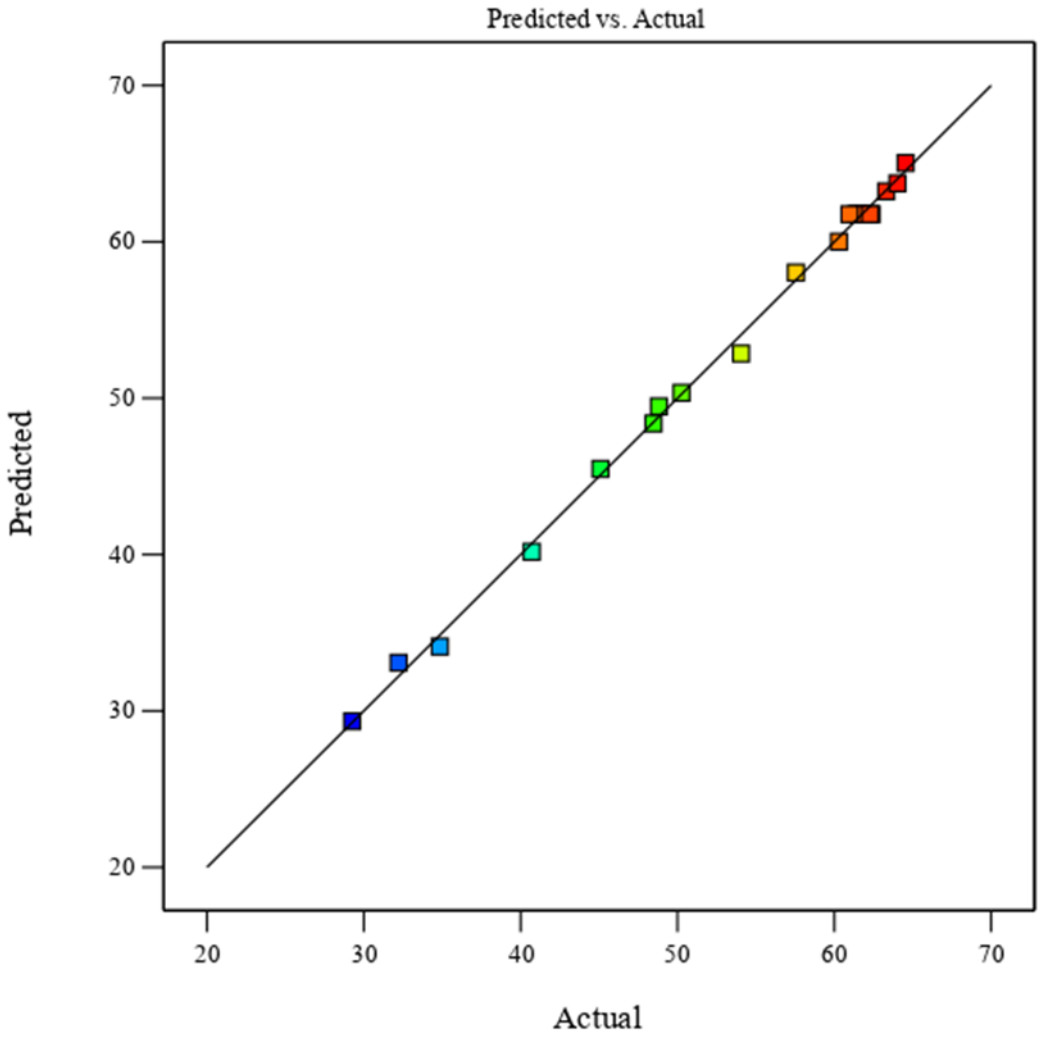

Figure IV. 8 Predicted vs Actual plot.

IV.3.3 Residual's analysis

the difference between the observed value of the dependent variable or response (y) and the predicted value ($\hat{y}$) is called the residual (e). Each data point has one residual.

$$Residual = Observed\ value - Predicted\ value$$

$$e = y - \hat{y}$$

Both the sum and the mean of the residuals are equal to zero. That is, $\Sigma\, e = 0$ and $e = 0$.

The residual plot is a graph that shows the residuals on the vertical axis and the predicted dependent variable on the horizontal axis. If the points in a residual plot are randomly dispersed around the horizontal axis, a linear regression model is appropriate for the data; otherwise, a nonlinear model is more appropriate.

The residual plot in Figure IV. 9 shows a fairly random pattern; some residuals are positive, and some others are negative in random manner. This random pattern indicates that a linear model provides a decent fit to the data.

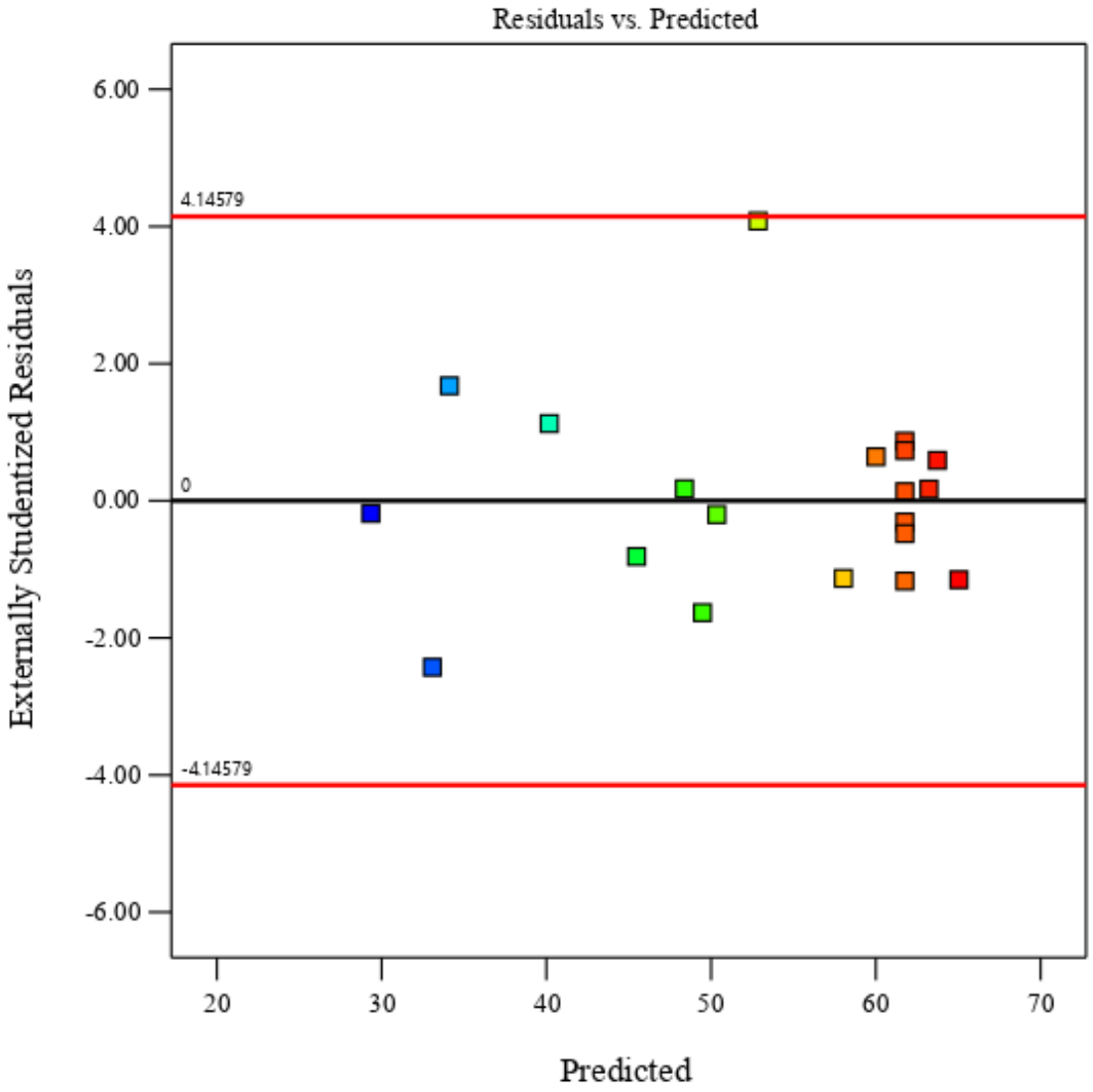

Figure IV. 9 Residuals vs Predicted.

Figure IV. 10 shows the normal probability plot of residuals. This plot indicates whether residuals are normally distributed. If they are normally distributed, the points should lay on an approximately straight line [24,25]. A nonlinear pattern implies that the distribution is not normal, which could be corrected using proper transformation. Worth noting that scattering may be observed even with normal data. According to Figure IV. 10; data are placed on a relatively straight line and, therefore, it can be supposed that they are of normal distribution [26].

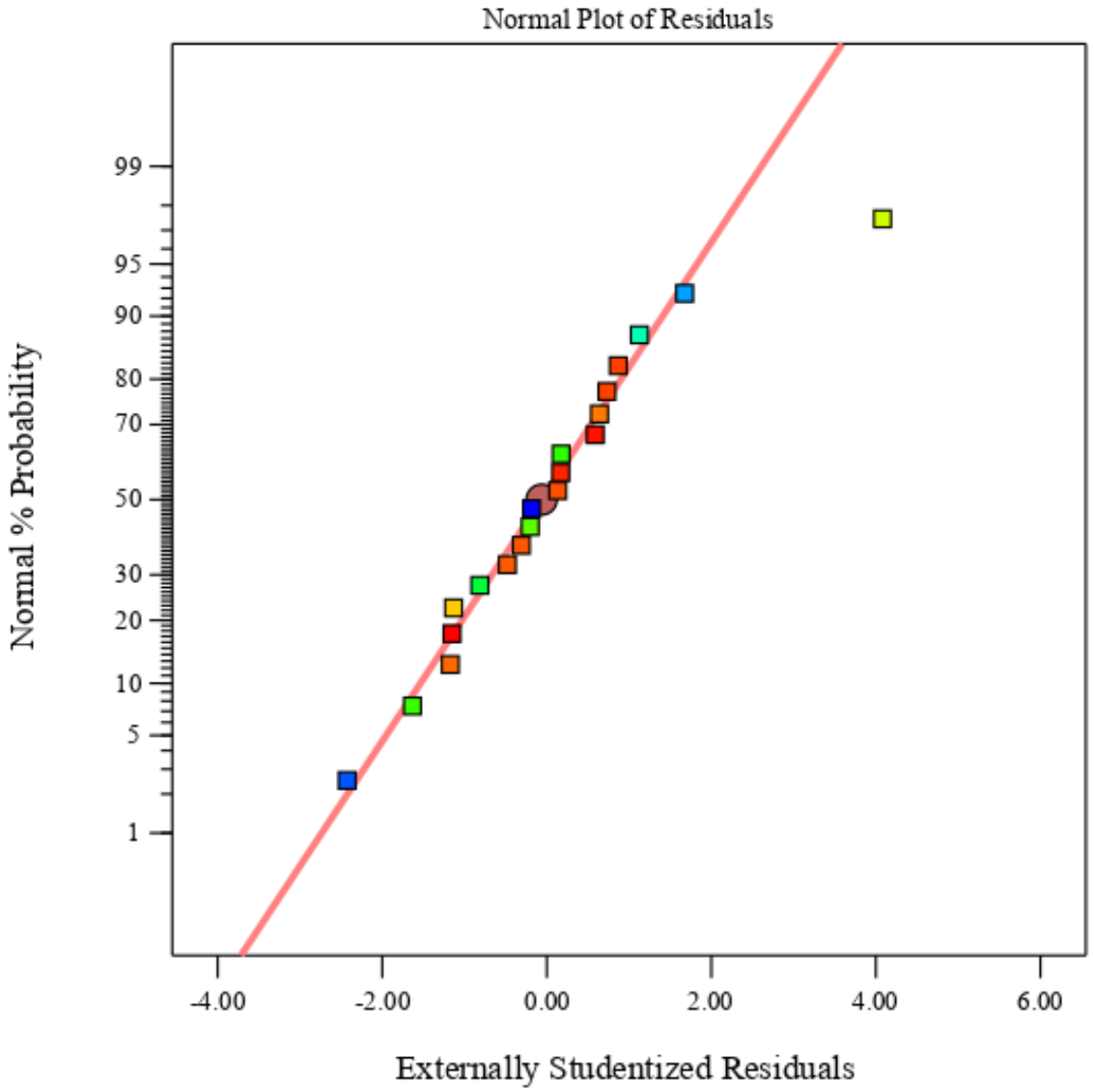

Figure IV. 10 Normal plot of residuals.

IV.3.4 Response surface analysis

The interactive effects of the biosynthesis variables on the response (Crystallite size), is represented as response surfaces with two-dimensional (2D) and three-dimensional (3D) contour plots. Each plot represents the interaction of two biosynthesis parameters while keeping the other parameter at their central level (0). This allows predicting the values crystallite size for different combinations and levels of the biosynthesis parameters.

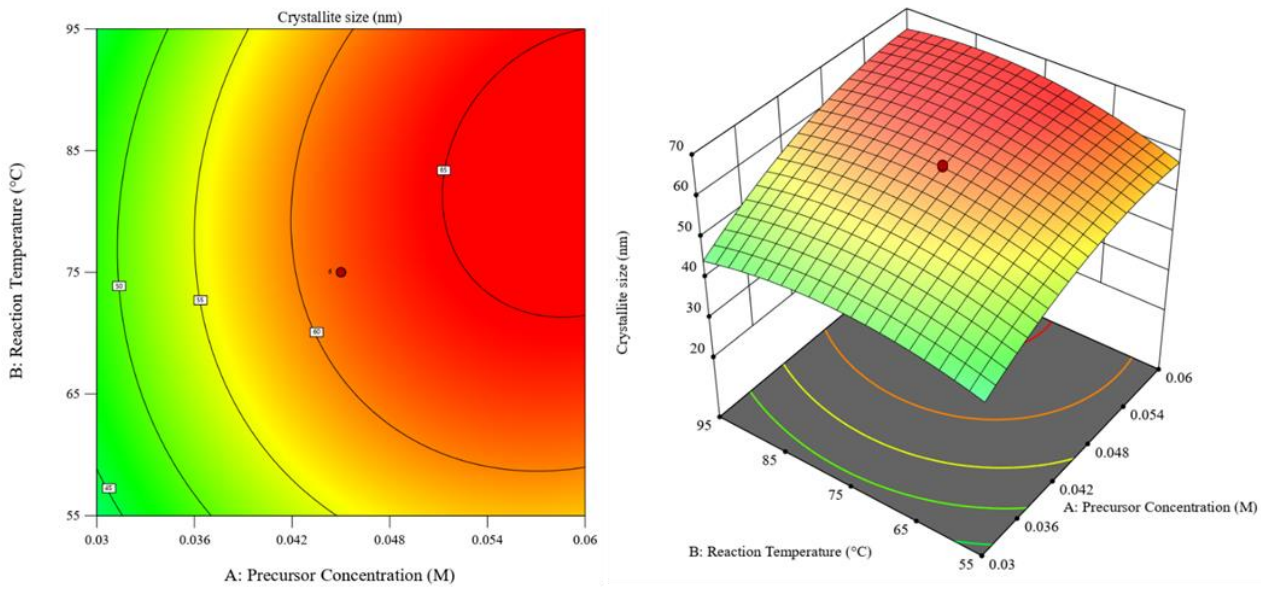

Figure IV. 11 2D and 3D response surface of the combined effect of reaction temperature and precursor concentration on the crystallite size of IONPs.

The 2D contour and 3D surface plots in Figure IV. 11 shows the response surface with respect to precursor concentration and reaction temperature. As shown, IONPs crystallite size increases directly proportional to both precursor concentration and reaction temperature when they increase from (0.03 to 0.06M) and (65 to 80°C) respectively. Further increase in reaction temperature (more than 80°C) have resulted a slight decrease on the crystallite size.

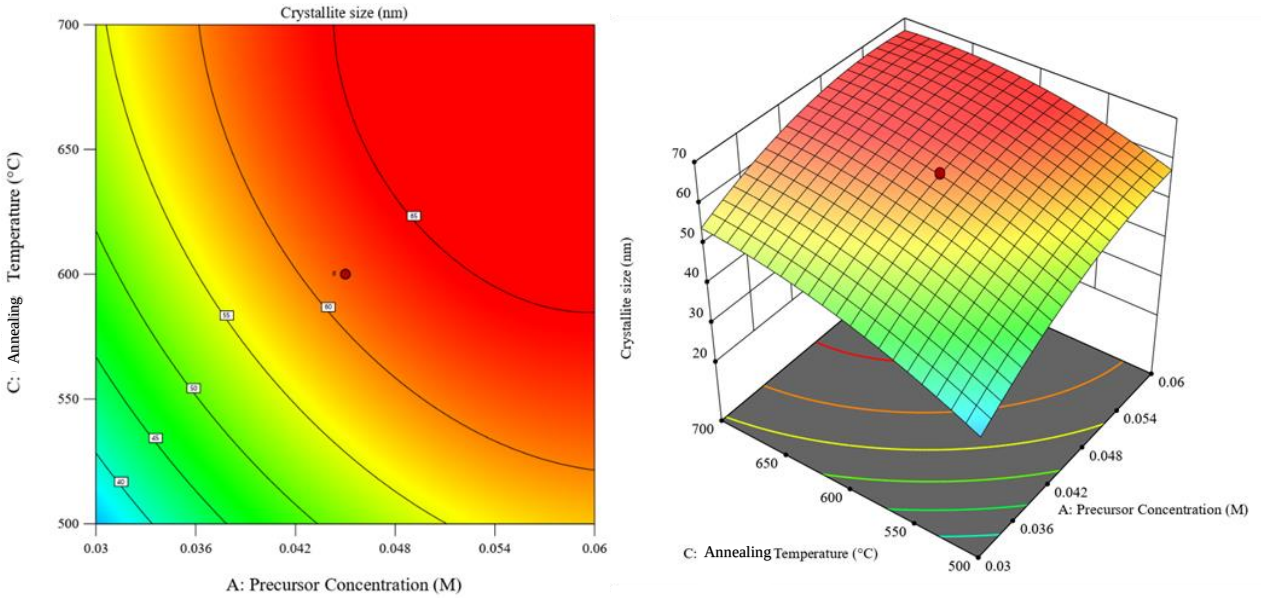

Figure IV. 12 2D and 3D response surface of the combined effect of annealing temperature and precursor concentration on the crystallite size of IONPs.

The precursor concentration verses annealing temperature effect is plotted as 2D and 3D surface plots shown in Figure IV. 12. It's noted that increasing both precursor concentration and annealing temperature have increased the crystallite size significantly. In other words, the crystallite size increases directly proportional to both the annealing temperature and the precursor concentration.

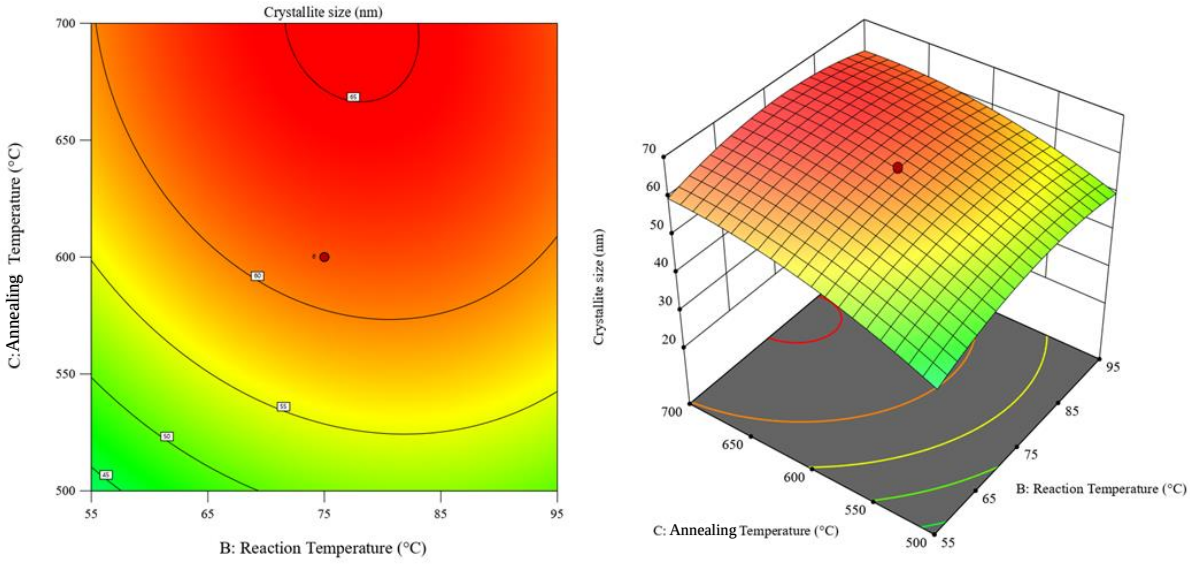

Figure IV. 13 2D and 3D response surface of the combined effect of annealing temperature and reaction temperature on the crystallite size of IONPs.

Figure IV. 13 display the interactive effect of reaction temperature and annealing temperature as 2D and 3D contour plots. The response surfaces indicate that while increasing annealing temperature and reaction temperature, the crystallite size increases significantly until the temperature of reaction passes 80°C; then, the size back to reduce slightly.

The results observed in Figure IV. 11 and Figure IV. 13 demonstrates a trend behavior for reaction temperature effect on the crystallite size; increasing the reaction temperature increases the crystallite size meanwhile at high temperatures (more than 80°C in this work) causes a slight decrease in crystallite size. This finding broadly supports the work of previous studies linking reaction temperature with nanoparticles crystallite size [24]. Which explained this increase of crystallite size with the fact that increasing reaction temperature increases the nucleation rate, resulting in more precursor monomers to be consumed and become crystal nucleus. At this point, if the precursor concentration is sufficient, the precursors would grow faster on the nucleus due to the increased growth rate at high temperatures. In contrast, if there is unsatisfaction in precursor concentration, the

growth would be limited due to the lack of precursor monomers. Consequently, the crystallite size of the NPs decreases [24].

The direct proportional correlation between crystallite size and precursor concentration observed in Figure IV. 11 and Figure IV. 12 are in accord with recent studies indicating that [3,25] the increase of the precursor concentration with sufficient surfactants, increases the concentration of monomers by increasing the number of monomers (growth species) at the same volume. Consequently, the diffusion distance between monomers decreases, leading to higher mass transfer and higher growth. As a result, the crystallite size increases [25].

According to Figure IV. 13 and Figure IV. 12 results, the increase in crystallite size is directly proportional to annealing temperature. This observation may support the hypothesis that increasing annealing temperature increases the amount of thermal energy given to the nanoparticles, leading them to earn a sufficient energy for diffusive motion in what is known by the Oswald ripening process [26]. which is a diffusion process where bigger particles are formed at the expense of small particles [27,28].

IV.3.5 Optimization using the desirability functions

Numerical optimization using the desirabilty function was used obtain the optimum conditions. The possible optimization goals were to maximize, minimize, obtain a solution in specific range or obtain a targeted value of the response. In our case, the optimization goal was set to minimize the response while keeping the rest of the variables “in rage” wich is their maximum (+1) and minimum (-1) levels. Using the previous optimization criteria, a maximum desirability of 0.998 related to minimum crystallite size of 29.26 nm is achieved by setting all the biosynthesis parameters at their inferior levels; i.e., precursor concentration = 0.03 M, reaction temperature = 55°C and annealing temperature 500°C. The optimal condition and their related desirability are shown in Figure IV. 14 and Figure IV. 15 The experimental run executed at the suggested optimal conditions exhibited a crystallite size of 29.18 nm which is in close arrangement with the predicted response, approving the model suitability in the studied range.

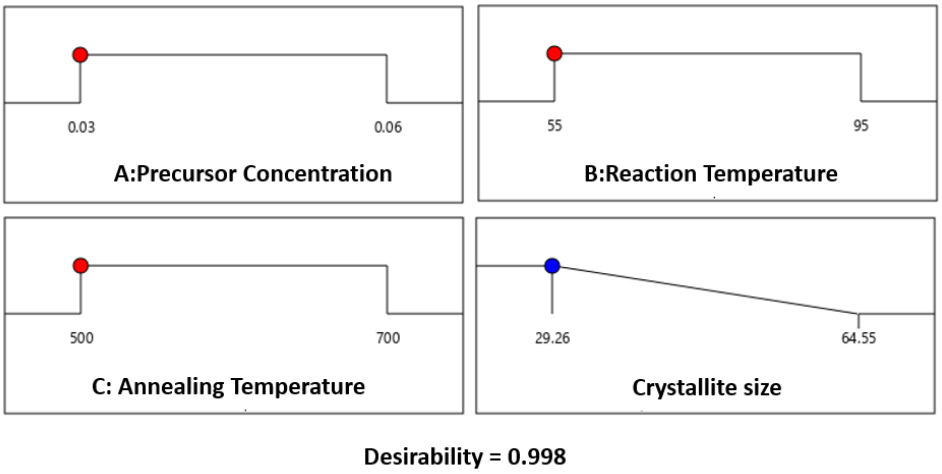

Figure IV. 14 Desirability ramp for the optimal conditions.

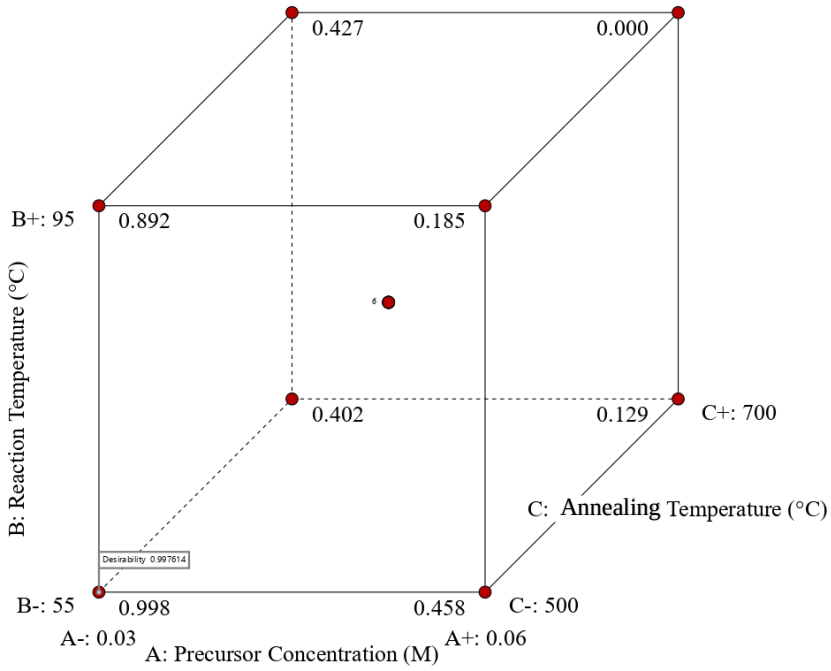

Figure IV. 15 Desirability cube for the optimal conditions.

IV.4 Scanning Electron Microscopy (SEM)

Scanning Electron Microscopy was employed to scan the surface of the biosynthesized IONPs sample at the optimum conditions and study their morphology. The nanoparticles were imaged using (FEI, QUANTA-250 FEG) microscope under a high vacuum and a voltage of 20 Kilovolts**.**

The SEM analysis exhibited an image shown in Figure IV. 16, between the diverse irregular shapes, it's possible to recognize the trend distorted cubes (rhombohedral) structure which further support XRD findings, similar results were demonstrated in prior studies [29],[3].

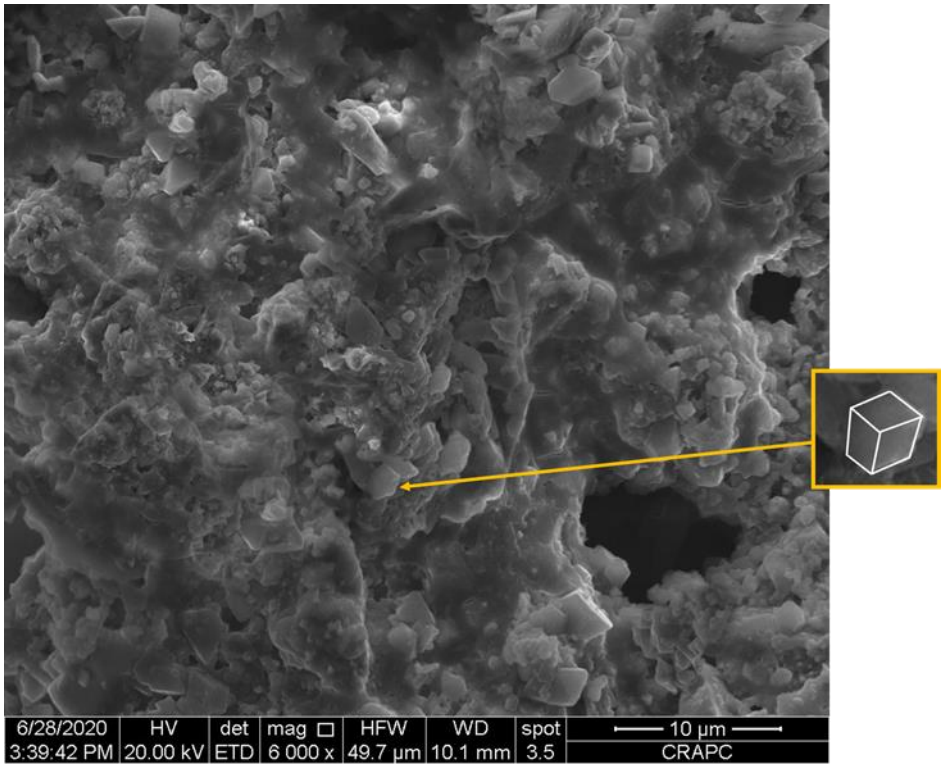

Figure IV. 16 SEM image for the biosynthesized IONPs under the optimum conditions.

IV.5 The Energy Dispersive X-ray analysis (EDX)

EDX was employed to identify the elemental composition of biosynthesized iron oxide nanoparticles at the optimal conditions (Figure IV. 17). The spectrum shown that the sample contains of both Iron (Fe) and Oxygen (O) with different quantities. The weight percentages of Iron and Oxygen were 67.84% and 25.71% respectively. The spectrum also shows the presence of unimportant fraction of Chlorine which may be due to the mineral cell used. Similar results were stated in former works [30,31].

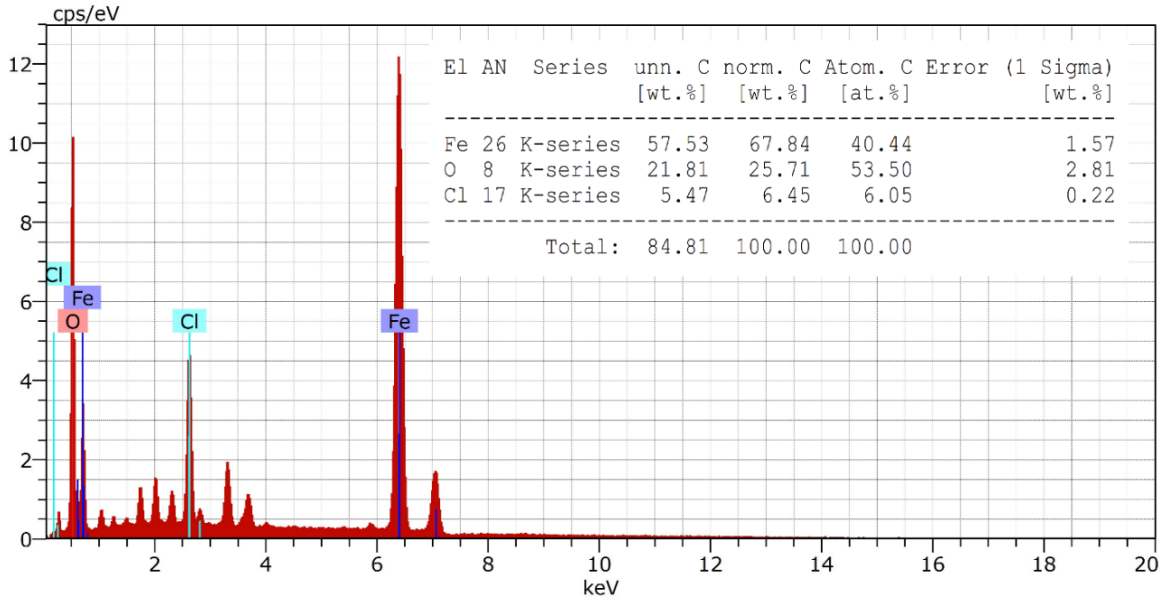

Figure IV. 17 EDX spectrum of IONPs at the optimal conditions.

IV.6 Antibacterial activity of IONPs

The disk diffusion method was used to study the antibacterial activity of IONPs against both gram-positive (Staphylococcus aureus) and gram-negative (Escherichia coli) bacteria. Furthermore, the effect of crystallite size on antimicrobial activity was investigated by measuring the inhibition zone of different size samples of IONPs. The results of the antibacterial test are shown in Figure IV. 18 and Figure IV. 19.

Table IV. 2 The inhibition zones for the different samples.

Sample	Crystallite size (nm)	Escherichia coli	Staphylococcus aureus
Control	-	0	0
Gentamicin (120 µg)	-	36.3 ± 1.98	32.7 ± 2.31
Run 01	61.76	13 ± 2.09	12.4 ± 1.9
Run 05	29.34	22 ± 1.22	20 ± 1.04
Run 17	50.35	16 ± 0.89	14 ± 0.62
Run 20	45.09	18 ± 2	17 ± 0.83

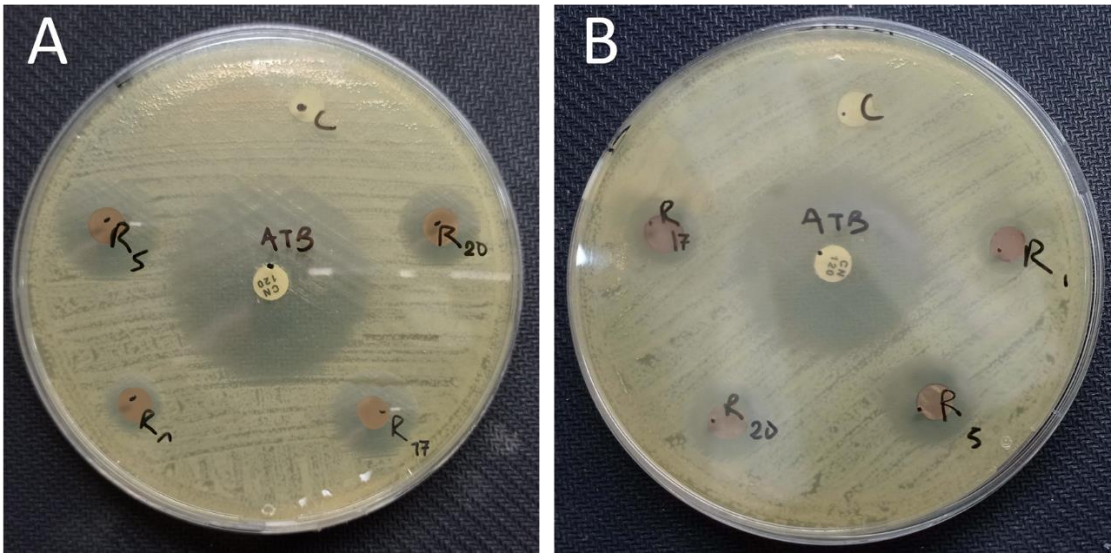

Figure IV. 18 The antibacterial activity of IONPs against (A) Escherichia Coli and (B) Staphylococcus aureus. R5-run 05, R1-run 01, R17-run 17, R20-run 20, ATB-Antibiotic (Gentamicin 120 µg).

The results indicate that the biosynthesized nanoparticles and antibiotics inhibited the growth of both gram-positive and gram-negative microorganisms. Comparing the inhibition zones for each sample against gram-positive and gram-negative bacteria shows that gram-negative bacteria have more significant inhabitation zones. Pervious study have demonstrated that the variance in antibacterial activity is due to the differences in each bacteria type's construction and composition of cell membranes [32]. Gram-negative bacteria have thinner peptidoglycan cell membranes compared to Gram-positive bacteria. Therefore, IONPs penetrates it easier, causing a higher antibacterial activity [33].

IV.5.1 The effect of the crystallite size on the antibacterial activity of IONPs

The different sizes of IONPs have resulted different inhabitation zones diameters. The effect of IONPs crystallite size on the antibacterial activity against gram-positive and gram-negative bacteria is shown in Figure IV. 20, higher antibacterial activity was obtained at lower crystallite sizes. In other words, decreasing the crystallite size increases the antibacterial activity. This result is in accord with recent studies indicating that the smaller the nanoparticles size the higher antibacterial activity; the smaller sizes NP penetrates in to the cell easier compared the bigger counterparts, which causing more damage to the bacteria [34–37].

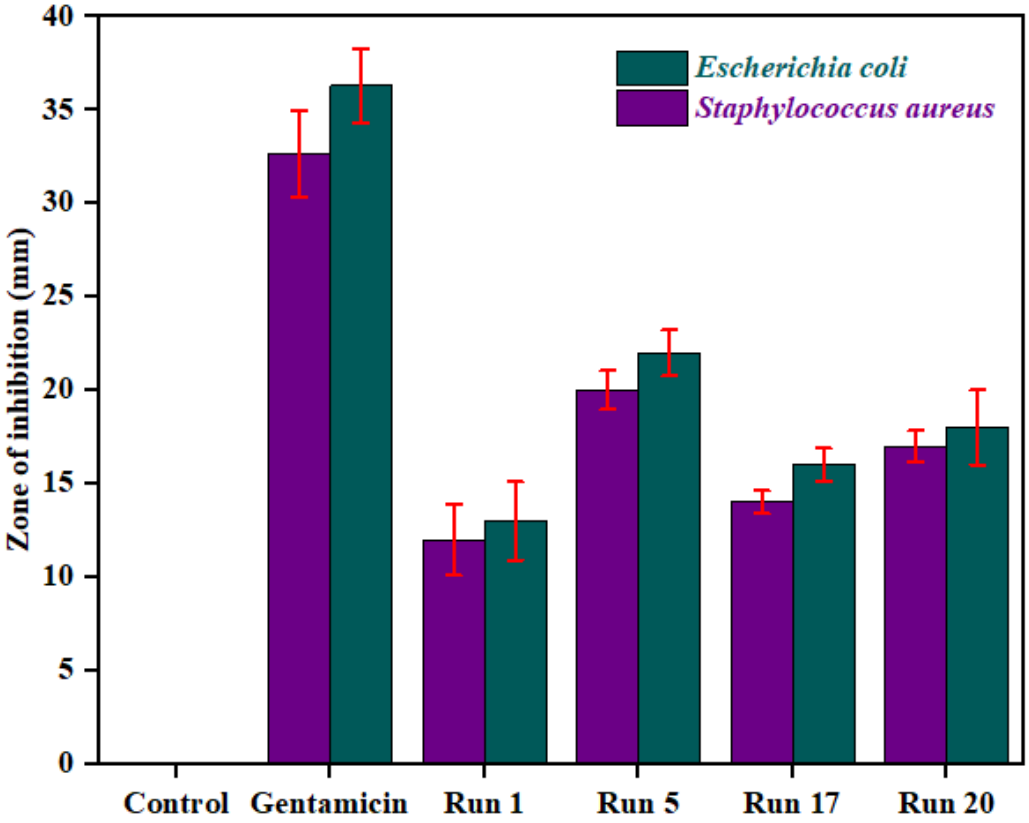

Figure IV. 19 The antibacterial activity of different samples of IONPs against (A) Escherichia Coli and (B) Staphylococcus aureus

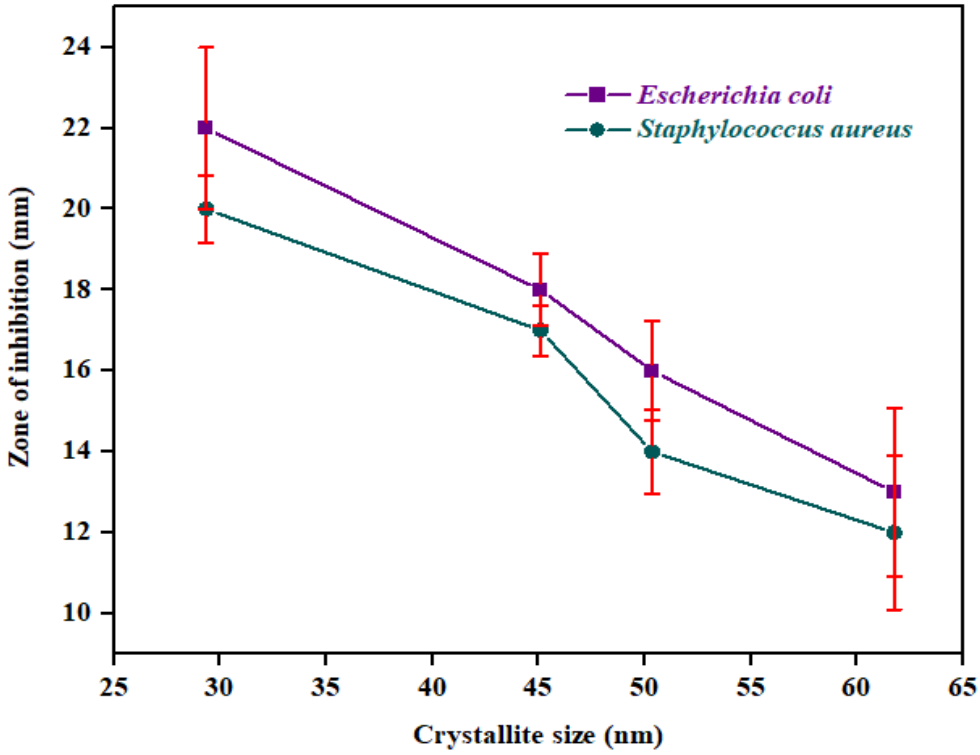

Figure IV. 20 The effect of IONPs crystallite size on the antibacterial activity against gram-positive and gram-negative bacteria

IV.5.2 The antibacterial mechanisms of IONPs

The three proposed antibacterial mechanisms of IONPs against bacterial cells are shown in Figure IV. 21. The first mechanism suggests that IONPs enable the formation of reactive oxygen species (ROS) such as hydroxyl ions and hydrogen peroxide, which causes oxidative stress and damages the cell membrane and DNA, leading to bacterial death [38]. The second mechanism by the dissolution of IONPs into iron ions, which is known to inhibit several bacterial cells activities by interfering with enzyme, amino acid, and protein metabolisms causing bacterial death [39]; and the third mechanism propose that IONPs interact directly with cell membrane through electrostatic forces, which damages the membrane plasma, and causes intracellular content leaks [40].

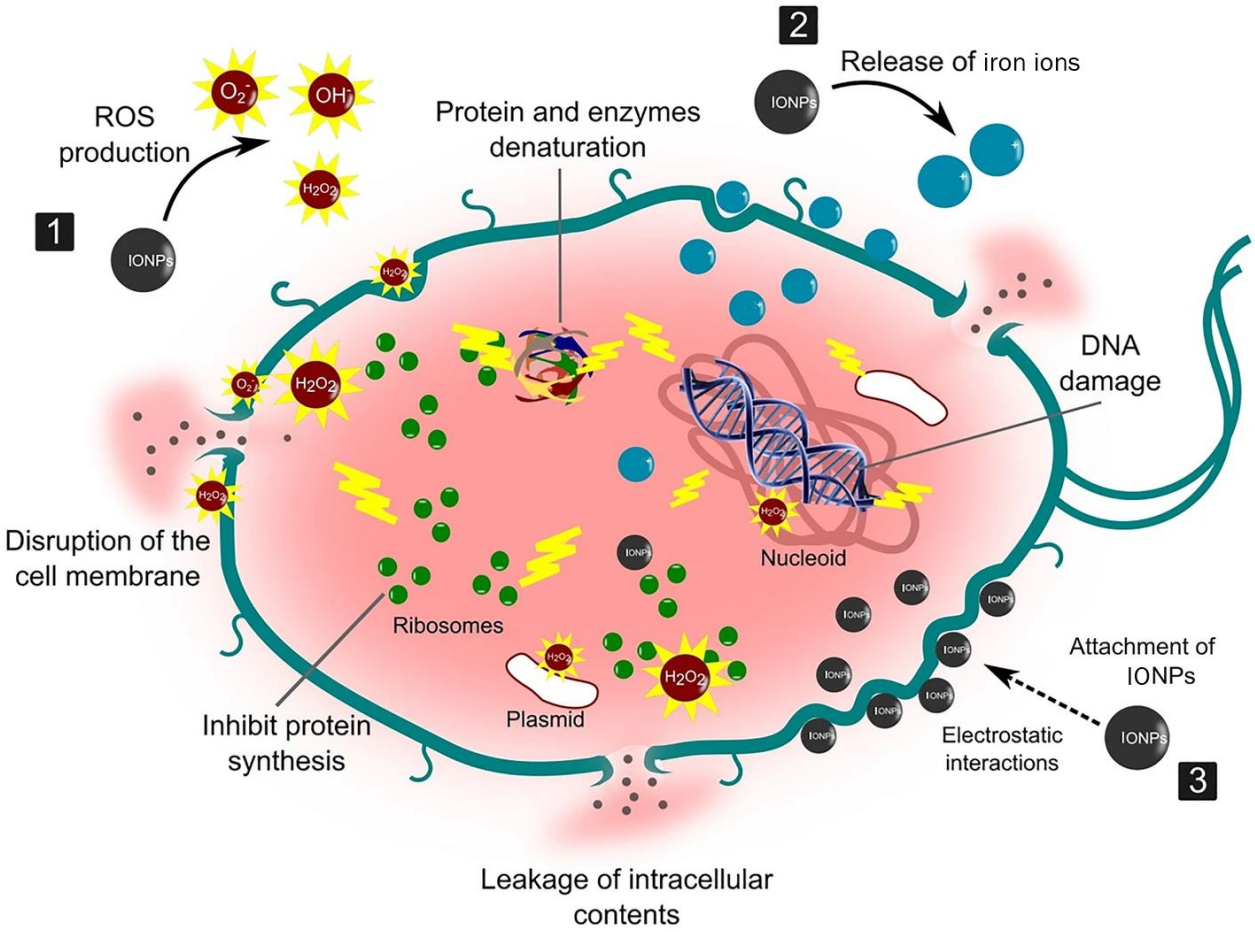

Figure IV. 21 Schematic illustration shows the proposed antibacterial mechanisms of IONPs against bacterial cells [40].

References

[1] T.M. Laid, K. Abdelhamid, L.S. Eddine, B. Abderrhmane, Optimizing the biosynthesis parameters of iron oxide nanoparticles using central composite design, J. Mol. Struct. (2020) 129497. https://doi.org/10.1016/j.molstruc.2020.129497.

[2] M. Mahdavi, F. Namvar, M. Ahmad, R. Mohamad, Green Biosynthesis and Characterization of Magnetic Iron Oxide (Fe3O4) Nanoparticles Using Seaweed (Sargassum muticum) Aqueous Extract, Molecules. 18 (2013) 5954–5964. https://doi.org/10.3390/molecules18055954.

[3] A. Bouafia, S.E. Laouini, Green synthesis of iron oxide nanoparticles by aqueous leaves extract of Mentha Pulegium L.: Effect of ferric chloride concentration on the type of product, Mater. Lett. 265 (2020) 127364–127368. https://doi.org/10.1016/j.matlet.2020.127364.

[4] D. Badmapriya, I. V. Asharani, Dye degradation studies catalysed by green synthesized iron oxide nanoparticles, Int. J. ChemTech Res. 9 (2016) 409–416.

[5] S. Groiss, R. Selvaraj, T. Varadavenkatesan, R. Vinayagam, Structural characterization, antibacterial and catalytic effect of iron oxide nanoparticles synthesised using the leaf extract of Cynometra ramiflora, J. Mol. Struct. 1128 (2017) 572–578. https://doi.org/10.1016/j.molstruc.2016.09.031.

[6] W.H. Strehlow, E.L. Cook, Compilation of Energy Band Gaps in Elemental and Binary Compound Semiconductors and Insulators, J. Phys. Chem. Ref. Data. 2 (1973) 163–200. https://doi.org/10.1063/1.3253115.

[7] P. Mallick, B.N. Dash, X-ray diffraction and UV-visible characterizations of α-Fe2O3 nanoparticles annealed at different temperature, J. Nanosci. Nanotechnol. 3 (2013) 130–134. https://doi.org/10.5923/j.nn.20130305.04.

[8] P. Jayaprakash, M.P. Mohamed, M.L. Caroline, Growth, spectral and optical characterization of a novel nonlinear optical organic material: d-Alanine dl-Mandelic acid single crystal, J. Mol. Struct. 1134 (2017) 67–77. https://doi.org/10.1016/j.molstruc.2016.12.026.

[9] M. Gartner, M. Crisan, A. Jitianu, R. Scurtu, R. Gavrila, I. Oprea, M. Zaharescu,

Spectroellipsometric Characterization of Multilayer Sol-Gel Fe 2 O 3 Films, J. Sol-Gel Sci. Technol. 26 (2003) 745–748. https://doi.org/10.1023/A:1020706423230.

[10] N. Özer, F. Tepehan, Optical and electrochemical characteristics of sol–gel deposited iron oxide films, Sol. Energy Mater. Sol. Cells. 56 (1999) 141–152. https://doi.org/10.1016/S0927-0248(98)00152-4.

[11] G. Zotti, G. Schiavon, S. Zecchin, U. Casellato, Electrodeposition of Amorphous Fe2 O 3 Films by Reduction of Iron Perchlorate in Acetonitrile, J. Electrochem. Soc. 145 (1998) 385–389. https://doi.org/10.1149/1.1838273.

[12] M.F. Al-Kuhaili, M. Saleem, S.M.A. Durrani, Optical properties of iron oxide (α-Fe2O3) thin films deposited by the reactive evaporation of iron, J. Alloys Compd. 521 (2012) 178–182. https://doi.org/10.1016/j.jallcom.2012.01.115.

[13] L. Dghoughi, B. Elidrissi, C. Bernède, M. Addou, M.A. Lamrani, M. Regragui, H. Erguig, Physico-chemical, optical and electrochemical properties of iron oxide thin films prepared by spray pyrolysis, Appl. Surf. Sci. 253 (2006) 1823–1829. https://doi.org/10.1016/j.apsusc.2006.03.021.

[14] G.B. Sakura, A.Y.T. Leung, Experimental Study of Particle Collection Efficiency of Cylindrical Inlet Type Cyclone Separator, Int. J. Environ. Sci. Dev. 6 (2015) 160–164. https://doi.org/10.7763/ijesd.2015.v6.581.

[15] N. Izza, S.R. Dewi, A. Setyanda, A. Sukoyo, P. Utoro, Di.F. Al Riza, Y. Wibisono, Microwave-assisted extraction of phenolic compounds from Moringa oleifera seed as anti-biofouling agents in membrane processes, MATEC Web Conf. 204 (2018) 03003–03009. https://doi.org/10.1051/matecconf/201820403003.

[16] O.S. Bello, K.A. Adegoke, O.O. Akinyunni, Preparation and characterization of a novel adsorbent from Moringa oleifera leaf, Appl. Water Sci. 7 (2017) 1295–1305. https://doi.org/10.1007/s13201-015-0345-4.

[17] C.S.T. Araújo, E.I. Melo, V.N. Alves, N.M.M. Coelho, Moringa oleifera Lam. seeds as a natural solid adsorbent for removal of AgI in aqueous solutions, J. Braz. Chem. Soc. 21 (2010) 1727–1732. https://doi.org/10.1590/S0103-50532010000900019.

[18] S. Kanagasubbulakshmi, K. Kadirvelu, Green synthesis of Iron oxide nanoparticles using Lagenaria siceraria and evaluation of its Antimicrobial activity, Def. Life Sci.

J. 2 (2017) 422–427. https://doi.org/10.14429/dlsj.2.12277.

[19] N. Marooufpour, M. Alizadeh, M. Hatami, B. Asgari Lajayer, Biological Synthesis of Nanoparticles by Different Groups of Bacteria, in: Microb. Nanobionics, Springer, 2019: pp. 63–85. https://doi.org/10.1007/978-3-030-16383-9_3.

[20] I. Abdulkadir, H.M.I. Abdallah, S.B. Jonnalagadda, B.S. Martincigh, The effect of synthesis method on the structure,and magnetic and photocatalytic properties of hematite (α-Fe2O3) nanoparticles - research article, South African J. Chem. 71 (2018) 68–78. https://doi.org/10.17159/0379-4350/2018/v71a9.

[21] J. Vidal-Vidal, J. Rivas, M.A. López-Quintela, Synthesis of monodisperse maghemite nanoparticles by the microemulsion method, Colloids Surfaces A Physicochem. Eng. Asp. 288 (2006) 44–51. https://doi.org/10.1016/j.colsurfa.2006.04.027.

[22] D.M. Yufanyi, A.M. Ondoh, J. Foba-Tendo, K.J. Mbadcam, Effect of Decomposition Temperature on the Crystallinity of α-Fe 2 O 3 (Hematite) Obtained from an Iron(III)-Hexamethylenetetramine Precursor, Am. J. Chem. 5 (2015) 1–9. https://doi.org/10.5923/j.chemistry.20150501.01.

[23] E. Darezereshki, F. Bakhtiari, M. Alizadeh, A. Behrad vakylabad, M. Ranjbar, Direct thermal decomposition synthesis and characterization of hematite (α-Fe2O3) nanoparticles, Mater. Sci. Semicond. Process. 15 (2012) 91–97. https://doi.org/10.1016/j.mssp.2011.09.009.

[24] C. Moya, X. Batlle, A. Labarta, The effect of oleic acid on the synthesis of Fe3-xO4 nanoparticles over a wide size range, Phys. Chem. Chem. Phys. 17 (2015) 27373–27379. https://doi.org/10.1039/c5cp03395k.

[25] J. Cao, Y. Wu, Y. Jin, P. Yilihan, W. Huang, Response surface methodology approach for optimization of the removal of chromium(VI) by NH2-MCM-41, J. Taiwan Inst. Chem. Eng. 45 (2014) 860–868. https://doi.org/10.1016/j.jtice.2013.09.011.

[26] V. Kumar Gupta, S. Agarwal, M. Asif, A. Fakhri, N. Sadeghi, Application of response surface methodology to optimize the adsorption performance of a magnetic graphene oxide nanocomposite adsorbent for removal of methadone from the environment, J. Colloid Interface Sci. 497 (2017) 193–200. https://doi.org/10.1016/j.jcis.2017.03.006.

[27] H. Liu, H. Zhang, J. Wang, J. Wei, Effect of temperature on the size of biosynthesized

silver nanoparticle: Deep insight into microscopic kinetics analysis, Arab. J. Chem. 13 (2020) 1011–1019. https://doi.org/10.1016/j.arabjc.2017.09.004.

[28] H. Sharifi Dehsari, A. Halda Ribeiro, B. Ersöz, W. Tremel, G. Jakob, K. Asadi, Effect of precursor concentration on size evolution of iron oxide nanoparticles, CrystEngComm. 19 (2017) 6694–6702. https://doi.org/10.1039/c7ce01406f.

[29] O. Amadine, Y. Essamlali, A. Fihri, M. Larzek, M. Zahouily, Effect of calcination temperature on the structure and catalytic performance of copper–ceria mixed oxide catalysts in phenol hydroxylation, RSC Adv. 7 (2017) 12586–12597. https://doi.org/10.1039/C7RA00734E.

[30] I.P.T. Indrayana, L.A. Tjuana, M.T. Tuny, Kurnia, Nanostructure and Optical Properties of Fe 3 O 4 : Effect of Calcination Temperature and Dwelling Time, J. Phys. Conf. Ser. 1341 (2019) 082044–082053. https://doi.org/10.1088/1742-6596/1341/8/082044.

[31] C.-C. Diao, C.-Y. Huang, C.-F. Yang, C.-C. Wu, Morphological, Optical, and Electrical Properties of p-Type Nickel Oxide Thin Films by Nonvacuum Deposition, Nanomaterials. 10 (2020) 636–651. https://doi.org/10.3390/nano10040636.

[32] F.N. Sayed, V. Polshettiwar, Facile and Sustainable Synthesis of Shaped Iron Oxide Nanoparticles: Effect of Iron Precursor Salts on the Shapes of Iron Oxides, Sci. Rep. 5 (2015) 9733–9747. https://doi.org/10.1038/srep09733.

[33] P. Rajiv, B. Bavadharani, M.N. Kumar, P. Vanathi, Synthesis and characterization of biogenic iron oxide nanoparticles using green chemistry approach and evaluating their biological activities, Biocatal. Agric. Biotechnol. 12 (2017) 45–49. https://doi.org/https://doi.org/10.1016/j.bcab.2017.08.015.

[34] S.S.U. Rahman, M.T. Qureshi, K. Sultana, W. Rehman, M.Y. Khan, M.H. Asif, M. Farooq, N. Sultana, Single step growth of iron oxide nanoparticles and their use as glucose biosensor, Results Phys. 7 (2017) 4451–4456. https://doi.org/https://doi.org/10.1016/j.rinp.2017.11.001.

[35] V.V.T. Padil, M. Černík, Green synthesis of copper oxide nanoparticles using gum karaya as a biotemplate and their antibacterial application, Int. J. Nanomedicine. 8 (2013) 889.

[36] X. Liang, M. Sun, L. Li, R. Qiao, K. Chen, Q. Xiao, F. Xu, Preparation and antibacterial activities of polyaniline/Cu 0.05Zn 0.95O nanocomposites, Dalt. Trans. 41 (2012) 2804–2811. https://doi.org/10.1039/c2dt11823h.

[37] Y.-N. Chang, M. Zhang, L. Xia, J. Zhang, G. Xing, The Toxic Effects and Mechanisms of CuO and ZnO Nanoparticles, Mater. . 5 (2012). https://doi.org/10.3390/ma5122850.

[38] S. Kanagasubbulakshmi, K. Kadirvelu, Green synthesis of Iron oxide nanoparticles using Lagenaria siceraria and evaluation of its Antimicrobial activity, Def. Life Sci. J. 2 (2017) 422. https://doi.org/10.14429/dlsj.2.12277.

[39] W. Ahmad, K. Kumar Jaiswal, M. Amjad, Euphorbia herita leaf extract as a reducing agent in a facile green synthesis of iron oxide nanoparticles and antimicrobial activity evaluation, Inorg. Nano-Metal Chem. 51 (2021) 1147–1154. https://doi.org/10.1080/24701556.2020.1815062.

[40] W. Ahmad, K.K. Jaiswal, S. Soni, Green synthesis of titanium dioxide (TiO2) nanoparticles by using Mentha arvensis leaves extract and its antimicrobial properties, Inorg. Nano-Metal Chem. 50 (2020) 1032–1038. https://doi.org/10.1080/24701556.2020.1732419.

[41] S. Soren, S. Kumar, S. Mishra, P.K. Jena, S.K. Verma, P. Parhi, Evaluation of antibacterial and antioxidant potential of the zinc oxide nanoparticles synthesized by aqueous and polyol method, Microb. Pathog. 119 (2018) 145–151. https://doi.org/https://doi.org/10.1016/j.micpath.2018.03.048.

[42] S.F. Mossallam, E.I. Amer, R.G. Diab, Potentiated anti-microsporidial activity of Lactobacillus acidophilus CH1 bacteriocin using gold nanoparticles, Exp. Parasitol. 144 (2014) 14–21. https://doi.org/https://doi.org/10.1016/j.exppara.2014.06.002.

[43] H. Mohd Yusof, R. Mohamad, U.H. Zaidan, N.A. Abdul Rahman, Microbial synthesis of zinc oxide nanoparticles and their potential application as an antimicrobial agent and a feed supplement in animal industry: a review, J. Anim. Sci. Biotechnol. 10 (2019) 57. https://doi.org/10.1186/s40104-019-0368-z.

GENERAL CONCLUSION

General conclusion

Nanoscience and nanotechnology have attracted the interest of research committees in many specialties due to their exceptional features applicable in many fields. It represents a mutual interest that unites physics, chemistry, and biology to resolve many challenges exploiting the unique features of nanomaterials.

These unique properties of nanomaterials are strongly dependent on their size and shape, which has motivated many studies to search for a size-controlled synthesis of nanomaterials. It was found that synthesis parameters affect the size of the nanomaterials, making it possible to control the size by adjusting synthesis parameters.

The development in nanomaterials has been followed by rising concerns about the toxic methods used for their production. These concerns are faded by implementing sustainable green chemistry in nanomaterials production, which allowed the production of low-cost, non-toxic, and eco-friendly nanomaterials.

Since the reduced size is assigned to more desirable properties, this work aims to optimize the biosynthesis temperature of IONPs by obtaining the optimal conditions that result in a minimum IONPs crystallite size and to study their biological activity. A green and non-toxic method was used to biosynthesize IONPs using *Moringa Oleifera* leaves extract. Different characterization techniques were used to confirm and study the biosynthesized IONPs. The optical characterization techniques UV-visible and FTIR analysis showed characteristic absorption bands assigned to IONPs confirming their formation. Furthermore, FTIR analysis results indicated that the polyphenolic groups presented in *Moringa Oleifera* leaves extract played a vital role in reducing and stabilizing IONPs.

XRD analysis results showed common peaks in all the samples, indicating the formation of a pure Hematite (α-Fe_2O_3) with a rhombohedral geometry. XRD patterns and Scherrer's formula allowed the estimation of IONPs crystallite size that ranged from 29.26 to 64.55 nm.

SEM analysis indicates that the biosynthesized IONPs are of different sizes and shapes; however, a trend shape of distorted cubes (rhombohedral) was observed on the sample surface, which agrees with XRD results.

Unlike the non-efficient traditional studies that study individual factors, this study uses a modern optimization technique that efficiently studies the combined effect of different factors known as design of experiments (DOE). Response surface methodology (RSM)

based on central composite design (CCD) was used to study the combined influence of three different biosynthesis parameters; reaction temperature, annealing temperature, and precursor concentration on IONPs crystallite size.

The ANOVA results have proven the model validity for this study and shown that the size of IONPs is significantly influenced by all the studied factors and their interactions. Within the studied range, an optimal crystallite size of 29.26 nm was obtained using numerical optimization and the desirability function. The optimum crystallite size was reached at a reaction temperature of 55 °C, annealing temperature adjusted to 500 °C, and the precursor concentration of 0.03 M.

The Normal plot, ANOVA, and R^2 values suggest a good correlation between the experimental and the predicted values; additionally, a confirmatory run at the suggested optimal conditions exhibited a crystallite size of 29.18 nm, which is in good concordance with the predicted response confirming the model adequacy in prediction and finding the optimal conditions within the studied range.

The antibacterial activity of IONPs was tested using the disk diffusion method. The biosynthesized IONPs have shown significant antibacterial activity against both gram-positive and gram-negative bacteria. However, the activity was strongly influenced by the crystallite size of IONPs; higher antibacterial activity was obtained at smaller sizes.

This study has gone some way towards enhancing our understanding of the combined effect of different biosynthesis parameters on the crystallite size, allowing better control over the size and optimizing the biosynthesis by selecting optimized synthesis conditions, including temperature.

Further studies can extend the present work to consider investigating more biosynthesis parameters added to the ones examined in this study, allowing better control over the IONPs size and enhancing the biosynthesis process by obtaining more precise optimal conditions.

APPENDIXES

Appendix I

The used software

Design Expert 13

Design Expert (version 13) statistical software was employed to constructing the experimental design and analyzing the obtained data by generating the different statistical reports and plots, investigating the different effects of the chosen variables, and determining the optimal conditions

VESTA software

Vesta software was used to draw the Crystal structures of hematite, magnetite, and maghemite

Appendix II

Additional model graphs

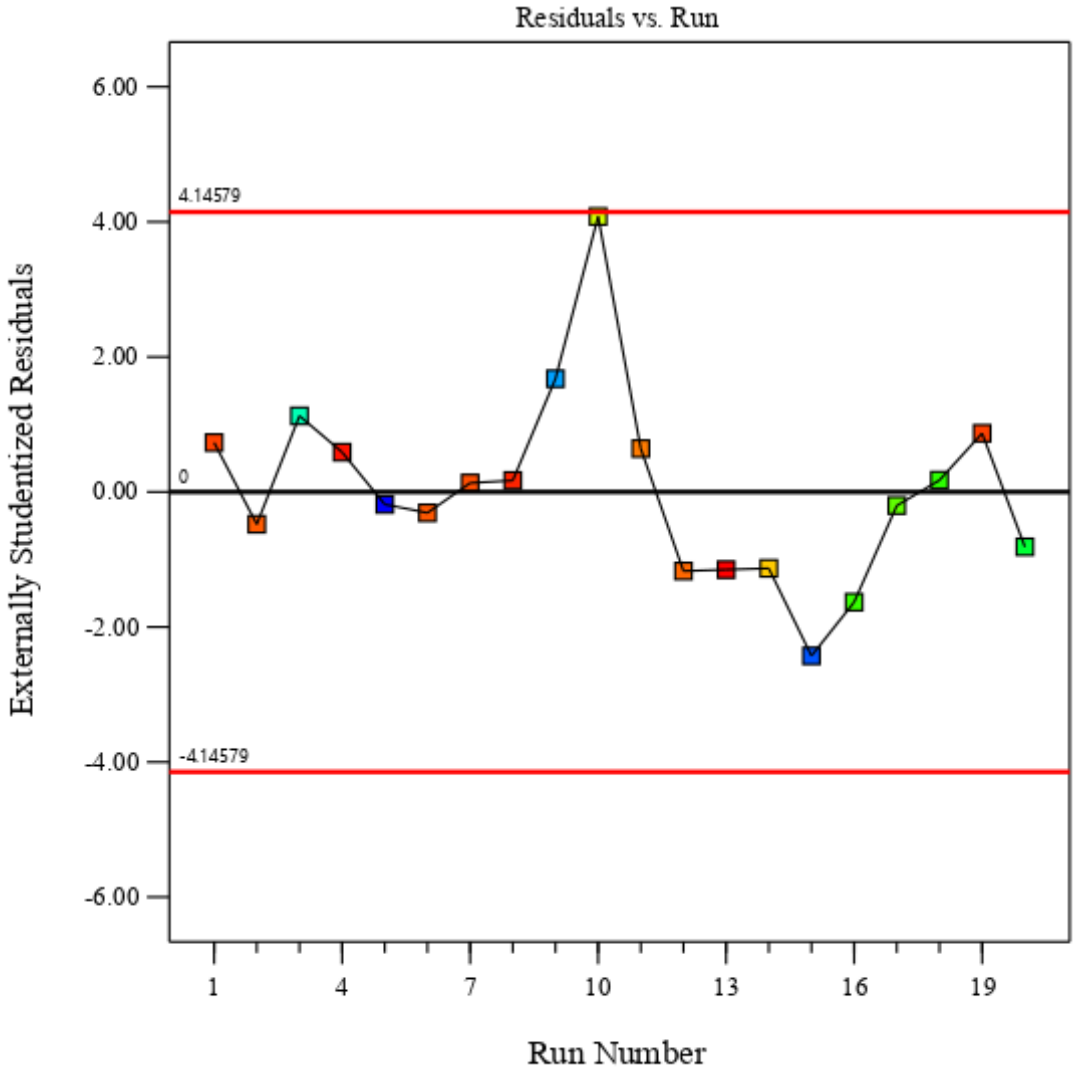

Figure 1 Residuals vs Run Plot

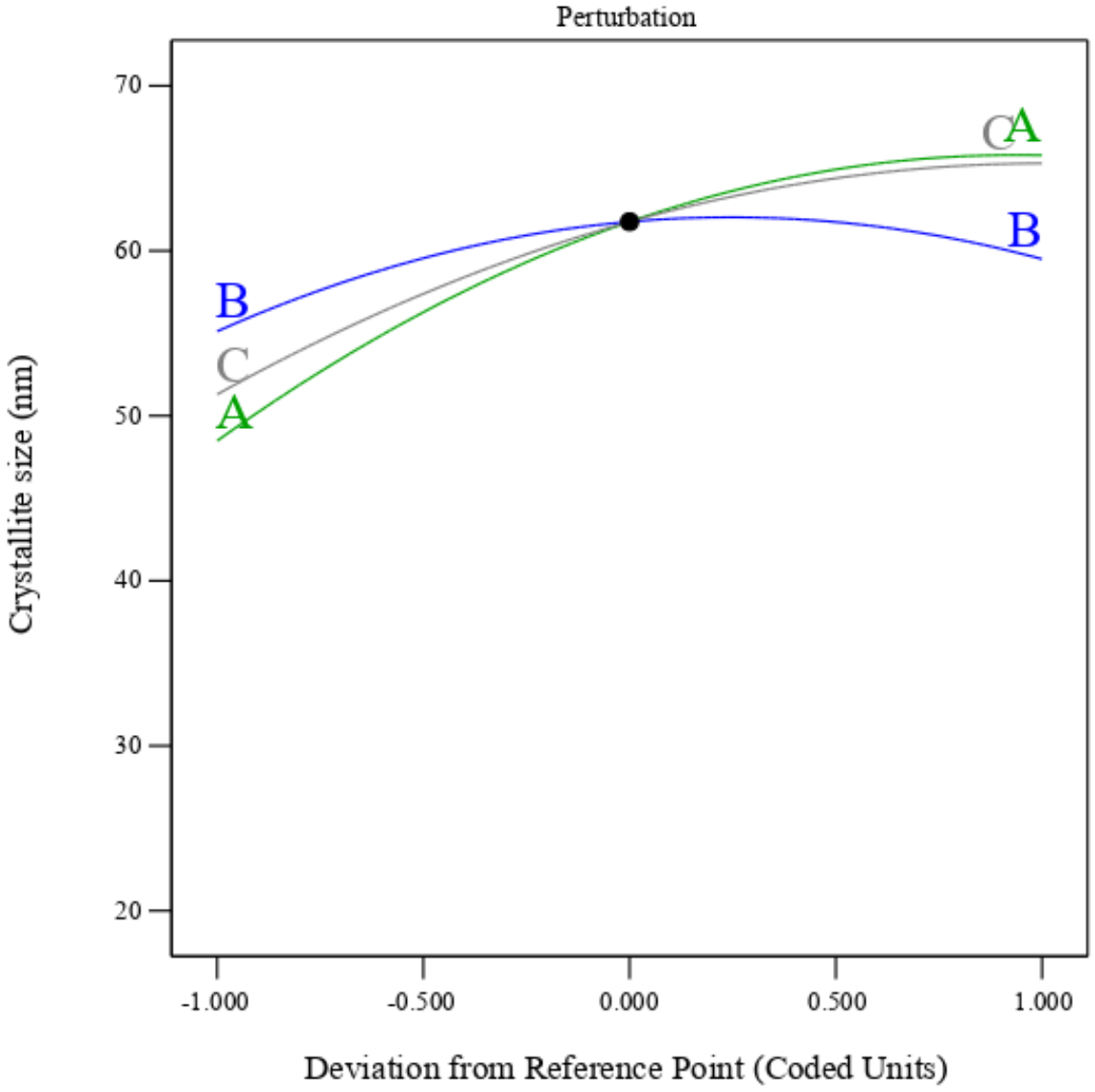

Figure 2 Perturbation vs response plot.

SCIENTIFIC PUBLICATIONS

Articles on 'A' Class Journals

M.L. Tedjani, A. Khelef, S.E. Laouini, A. Bouafia, Optimizing the biosynthesis parameters of iron oxide nanoparticles using central composite design, J. Mol. Struct. (2020) 129497. https://doi.org/10.1016/j.molstruc.2020.129497.

A. Bouafia, S.E. Laouini, A. Khelef, **M.L. Tedjani**, F. Guemari, Effect of Ferric Chloride Concentration on the Type of Magnetite (Fe3O4) Nanoparticles Biosynthesized by Aqueous Leaves Extract of Artemisia and Assessment of Their Antioxidant Activities, J. Clust. Sci. (2020) 1–9. https://doi.org/10.1007/s10876-020-01868-7.

A. Bouafia, S.E. Laouini, **M.L. Tedjani**, G.A.M. Ali, A. Barhoum, Green biosynthesis and physicochemical characterization of Fe3O4 nanoparticles using Punica granatum L. fruit peel extract for optoelectronic applications, Text. Res. J. (2021) 00405175211006671. https://doi.org/10.1177/00405175211006671.

O. Louafi, A. Khelef, S. Zeroual, S. E. Laouini, and **M. L. Tedjani**, "Effect of Nickel Nitrate Concentration on the Size of Nickel Oxide Nanoparticles Bio-synthesized by Artemisia herba-alba Aqueous Leaves Extract and Improving Their Antioxidant Activities," J. Inorg. Organomet. Polym. Mater., 2021, doi: 10.1007/s10904-021-02152-5.

S.E. Laouini, A. Bouafia, A. V Soldatov, H. Algarni, **M.L. Tedjani**, G.A.M. Ali, A. Barhoum, Green Synthesized of Ag/Ag2O Nanoparticles Using Aqueous Leaves Extracts of Phoenix dactylifera L. and Their Azo Dye Photodegradation, Membr. . 11 (2021). https://doi.org/10.3390/membranes11070468.

Y. Belaiche, A. Khelef, S.E. Laouini, A. Bouafia, **M.L. Tedjani**, A. Barhoum, green synthesis and characterization of silver/silver oxide nanoparticles using aqueous leaves extract of artemisia herba-alba as reducing and capping agents, Rev. Rom. Mater. 51 (2021) 342–352.

International Seminars

Tedjani Mohammed Laid, Khelef Abdelhamid, 'Optimizing the Green Synthesis of Iron Oxide Nanoparticles Using Moringa Extract via RSM'international seminar on green chemistry and sustainable engineering (ISGCSE) 17-18 Déc. 2019, El-Oued, Algérie